



ISSN 1028-8546

Volume XXV , Number 1

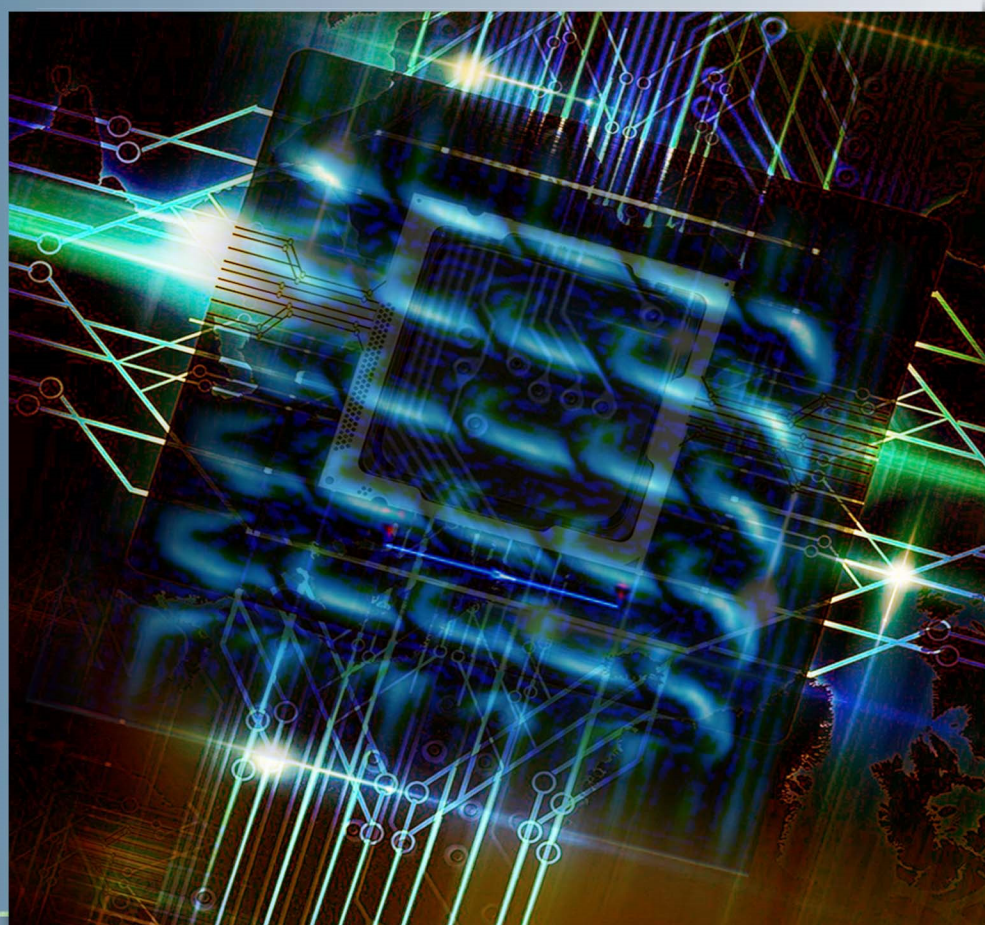
Section: En

March, 2019

Azerbaijan Journal of Physics

Fizika

www.physics.gov.az



G.M. Abdullayev Institute of Physics
Azerbaijan National Academy of Sciences
Department of Physical, Mathematical and Technical Sciences

Azerbaijan Journal of Physics

FIZIKA

*G.M. Abdullayev Institute of Physics
Azerbaijan National Academy of Sciences
Department of Physical, Mathematical and Technical Sciences*

HONORARY EDITORS

Arif PASHAYEV

EDITORS-IN-CHIEF

Nazim MAMEDOV

Chingiz QAJAR

SENIOR EDITOR

Talat MEHDIYEV

INTERNATIONAL REVIEW BOARD

Ivan Scherbakov, Russia
Kerim Allahverdiyev, Azerbaijan
Mehmet Öndr Yetiş, Turkey
Gennadii Jablonskii, Buelorussia
Rafael Imamov, Russia
Vladimir Man'ko, Russia
Eldar Salayev, Azerbaijan
Dieter Hochheimer, USA
Victor L'vov, Israel

Vyacheslav Tuzlukov, South Korea
Majid Ebrahim-Zadeh, Spain
Anatoly Boreysho, Russia
Mikhail Khalin, Russia
Hasan Bidadi, Tebriz, Iran
Natiq Atakishiyev, Mexico
Tayar Djafarov, Azerbaijan
Arif Hashimov, Azerbaijan
Javad Abidinov, Azerbaijan

Bagadur Tagiyev, Azerbaijan
Salima Mehdiyeva, Azerbaijan
Talat Mehdiyev, Azerbaijan
Ayaz Baramov, Azerbaijan
Tofiq Mammadov, Azerbaijan
Shakir Nagiyev, Azerbaijan
Rauf Guseynov, Azerbaijan
Almuk Abbasov, Azerbaijan
Yusif Asadov, Azerbaijan

TECHNICAL EDITORIAL BOARD

Senior secretary Elmira Akhundova, Nazli Guseynova, Sakina Aliyeva, Gulnura Jafarova
Nigar Akhundova, Elshana Aleskerova, Rena Nayimbayeva

PUBLISHING OFFICE

131 H. Javid ave, AZ-1143, Baku
ANAS, G.M. Abdullayev Institute of Physics

Tel.: (99412) 539-51-63, 539-32-23
Fax: (99412) 537-22-92
E-mail: jophphysics@gmail.com
Internet: www.physics.gov.az
<https://jophphysics.wixsite.com/ajpphysics>

Published at "SƏRQ-QƏRB"
17 Ashug Alessger str., Baku
Typographer : Aziz Gulaliyev

Sent for printing on: __.__. 201__
Printing approved on: __.__. 201__
Physical binding: _____
Number of copies: _____ 200
Order: _____

It is authorized for printing:

OPTICAL PARAMETER SPECTRA OF Bi_2Te_3 (Ni, Cu, Zn) SINGLE CRYSTALS

N. Z. JALILOV

G.M. Abdullayev Institute of Physics of Azerbaijan NAS

131, H. Javid ave., Baku, AZ 1143

xmamedova1986@gmail.com

$R(E)$ reflection spectra of Bi_2Te_3 (Ni, Cu, Zn) single crystals in beam energy interval $1 \div 6$ eV are investigated. For the case of Bi_2Te_3 single crystals the measurements are carried out parallel and perpendicular to optical C axis. It is shown that the energy values of some optical transitions from crystalline to non-crystalline state in Bi_2Te_3 (Ni, Cu, Zn) are constant.

Keywords: optical spectra, reflection coefficient, optical conduction.

PACS: 535.3; 539.2/6; 539.J.04

1. INTRODUCTION

$R(E)$ reflection coefficients of some materials (amorphous and single-crystalline) Se, Se-S, InSnTe_2 , $\text{TlIn}_{0.9}\text{Ce}_{0.1}\text{Se}_2$, $\text{TlInSe}_2\text{Ce}_{0.04}$, TlInSe_2 , Cu_3GdTe_3 , Cu_5GdTe_4 , CuGdTe_2 , $\text{Se}_{95}\text{As}_5$ (with impurity Sm), Bi_2Te_3 (Ni, Cu, Zn), Bi_2Te_3 , Bi_2Se_3 are measured and their optical parameters such as θ reflected light phase, indexes of κ absorption and n reflection, real ε_1 and imaginary ε_2 parts of dielectric constant, α absorption coefficient, function of characteristic volume $-\text{Im}g \varepsilon^{-1}$ and surface $-\text{Im}g(\varepsilon+1)^{-1}$ electron losses, electrooptical differential functions (α , β), optical conduction $\varepsilon_2 E$, integral function of bound state density $\varepsilon_0(E)$, effective number of valence electrons $n_{\text{ef}}(E)$ [1], taking part in transitions up to the given energy E are calculated by us.

The bismuth telluride is known as effective material for thermoelectric transformers. This material is easier to prepare in the form of enough perfect single crystals and obtain both n - and p -type by the way of doping [2,6].

Bi_2Te_3 (Ni, Cu, Zn) crystals has packet structure and the bound between neighbor packets has the mixed Van-der-Waals-covalent character [7]. The additional bond between packets is carried out because of transition of one p -electron on d -levels and overlapping of some d -levels with valence band. All this causes the significant metallic properties and comparably small energy values of forbidden bands in interval $0,15 \div 0,35$ eV.

Bi_2Te_3 (Ni, Cu, Zn) and its analogues are the uniaxial crystals in optical relation. The dielectric constant in them is the tensor of second order and depends on direction of incident wave with respect to optical C axis. The bismuth telluride optical properties are investigated in region of higher frequencies in work [5].

The band structure of Bi_2Te_3 (Ni, Cu, Zn) crystal is theoretically calculated in work [5]. The absence of data on (Δ) spin-orbital interaction value and complexity of chemical bond character between Bi_2Te_3 (Ni, Cu, Zn) atoms make the essential difficulty.

The bismuth telluride and solid solutions on its base are used at preparation of different energy

transformers [7]. The single-crystalline or polycrystalline Bi_2Te_3 and its solid solutions with Bi_2Se_3 are mainly used. The single-crystalline samples Bi_2Te_3 (Ni, Cu, Zn) are easily sheared by cleavage plane [0001] forming the mirror surface which stable to the oxidation that is very important for carrying out of optical measurements and doesn't require the special thermal treatment.

The study of band structure Bi_2Te_3 (Ni, Cu, Zn) hasn't achieved the level study of germanium and $A^{III}B^V$ compound that is connected with complexity of its crystalline and band structures [3]. This makes new investigations very important.

The measurement of crystal reflection coefficient of Bi_2Te_3 (Ni, Cu, Zn) of n - and p - types and also its polycrystalline film samples, parallel and perpendicular to C axis and the definition of spectra of their optical parameters on the base of the reflection coefficient are the tasks of the given work.

2. EXPERIMENT TECHNIQUE

The cleavage of Bi_2Te_3 (Ni, Cu, Zn) single crystal having the mirror smooth surface is used for measurement of $R(E)$ reflection coefficient. The reflection coefficient is measured by method of double-beam spectroscopy. The crystals are doped by Cl impurities having n - type conduction and Tb impurities which have p - type conduction.

The technology of single crystal Bi_2Te_3 (Ni, Cu, Zn) and films obtaining is described in works [8, 9, 10]. The single crystals are obtained by Bridgman method as in [3] and films by thickness $0,3 \mu\text{m}$ of polycrystalline Bi_2Te_3 (Ni, Cu, Zn) on cleavage surface of rock salt are obtained by its in sublimation vacuum.

The definition methods of optical parameters are given in work [11] and this procedure is described in [12].

As usual, the special computer programs are applied for calculation of optical parameters. The optical parameters of investigated materials are calculated by programs written by author of work [13]. These programs are checked at calculation of optical parameters of some materials in works [14 – 18].

3. RESULTS AND THEIR DISCUSSION

$R(E)$ reflection coefficients of single-crystalline Bi_2Te_3 (Ni, Cu, Zn) of n - and p - types parallel and perpendicular to C axis and also its film samples of n - and p - types are measured in the work; the spectra of their optical parameters: α absorption coefficient, ε_1 real and ε_2 imaginary parts of dielectric constant, indexes of κ absorption and n refraction, $n_{\text{eff}}(E)$ effective number of valence electrons taking part in transitions up to the given energy E , $\varepsilon_{0,\text{eff}}(E)$ effective static dielectric constant, functions of character $-\text{Im}g \varepsilon^{-1}$ volume and $-\text{Im}g(\varepsilon+1)^{-1}$ surface electron losses, phase of θ reflected light, $\varepsilon_2 E$ optical conduction, integral function of $\varepsilon_2 E^2$ bound state density and (α, β) electrooptical differential functions are defined.

Only spectra of $R(E)$ reflection coefficients, ε_1 real and ε_2 imaginary parts of dielectric constant, functions of character $-\text{Im}g \varepsilon^{-1}$ volume and $-\text{Im}g(\varepsilon+1)^{-1}$ surface electron losses, (α, β) electrooptical differential functions, spectra of σ optical conduction of massive and film samples are presented in fig. 1-12 for brevity and the values of interband optical transitions defined by maximums of σ optical conduction are presented in table 1.

The presented data give the possibility to compare optical spectra, transitions of single crystals and film samples Bi_2Te_3 (Ni, Cu, Zn).

The authors of work [5] for the case of high energies for single-crystalline Bi_2Te_3 (Ni, Cu, Zn) have found the transitions 1,4 eV and 1,1 eV. As it is seen from table 1 the same transitions are observed for n - and p - types correspondingly. As it is seen from table 1 the transitions corresponding to corresponding energies 1,4 eV and 1,15 eV for film samples Bi_2Te_3 (Ni, Cu, Zn) of n - and p -types. From this it is concluded that the values of some optical transitions Bi_2Te_3 (Ni, Cu, Zn) at transition of material from crystalline to non-crystalline state for non-crystalline samples are saved.

As it is mentioned in [18] the study of absorbing transitions in materials is impossible because of absorption big value in region of interband transition energies $E > E_g$ (E_g is forbidden band thickness). The reflection is the unique method.

The analytical singularities of imaginary part of $\varepsilon_2(E)$ complex dielectric constant and functions bound by dN/dE state densities are always coincide and the gradient of interband states makes the main contribution into dN/dE functions:

$$\frac{dN_{ij}}{dE} \sim \int \frac{dS_k}{|\nabla_k E_{ij}|}, \quad (1)$$

where $E_{ij}(k) = E_j(k) - E_i(k)$ is between conduction band and valence band. dN/dE values near critical points in k -space defined by $|\nabla_k E_{ij}| = 0$ expression and also the position of critical points and transition type can be theoretically calculated from band structure

The analysis of $\varepsilon_2(E)$, dN/dE functions and $R(E)$ reflection coefficient show that disposition and

character of maximums in their spectra are similar ones or very close to each other. That's why the values of corresponding interband gaps and band nature can be defined with the help of direct comparison of experimental data in $E > E_g$ region with theoretical calculations of dN/dE function. As it is mentioned in [18] E_0 resonance frequency presents itself that frequency at which $2nk \cdot E$ conduction achieves to maximum by which the interband transitions are defined.

The high transparency in wide energy region $E < E_g$ is character for non-crystalline materials and several methods of E_g definition are known. Its evaluation by the level of $\alpha(E)$ absorption coefficient of long-wave edge is the one of them. E_g exact value for non-crystalline semiconductors is discussion one and as usual the discussion of $\alpha(E)$ spectrum character in Urbakh and Tauc models is carried out without E_g evaluations [20,21]. E_g is defined for $\alpha(E) = 10^3 \text{cm}^{-1}$ value by Tauc model.

As it is mentioned in [20] the state density $N(E)$ is the similar useful one for crystalline and non-crystalline substances. The state density motion in non-crystalline substance doesn't essentially differ from corresponding one in crystal. The thin structure in 1st case can be blurred and local states can appear in forbidden band. The band structure is saved as it is defined by atom short-range order in materials.

The author of work [22] mentions that it is impossible to make the principal boundary between single-crystalline, polycrystalline and amorphous substance states. The presence of the band structure i.e. the forbidden band and conduction band can be derived from the fact of atom short-range existence and it is no necessity to require the periodic atom disposition for such derivation.

As authors [23-25] show that the structure of indirect binary compound can be considered as collection of different basis clusters presented in structural matrix with different static weight and put into effective medium. As authors [26] mention the atom short-range order makes the main contribution in electronic state density. However, as atom short-range order in binary compounds can significantly change from node to node in structural matrix of amorphous substance, especially statistics of basis clusters defines the final electronic state density. Thus, the low-molecular structural configurations that are accompanied by significant benefit in energy can appear at melt cooling or in the process of amorphous substance formation by another way. Such formations can serve neither as crystal germs nor as the centers of solid amorphous phase growth because of the fact that they are characterized by special symmetry.

The ambiguity of structural order in compositional amorphous solid states by $A_x B_{1-x}$ type can be considered as their general property. The peculiarities of atom short-range order near each node are caused firstly by physical methods of $A_x B_{1-x}$ system preparation and secondly by chemical order principle, taking under consideration «rule 8-N» [20] and value of a quantity of bond energy of neighbor atoms.

The decomposition of ideal structure in non-crystalline solid state takes place in systems including the atoms with not-divided electron couples. It is very often that at the breakage of electron couple is on the one of fragments, i.e. the bond heterolytic breakage. The one positive and one negative charged defect centers in regions of atom short-range order appear. The energy necessary for bond breakage is partly compensated because of existence of non-divided electron couple of atoms being surrounding and number of chemical bonds doesn't change. Thus, the structural disorder exists in homogeneous non-crystalline materials of stoichiometric composition along with density oscillations and existing topological disorder of different types. It is revealed in the form of positive and negative charged defect centers as in the case of point defects in crystals. As a result, the reaction defects, the formations of which are characterized by lowest change of free energy, dominate.

The idea of atom short-range order at formation of electron energy bands is the one of the fundamental conceptions in physics of disordered system. This idea has the experimental and theoretical confirmation on the example of many non-crystalline solid and liquid semiconductors [27]. The mechanism of formation of valence and conduction bands in non-crystalline semiconductors is mainly formed by authors [28, 29]. The similarity of the main peculiarities of spectral dependence of imaginary part dielectric conduction $\varepsilon_2(E)$ is emphasized in the works of these authors for non-crystalline semiconductors and their crystal analogues. This similarity is shown by author [28] on the example of selenium. The analogous conclusion is made in the relation to $\alpha\text{-As}_2\text{S}_3$ and $\alpha\text{-As}_2\text{Se}_3$ in works [28, 29].

Only maximum smoothing takes place in their $\varepsilon_2(E)$ for the cases of amorphous materials and similarity of the curves for amorphous and crystalline samples is preserved.

Nowadays, it is established that one can directly change optical, photoelectric and electric properties of non-crystalline semiconductors with the change of chemical composition and also by impurity introduction. The concentration changes of charged defect centers D^+ и D^- (U^{-1} are centers) takes place in them and these defects form from initial neutral defects D^0 by reaction:



which can be eigen or impurity and mixed defects giving the possibility to control by their physical properties.

Thus, reflection coefficients $R(E)$ of single crystals and film samples $\text{Bi}_2\text{Te}_3(\text{Ni, Cu, Zn})$ of n - and p -types in beam energy interval 1–6 eV falling normally to the surface are measured in the work. The measurements are carried out parallel and perpendicular to C axis for the case of Bi_2Te_3 single crystals. It is shown that values of some optical

transitions $\text{Bi}_2\text{Te}_3(\text{Ni, Cu, Zn})$ from crystalline to non-crystalline state are preserved for the non-crystalline samples.

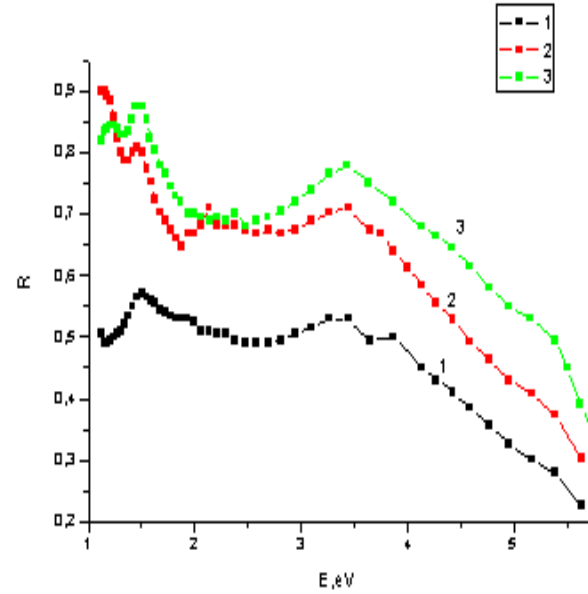


Fig. 1. Reflection spectra (R) of single crystals: 1 - Bi_2Te_3 (Cu), 2 - Bi_2Te_3 (Ni), 3 - Bi_2Te_3 (Zn).

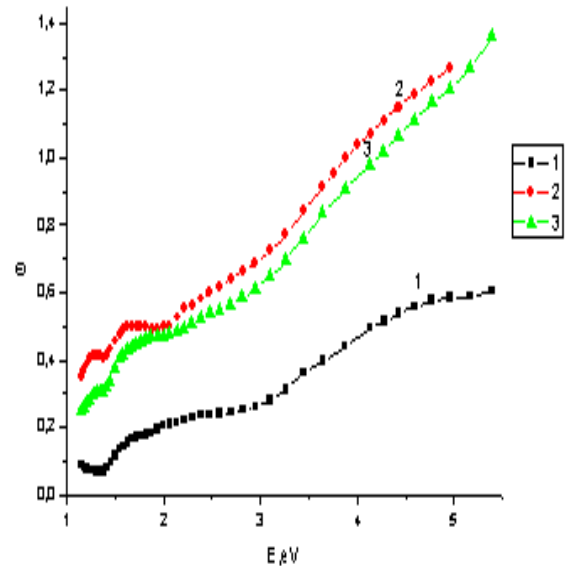


Fig. 2. Reflection phase spectra (θ) of single crystals: 1 - Bi_2Te_3 (Cu), 2 - Bi_2Te_3 (Ni), 3 - Bi_2Te_3 (Zn).

Only reflection coefficient spectra, ε_1 real and ε_2 imaginary parts of dielectric constant, functions of character $-\text{Im}g\varepsilon^{-1}$ volume and $-\text{Im}g(\varepsilon+1)^{-1}$ surface electron losses, the spectra of (α, β) electrooptical differential functions, the spectra of optical conduction of σ massive and film samples correspondingly are shown for brevity in fig. 1–12 and the values of interband optical transitions defined by σ optical conduction maximums are shown in table.

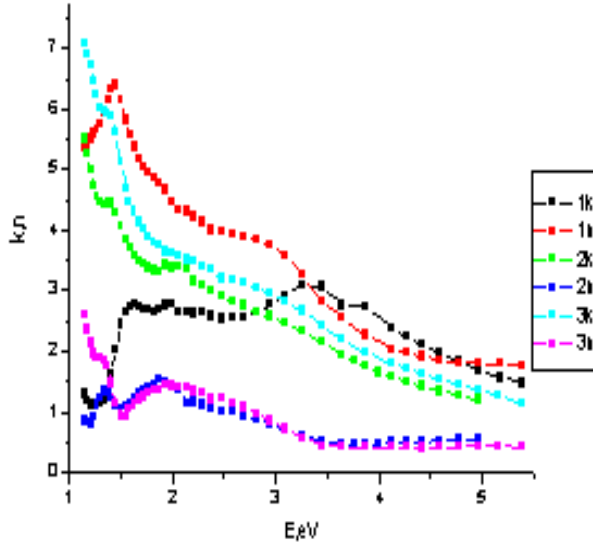


Fig. 3. k and n spectra of single crystals: 1 - $\text{Bi}_2\text{Te}_3(\text{Cu})$, 2 - $\text{Bi}_2\text{Te}_3(\text{Ni})$, 3 - $\text{Bi}_2\text{Te}_3(\text{Zn})$.

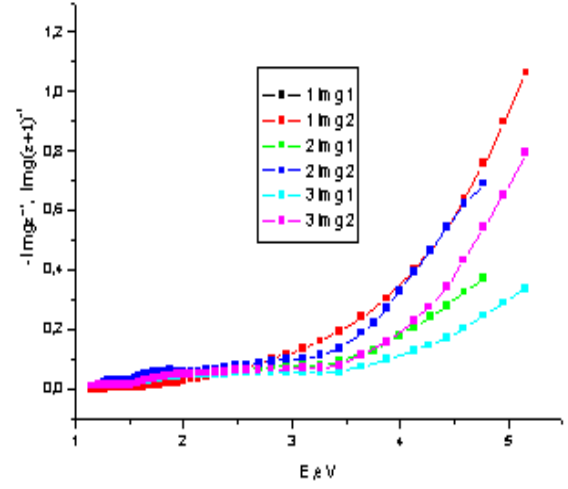


Fig. 6. $-\text{Img}\epsilon-1$ and $-\text{Img}(\epsilon+1)^{-1}$ spectra of single crystals: 1 - $\text{Bi}_2\text{Te}_3(\text{Cu})$, 2 - $\text{Bi}_2\text{Te}_3(\text{Ni})$, 3 - $\text{Bi}_2\text{Te}_3(\text{Zn})$.

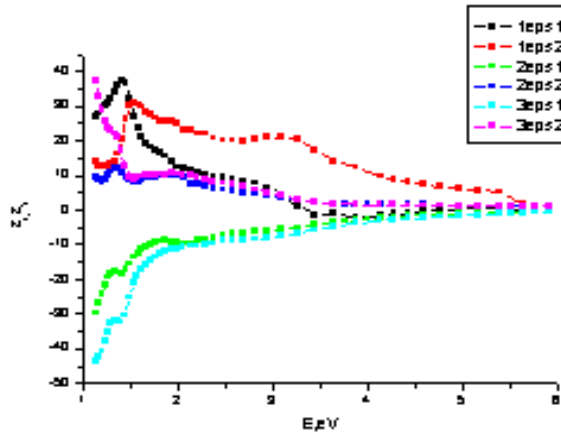


Fig. 4. ϵ_1 and ϵ_2 spectra of single crystals: 1 - $\text{Bi}_2\text{Te}_3(\text{Cu})$, 2 - $\text{Bi}_2\text{Te}_3(\text{Ni})$, 3 - $\text{Bi}_2\text{Te}_3(\text{Zn})$.

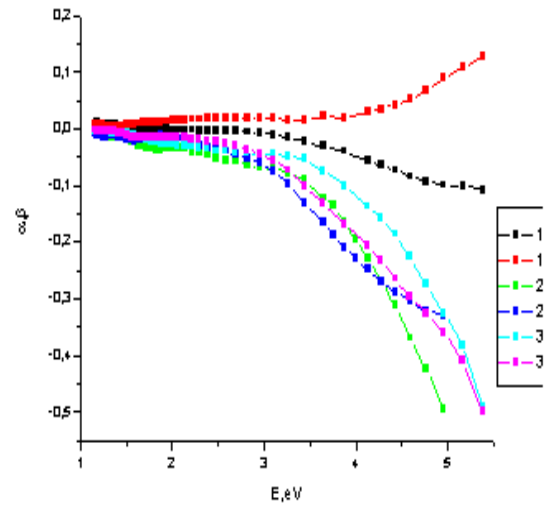


Fig. 7. α and β spectra of single crystals: 1 - $\text{Bi}_2\text{Te}_3(\text{Cu})$, 2 - $\text{Bi}_2\text{Te}_3(\text{Ni})$, 3 - $\text{Bi}_2\text{Te}_3(\text{Zn})$.

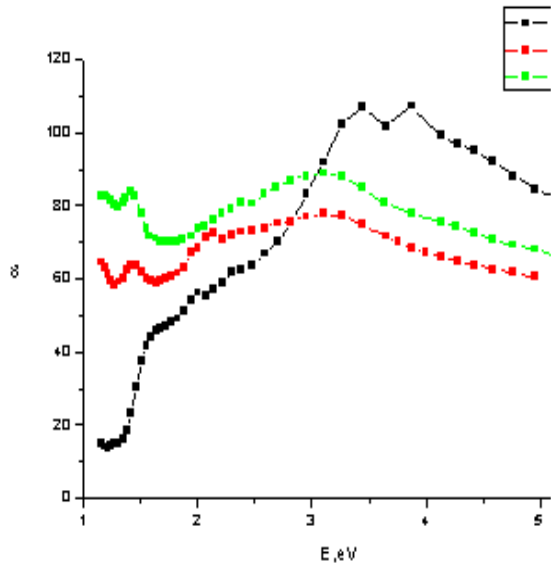


Fig. 5. α spectra of single crystals: 1 - $\text{Bi}_2\text{Te}_3(\text{Cu})$, 2 - $\text{Bi}_2\text{Te}_3(\text{Ni})$, 3 - $\text{Bi}_2\text{Te}_3(\text{Zn})$.

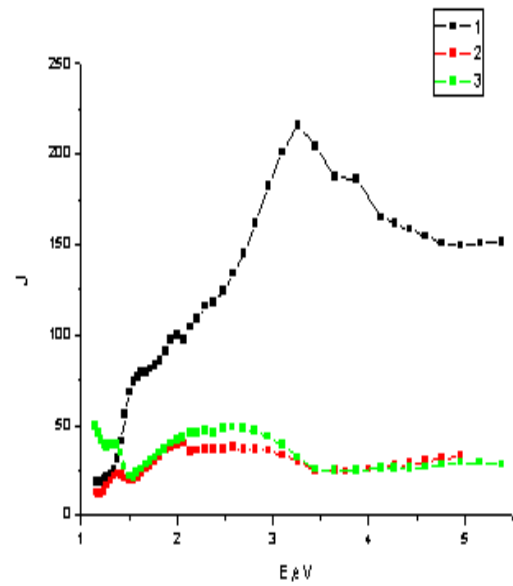


Fig. 8. The state density spectra (J) of single crystals: 1 - $\text{Bi}_2\text{Te}_3(\text{Cu})$, 2 - $\text{Bi}_2\text{Te}_3(\text{Ni})$, 3 - $\text{Bi}_2\text{Te}_3(\text{Zn})$.

OPTICAL PARAMETER SPECTRA OF Bi_2Te_3 (Ni, Cu, Zn) SINGLE CRYSTALS

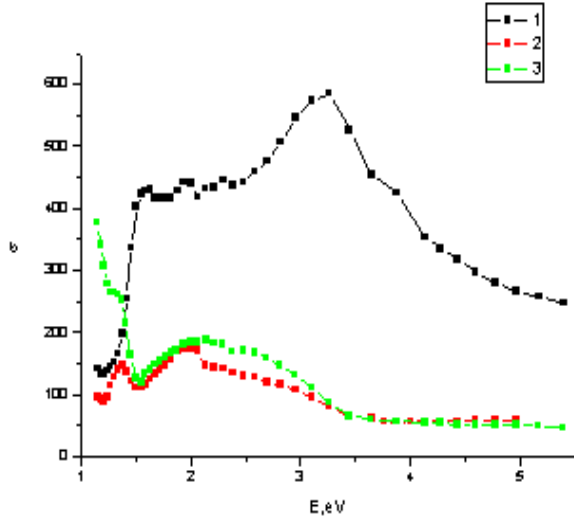


Fig. 9. Optical conduction (σ) of single crystals: 1 - Bi_2Te_3 (Cu), 2 - Bi_2Te_3 (Ni), 3 - Bi_2Te_3 (Zn).

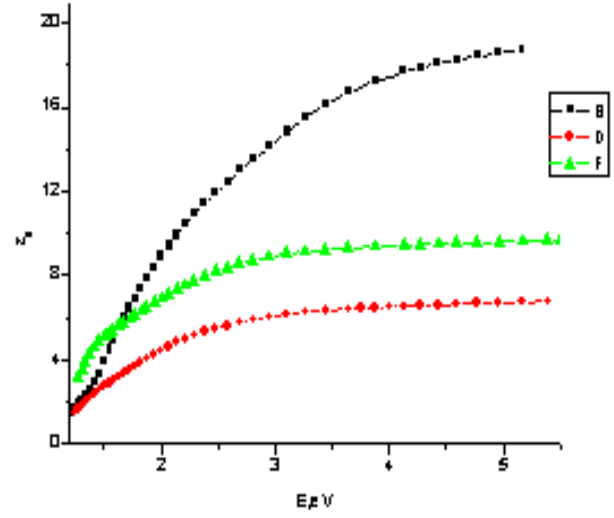


Fig. 11. ϵ_0 spectra of single crystals: 1 - Bi_2Te_3 (Cu), 2 - Bi_2Te_3 (Ni), 3 - Bi_2Te_3 (Zn).

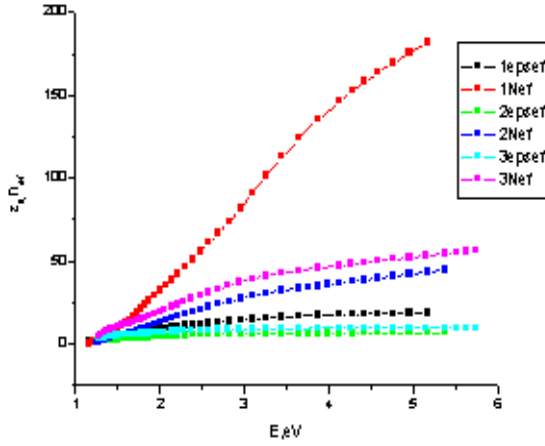


Fig. 10. ϵ_0 and n_{eff} spectra of single crystals: 1 - Bi_2Te_3 (Cu), 2 - Bi_2Te_3 (Ni), 3 - Bi_2Te_3 (Zn).

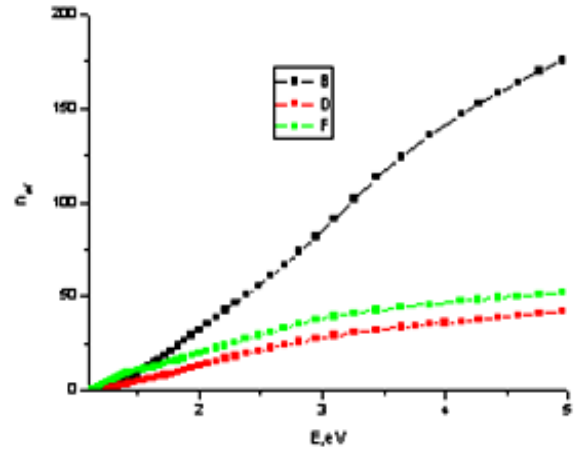


Fig. 12. n_{eff} spectra of single crystals: 1 - Bi_2Te_3 (Cu), 2 - Bi_2Te_3 (Ni), 3 - Bi_2Te_3 (Zn).

Table

The optical transitions in Bi_2Te_3 (Ni, Cu, Zn) single crystals in 1 ÷ 6 eV energy interval of n - and p - types parallel and perpendicular to C axis defined by optical conduction.

n - type parallel to C axis	n - type perpendicular to C axis	p - type parallel to C axis	p - type perpendicular to C axis
1.01	0.70	1.41	1.19
1.10	0.79	2.02	1.27
1.14	1.29	2.29	1.37
1.36	1.86	2.96	1.81
1.94	2.07	3.18	1.92
2.16	2.17	7.21	2.10
2.28	2.31	7.41	2.23
2.44	2.58	-	2.42
2.61	2.71	-	2.99
3.02	3.09	-	4.95
4.24	3.95	-	6.98
5.06	4.61	-	7.10
7.08	6.45	-	-
7.22	6.81	-	-
7.38	6.97	-	-
7.69	7.12	-	-
8.10	7.41	-	-
-	8.08	-	-
-	8.32	-	-

-
- [1] *N.Z. Jalilov*. Optical spectra of the selenium received under various conditions, Transactions, AMEA FRTE, physics and astronomy, 2011, № 2, p.141
 - [2] *B.M. Goltsman, V.A. Kudinov, I.A. Smirnov*. Semiconductor thermoelectric materials on the basis Bi_2Te_3 , "Nauka", Moscow 1972, p.216 (in Russian).
 - [3] *P.M.Lee, L.Pincherle*. Pros. Phys. Soc. 81, 461, 1963.
 - [4] *D.I. Greenaway and G. Harbeke*. I. Phys. Chem. Solids Pergamon Press, 26, 1585, 1965.
 - [5] *E.V. Oleshko, V.N. Korolishin*. FTT, 27, 2856, 1985.
 - [6] *V.L. Gurevich*. Kinetics of phonon systems M.: Nauka, 1980, 14 (in Russian).
 - [7] *E. Mooser, W.C. Pearson*, Phys. Chem. Solids 7, 5, 1958.
 - [8] *B.M. Goltsman, Z.M. Dashevskiy, V.I. Kaydanov, N.V. Kolomoets*. Film thermoelements: physics and applications (M.: Nauka, 1985), p. 23 (in Russian).
 - [9] *S.A. Semiletov*. Reports of Crystallography Institute, 10, 74, 1954 (in Russian).
 - [10] *V.V. Sobolev, V.V. Nemoshkalenko*. Electronic structure of solids (Kiyev, Naukova. Dumka) 1988 (in Russian).
 - [11] *R. Willardson* Optical properties of semiconductors. M., 1970.
 - [12] *N.Z. Jalilov*. Reports of X International. conf. Opto–nanoelectronics, nanotechnology and microsystems», Ulyanovsk, 2008, 45 (in Russian).
 - [13] *N.Z. Jalilov, G.M. Damirov*. Reports of X International. conf. Opto–nanoelectronics, nanotechnology and microsystems», Ulyanovsk, 2008, 45 (in Russian).
 - [14] *N.Z. Jalilov, G.M. Damirov*. FTP, 45, 500, 2011 (in Russian).
 - [15] *N.Z. Jalilov, G.M. Damirov*. Transactions, AMEA FRTE, physics and astronomy, XXVIII, №5, 134, 2008; XXIX, 125, 2009.
 - [16] *N.Z. Jalilov, M.A. Maxmudova*. Transactions, AMEA FRTE, physics and astronomy, XXX, 71, 2010.
 - [17] *N.Z. Jalilov, S.I. Mextieva, N.M. Abdullayev*. Transactions, AMEA FRTE, physics and astronomy. XXVII, 114, 2007.
 - [18] *J.C. Phillips*. Phys. Rev. 125, 1931, 1962, 133, A452, 1964.
 - [19] *T. Moss, G. Barrel, B. Ellis*. Semiconductor opto-electronics M., Mir, 1976.
 - [20] *H. Mott, E. Deviss*. Electronic Processes in Non-Crystalline Materials M., Mir, 1982.
 - [21] The Ioffe Institute, Electronic phenomena of glass-like semiconductors, Nauka 486, 1996 (in Russian).
 - [22] *A. Rose*. Concept in Photoconductivity M., Mir, 1966 (in Russian).
 - [23] *Y.N. Shunin, K.K. Shvarts*. JSX, 27, № 6, 146 - 150, 1986 (in Russian).
 - [24] *K.K. Shvarts, Y.N. Shunin, Y.A. Temeris*. Izv. AN LatSSR, ser. Phys.-techn, № 4, 51 - 57, 1987 (in Russian).
 - [25] *K.K. Shvarts, F.V. Pirgorov, Y.N. Shunin, J.A. Teteris*. Cryst. Latt. Def. Amorph. Mat., 17, 133- 138, 1987.
 - [26] *Y.N. Shunin, K.K. Shvarts*. FTP, 23, №6, 1049-1053, 1989 (in Russian).
 - [27] *A.I. Gubanov*. Quant-electronic theory of amorf. semiconductors. M., L., Academy Science, USSR, 1966, 250 c (in Russian).
 - [28] *M. Kastner*. Phys. Rev. Lett., 1972, 26 N7, p.355.
 - [29] *R.E. Drews, R.L. Emerald, M.L. Slade, R. Zallen*. Solid State Comm., 1972, 10, N3, p. 2.
 - [30] *F.K. Aleskerov, N.Z. Jalilov, Sh. Kahramanov*. Transactions, AMEA FRTE, physics and astronomy, XXVII № 2, 2008.

Received: 06.12.2018

ION-OPTICAL CALCULATION OF TIME-OF-FLIGHT MASS-SPECTROMETER

T.K. NURUBEYLI, K.Z. NURIYEV

*G.M. Abdullayev Institute of Physics of Azerbaijan NAS**131, H.Javid ave., Baku, AZ 1143**kamilnuri@rambler.ru*

The parameters of shock mass-spectrometer for the dust particle composition analysis in near-Earth space are calculated. The time-of-flight mass-spectrometer of reflectron type is used as mass-spectrometer. The analytical expressions for particle trajectories in phase space in device different parts are obtained in paraxial beam approximation. The transmission value of device ion-optical system is calculated on the base of obtained expressions with the help of static modelling method. The device resolution is calculated and its dependence on mass-spectrometer parameters is defined.

Keywords: time-of-flight mass-spectrometer, cosmic dust, resolution.

PACS: 07.75.+h

1. INTRODUCTION

The determination of cosmic dust chemical composition in near-Earth space by the analysis of shock plasma ion composition appearing at collision of the particle with solid (atom-pure) target [1] is the one of the methods of solid substance investigation.

The ion-optical parameters of mass-spectrometer used as the electrostatic time-of-flight mass-spectrometer (TFMS) are calculated in the given work. The choice of the given mass-spectrometer type is caused by the fact that it has some advantages in comparison with other schemes of mass-analyzers: the construction simplicity, wide range of investigated masses, high sensitivity, and high accuracy of quantitative analysis.

The electrostatic mirror which allows us to compensate the energy spread in ion beam is included into time-of-flight mass-spectrometer scheme for its resolution increase. Such device scheme is called mass-reflectron [2]. The electrostatic lenses which allow us to increase the device transmission though the device resolution decreases are included in the device scheme investigated by us [3]. But in some cases, the high transmission is the dominating condition of device scheme choice.

The variants of ion-optical schemes of the calculated device have the series of features of construction: grid count in ion source, target sizes on which the ionization of

the investigated material takes place, the drift tube diameters and etc. Device consists of three main elements (fig.):

1. The ion source in which the primary formation of ions, their division in packets of different masses and introduction in analyzer take place. The source consists of target on which the investigated material ionization takes place and set of grids which are field-forming electrodes parallel to the target. In calculations the field between the grids is described as the field of plane capacitor.

2. The time-of-flight camera with electrostatic lens system in which the further division of ion packets and transformation of ion packet phase volume with the aim of device transmission increase. The electrostatic lenses are formed by tubular elements of time-of-flight camera between which the potential difference is formed. The lenses are thin ones for the given interval of potential variation on exciting electrode, i.e. their main plane coincides with the lens plane of symmetry.

3. The electrostatic plane mirror (reflectron) formed by plane electrode system. The electrodes are made in the form of the grids in the joint of reflectron with time-of-flight cameras. The series of auxiliary electrodes with linear potential distribution on them is put for the formation of more homogeneous potential distribution in reflectron zone between main electrodes.

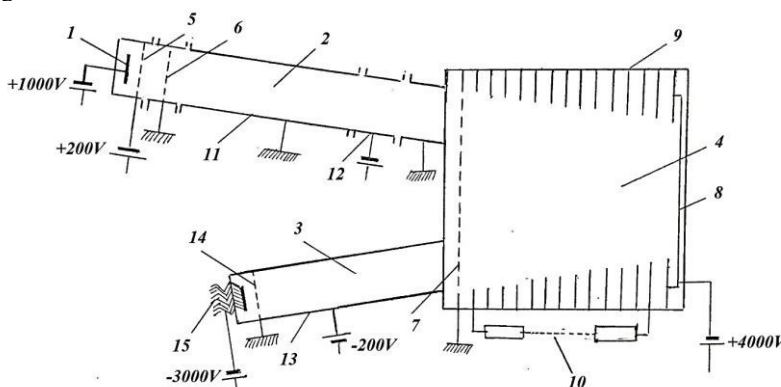


Fig. Mass-reflectron scheme 1 - is target; 2, 3 - are drift tubes, 4 - is reflectron, 5 - is accelerating grid, 6 - is monitor grid, 7 - is reflectron input grid, 8 - is reflectron plane, 9 - is correction electrodes, 10 is voltage divider, 11-13 are focusing electrodes

The accelerating gap for the energy increase of ions entering in detector is formed in the one of variants of calculated device scheme before ion detector, i.e., for increase of its sensitivity.

The values of the device resolution and transmission are the important parameters of mass-spectrometers. As the device dimensions have the final sizes then the part of the ions forming in the source are in its walls and are lost for the analysis. The quantity of such ions can consist of the significant part of forming ions. That's why the increase of device transmission values becomes the especially actual at few quantities of investigated material.

2. THE CALCULATION OF ELECTRO-FOCUSING SYSTEM TRANSMISSION VALUE.

The device transmission P value is defined as the ratio of ion number being in N_1 detector to ion number formed on N_0 target:

$$P = \frac{N_1}{N_0} \quad (1)$$

This ratio is calculated by static modelling method. It is supposed that the ion number in phase space element in ionization region has the form:

$$dN = \text{const} \cdot \exp[-V_{z0}^2 + V_z^2 + V_{\theta0}^2] \cdot r_0 dr_0 dV_{z0} dV_{z0} dV_{\theta0} \quad (2)$$

where $V_z, V_{z0}, V_{\theta0}$ are the components of velocity vector in cylindrical coordinate system in the velocity space r_0 is the distance from the time-of-flight camera to the target, T is ion temperature.

Let's introduce the dimensionless values defined by the ratios for the convenience.

$$\rho = \frac{r}{R_d}; v = \frac{V}{\sqrt{2\eta|W|}}; r = t \frac{\sqrt{2\eta|W|}}{R_d};$$

$$\varepsilon_0 = \frac{E_0}{e|W|}; W = -U_0; U_0 > 0$$

where R_d is the time-of-flight camera radius, v is ion velocities in drift field and ε_0 is the energy dimensionless value of the ions on the target; W is the potential difference between the source last grid and the target, U_0 is the target potential; E_0 is average ion energy on the target ($E_0 = 3/2kT$); $\eta = e/m$, e , m are the charge and mass of ion.

$$dN_0 = \text{const} \exp \left[-\frac{v_{r0}^2 + v_z^2 + v_{\theta0}^2}{\frac{2}{3}\varepsilon_0} \right] \rho_0 d\rho_0 dV_{z0} dV_{r0} dV_{\theta0} \quad (3)$$

moreover $v_{z0} \geq 0$, $\rho \leq \rho_m = R_0/R_d$, R_0 is the target radius.

The transformation of phase coordinates in ion source, drift gap in lens are defined by the following expressions:

a) in homogeneous field of ion source, the phase coordinates uniquely determine the state of a second-order system in terms of "k"

$$\rho_k^2 = (v_{r,k-1} \cdot \tau_k + \rho_{k-1})^2 + v_{\theta,k-1} \tau_k^2,$$

$$v_{rk} = \frac{(v_{r,k-1}^2 + v_{\theta,k-1}^2) \tau_k + \rho_{k-1} v_{r,k-1}}{\rho_k}, \quad (4)$$

$$v_{\theta,k} = \frac{\rho_{k-1}}{\rho_k} v_{\theta,k-1}; \quad v_{z,k} = \sqrt{v_{z,k-1}^2 + w_k}$$

$$\text{where } \tau_k = 2 \frac{d_k}{w_k} \left[\sqrt{v_{z,k-1}^2 + w_k} - v_{z,k-1} \right]$$

$$w_k = \frac{U_k - U_{k-1}}{W}; \quad d_k = \frac{Z_k - Z_{k-1}}{R_d} \quad (5)$$

Z_k, U_k are coordinate and potential of k -th grid.

Z_0, U_0 are coordinate and potential of target.

b) in lens with power $P_j = -1/f_j$ (f_j is focal distance)

As the optical power of the lens for each ion is the same so we have

$$\rho_j = \rho_{j-1}$$

$$v_{r,j} = v_{r,j-1} + P_j \rho_{j-1} v_{z,j-1};$$

$$v_{\theta,j} = v_{\theta,j-1}; \quad v_{z,j} = v_{z,j-1} \quad (6)$$

The transformation of phase coordinates in reflector at transmission calculation is accepted as the equivalent to the one in drift gap by the length:

$$S_p = 4d_r \cdot \frac{U_0}{U_r}$$

where U_r the voltage on reflector is, d_r is reflector depth.

Thus, the transformation of phase coordinates in the considered device can be presented as consistent transformation of (2)–(4) type. This consistence is defined by device scheme.

The distribution type function (1) is modeled with the help of standard gauge of random numbers. After each transformation (2), (3) the condition of ion transmission through device element is checked and ions with $\rho \geq 1$ is excluded from the further consideration.

3. THE CALCULATION OF THE DEVICE RESOLUTION

The ratio of average run time τ_0 from the target up to the double value of time spread of fixed mass ion receipt on detector:

$$R = \frac{\tau_0}{2\Delta\tau} = \frac{m}{\Delta m}$$

The static modelling method allows us to calculate the device resolution but makes difficult the definition of the dependence of its value on device parameters. That's why in the given work R is obtained on the base of obtained analytical expressions.

The time of motion of the ion emitted with \mathcal{E}_0 initial energy under angle φ_0 to normal of output diaphragm in the source with one grid is equal:

$$\tau_U = 2d_1(\sqrt{1 + \mathcal{E}_0 \cos^2 \varphi_0} - \sqrt{\mathcal{E}_0 \cos \varphi_0}) \quad (7)$$

with two grids is equal:

$$\tau_U = 2\frac{d_2}{w_2}(\sqrt{1 + \mathcal{E}_0 \cos^2 \varphi_0} - 2\frac{d_1}{w_1}\sqrt{\mathcal{E}_0 \cos \varphi_0}) + 2(\frac{d_1}{w_1} - \frac{d_2}{w_2})\sqrt{w_1 + \mathcal{E}_0 \cos^2 \varphi_0} \quad (8)$$

The ion motion time in drift field gap by S_i length without lenses is [4]:

$$\tau_i = S_i - \frac{\mathcal{E}_0}{2} S_i \quad (9)$$

The motion time in the reflector is:

$$\tau_r = \frac{4U_0}{E \cdot R_d} \sqrt{1 + \mathcal{E}_0} (\sin \varphi_1 \cdot \sin \beta \cdot \cos \alpha + \cos \varphi_1 \cdot \cos \beta) \quad (10)$$

where E is absolute value of electric field strength in reflector; φ_1 is the angle between ion velocity vector and Z tube axis at the output in reflector; α is the angle at the output in reflector between ion velocity vector component perpendicular to Z axis and X axis being in the device meridional plane; β is the angle between Z and reflector axes.

The motion time in detector accelerating gap:

$$\tau_D = \frac{2d_D}{w_D} (\sqrt{1 + \mathcal{E}_0 + w_D} - \sqrt{1 + \mathcal{E}_0}) \quad (11)$$

where $w_D = \frac{U_D}{W}$

Expanding the expressions (7), (8), (10), (11) into series over \mathcal{E}_0 and taking under consideration only 1st expansion order we obtain the following formula for each device element:

$$\tau = \tau_0 + \mathcal{E}_0 \cdot \tau_{\mathcal{E}} + \Delta\tau \quad (12)$$

where $\mathcal{E}_0 \cdot \tau_{\mathcal{E}}$ and $\Delta\tau$ are ion packet broadening by coordinate because of the spreads by energy and by angles correspondingly.

Then, we obtain the following expressions for (12) formula components for single-grid source for device different parts:

$$\tau_{0U} = 2d_r, \tau_{\mathcal{E}U} = d_1$$

and

$$\Delta\tau_U = 2d_1\sqrt{\mathcal{E}_0}(1 - \cos \varphi_{0m})$$

where φ_{0m} is maximal angle between velocity vector ions and tube axis on target (for ions reached the detector) for the drift gap S_i , $\tau_{0i} = S_i$.

The reflector allows us to compensate the energy spread in ion packet. The focusing condition of first order by the energy in detector plane is defined from the condition:

$$\frac{\delta\tau}{\delta\mathcal{E}_0} = \tau_{\mathcal{E}} = \tau_{\mathcal{E},U} + \sum_i \tau_{\mathcal{E},i} + \sum_j \tau_{\mathcal{E},j} + \tau_{\mathcal{E},R} + \tau_{\mathcal{E},D} = 0 \quad (13)$$

then the device resolution is equal:

$$R = \frac{\tau_{0U} + \sum_i \tau_{0i} + \sum_j \tau_{0j} + \tau_{0R} + \tau_{0D}}{2(\Delta\tau_U + \Delta\tau_R)} \quad (14)$$

If we neglect the time-of-flight times in the source and detector, then from (14), (15) we obtain the following approximate formula:

$$R = \frac{1}{2\varphi_{1m}} \cdot \frac{\cos \beta}{\sin \beta} \quad (15)$$

Formula (15) gives the practically similar results (maximal difference 2,5 %) for the considered device parameters.

The calculation results for ion shock plasma having the energy of directed motion 1keV and heat motion 5eV are presented in table.

Table
The calculation results for ion shock plasma parameters having the energy of directed motion 1keV

Parameter	With lenses	Without lenses
P	9,1%	5,4%
R	2,61%	3,63%
U_R	1,17%	1,7%
$\Delta\tau_0$	66,82%	66,82%
$\Delta\tau$	0,128%	0,092%
φ_{0m}	0,32%	0,23%
φ_{1m}	0,22%	0,016%

The ion time of flight value can be found by the following formula:

$$t = R_d \sqrt{\frac{M}{Z \cdot U_0}} \tau \cdot 0,723 \cdot 10^{-6} \quad (16)$$

Here R_d is expressed in centimeters, M is expressed in proton masses, Z is expressed in electron charges, U_0 is expressed in volts. For example, from (16) it is followed that $Z = 1$ average time-of-flight t_0 is 40,1 μ s and time spread of ion receipt on detector is 77 ns at $M=109$.

4. CONCLUSION

Thus, the previous experiments show that characteristics of developed mass-reflectron correspond to problem methodical aspects and also to structural and technological device developmental work. The mass-reflectron parameters are given below:

Velocity range km/sec	3-35
Mass range, gr	10^{-14} - 10^{-12}
Range of registered mass numbers, amu	12 – 75
Resolution (for Fe^{56}) at level 10%	not less 200
Sensitivity by Fe^{56} K1/kg	not less 200

-
- | | |
|---|---|
| <p>[1] <i>G.Braun, E.Go Run, J.Kissel, N. Failid.</i> Solid particles in the solar system. International astronomical union symposium № 90 edited by <i>İ. Halliday, B.A. McIntosh</i>, 1979, p. 275.</p> <p>[2] <i>V.I. Karatayev, B.A. Mamirin, D.V. Shmikk.</i> JTF, 1971, t. 41, v.7, p. 1498-1501.</p> <p>[3] <i>Z.K. Nurubeyli, T.K. Nurubeyli, K.Z. Nuriyev.</i> Mass-spectrometer for determining the</p> | <p>chemical composition of micrometeorites in near-Earth space, Scientific works NAA, 2006, cild 8, №.1, s. 56-61 (in Russian).</p> <p>[4] <i>V.N. Kelman, S.Y. Yavor.</i> Electronic optics, Leningrad, Publishing home “Science”, 1968, p. 167 (In Russian)</p> |
|---|---|

Received: 26.12.2018

THE USE OF NUCLEAR-PHYSICAL METHODS FOR THE ANALYSIS OF WASTES FROM MINING AND PROCESSING INDUSTRY

I.Z. KAMANINA¹, S.P. KAPLINA^{1,2}, M.V. GUSTOVA²,
M. V. FRONTASYEVA², N.E. PUKHAEVA²

¹State University "Dubna", Dubna, Russian Federation
(141980, Moscow region, Dubna, Universitetskaya str. 19),
e-mail: kamanina@uni-dubna.ru, dzerkachigoeva@yandex.ru, sv_kap@mail.ru

²Joint Institute for Nuclear Research, Dubna, Russian Federation
(141980, Moscow region, Dubna, Joliot-Curie str. 6),
nelli.pukhaeva@gmail.com, gust@jinr.ru, marina@nf.jinr.ru

The topic of using nuclear-physical methods for the analysis of waste mining and processing industry is shown by the example of the analysis of the dry part (beach zone) of the Unal tailings Mizur concentrator, located in the Central part of the Alagir district, the Republic of North Ossetia-Alania, in the valley of the river Ardon. Analytical identifications were performed at the Joint Institute for Nuclear Research (JINR) in Dubna, Moscow region. X-ray fluorescence (XRF) and instrumental neutron activation analysis (INAA) were used to identify the composition of multi-element samples, which allows us to obtain data on the content of 39 elements in the composition of the tails. The content of Ca, Ti, Cr, Mn, Cu, Sb in tails was determined by two methods. The results obtained by XRF and INAA are the same within the measurement uncertainties. The Unal tailing dump is a geochemical anomaly with the content of Zn, As, S, Cu, Sb, Se, Ag, In, Pb, Cd exceeding the Clark more than hundreds and thousands of times. The composition of tails in different parts of the tailing dump varies considerably, including the content of useful components, due to different distance from the mirror of water. As a result of the impact of flotation processes, the upper 10 cm of the dry part of the beach area of the tailing dump is enriched, including highly toxic elements (Zn, As, Cu, Sb, Ni, Pb), which poses a danger to the environment and public health. The presence of useful components in the tailings indicates the need for the use of waste under consideration as a source of minerals.

Keywords: nuclear-physical methods, waste mining, ore.

PACS: 87.58

1. INTRODUCTION

In the Sadonsky ore district of the Republic of North Ossetia-Alania (RSO - Alania), about 300 vein lead-zinc deposits and ore occurrences are known. Prospecting, exploration, mining and processing of polymetallic ores have been conducted in this area since the middle of the XIX century. The entire infrastructure of mining enterprises (mines, processing plants, tailing dumps, roads) is confined to the densely populated valleys of the main water systems of the Republic [1]. In RSO-Alania, 10 million tons of metal-containing tails of Mizur and Fiagdon concentrators and metallurgical plants have been accumulated on the area of 250 hectares [2, 3]. Since 1984, waste from processing ore materials (tails) of the Mizur concentrator has been placed on the territory of the Unal tailings storage facility. The tailing dump is located in the Central part of the Alagir district, the Republic of North Ossetia-Alania, in the valley of the river Ardon, on its left bank between the villages of Unal and Zintsar. The area of the Unal tailings pond is about 0.2 km². According to [6] in Unal tailings is 2600000 t. tails with a content of lead 0.21%, zinc 0.9%, copper 0.10%, etc.

Most of the surface of the tailing dump is occupied by a pond. The storage depth ranges from 12 to 15 m. The volume of tails is about 3.2 million tons. Currently, the tailing dump has a beach area (about

40% of its area) and water-filled one (60% of the area) due to continuous irrigation with water sprinklers. The tails represent the crushed rock mass, which is similar to fine-grained dusty sand on grain-size composition. In dry hot weather, this dust gets into the air pool area from the beach area. The dust in the area of tailings ponds in summer time is more than ten times the maximum permissible concentration (MPC) [2].

According to the results of comprehensive studies on the geoecological situation in the Sadon ore district [4, 5], the decisive role of the Unal tailings in the formation of technogenic anomalies of lead on the lower terraces of the Ardon river was revealed. The purpose of this study is to analyze the elemental composition of waste from the surface of the Unal tailings.

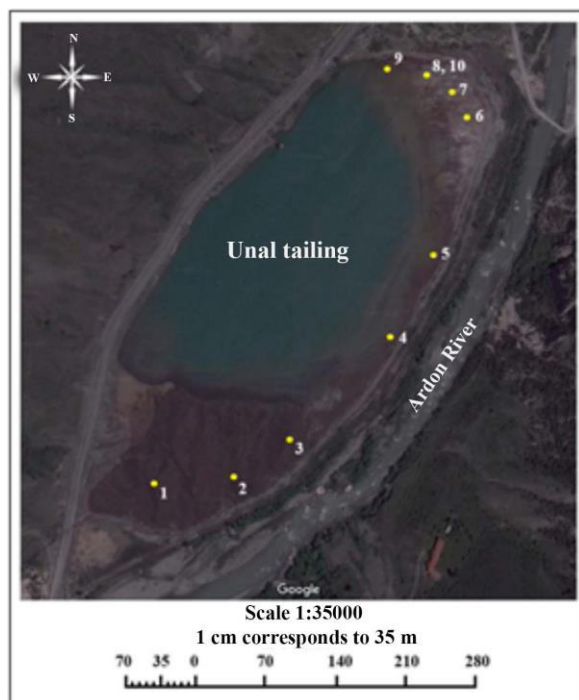
2. OBJECT AND METHODS OF RESEARCH

Sampling the surface with a dry portion of the tailings was conducted in 2015-2016. Sampling was carried out in accordance with conventional methods [7] in 10 points. Each sample was formed by mixing 5 spot samples, taken at a depth of 0-10 cm. Also in point 8 were further selected the sample from a depth of 15-20 cm. Positions of sampling points are shown in the figure.

Analytical identifications were performed at the Joint Institute for Nuclear Research (JINR) in

Dubna, Moscow region. Multi-element determination of the composition of samples by x-ray fluorescence (XRF) was carried out in The Laboratory of nuclear reactions named after G. N. Flerov (JINR FLNR), instrumental neutron activation analysis (INAA) - in the laboratory of neutron physics named after I. M. Frank (JINR FLNP). The x-ray spectra of the samples were measured using a standard Canberra spectrometer.

Ring radioisotope sources ^{109}Cd ($E = 22.16$ keV, $T_{1/2} = 453$ days) and ^{241}Am ($E = 59.6$ keV, $T_{1/2} = 458$ years) with a total activity of 20 μCi were used to excite x-ray radiation. The characteristic x-ray radiation was recorded by a semiconductor Si (Li) detector with an area of 30 mm² and a thickness of 3 mm, with a beryllium window thickness of 25 μm and a resolution of 145 eV on the 5.9 keV line. The WinAxil Canberra x-ray fluorescence analysis software was used to process spectra and calculate element concentrations. Concentrations of elements were determined by comparison with standard samples with similar matrix effects (SG-1A, GnA, soil-5, GM, Sch-ST, Fe₂O₃, etc.). The method of simultaneous determination of all elements excited by radioisotope sources in saturated layers of matter by a single calibration curves, constructed on the basis of measurements of standard samples [8], was used to determine the elements absent in the reference samples.



Instrumental neutron activation analysis (INAA) was performed at the IBR-2 reactor of the JINR LNP using a pneumatic transport unit REGATA [9]. To determine short-lived isotopes of Al, Cl, Ca, Ti, V, Mn, Cu, In elements, the samples were irradiated for 1 minute in the reactor channel with a neutron flux density of 1.3×10^{12} neutrons/(cm² • s). To determine the long-lived isotopes of elements Na, Sc, Cr, Co, Ni, As, Se, Sb, Cs, La, Ce, Tb, Ta, Ag, Th, U, the samples

were irradiated for about three days in the channel of the reactor with a cadmium screen and a flux density of resonance neutrons 1.6×10^{12} neutrons/(cm² • s). After irradiation, the samples were repackaged in clean containers for the measurement. Induced gamma activity of the samples was measured twice: 4-5 days after extraction from the irradiation channel for 45 minutes and 20 days later for 1.5 hours. The software package developed in FLNP, JINR [10] was used for processing of gamma spectra and to calculate concentrations of elements. The quality of the analysis was ensured by certified reference materials Coal fly ash (NIST, 1633c), Montana Soil (NIST, 2710), Estuarine sediment (BCR, 667), which were irradiated under the same conditions as the samples under study.

3. RESEARCH RESULTS AND THEIR DISCUSSION

The use of XRF and INAA allows us to obtain data on the content of 39 elements in the composition of mining waste (tailings of the Mizur concentrator). The content of Ca, Ti, Cr, Mn, Cu, Sb in tails was determined by two methods. The results obtained are the same within the measurement uncertainties. The results of the analytical identifications are presented in table 1.

Unal tailing dump is a technogenic geochemical anomaly with the content of a number of elements exceeding their Clarks in the earth's crust (table 1). The content of elements such as Zn, As, S, Cu exceeds the Clark concentration by more than a hundred times, the content of Sb, Se, Ag, In, Pb exceed the Clark values by thousands of times. Attention is drawn to the enrichment of technogenic formations of the Unal tailings by Cd, the content of which is more than twenty thousand times higher than its Clark in the earth's crust, while Cd is not included in the association of chemical elements (Pb, Zn, Fe, Cu, Ag, Bi, Al, Si), which are in high concentrations in lead-zinc deposits [11].

The composition of tails in different parts of the tailing dump varies considerably, including the content of useful components [12]. A significant variation in the content of a number of elements at different points of testing is probably due to different distance from the water mirror, and the impact of flotation processes. The average content (median) of elements in technogenic formations of the tailing dump (at a depth of 10 cm) is (in descending order) %: S - 13; Fe - 6,19; Zn - 4,32; Al - 3,9; Pb - 2,71; Ca - 2,5; K - 1,2; Cu - 1,1; Na - 0,92; As - 0,47; Sb - 0,39; Ba - 0,38; Ti - 0,28; Sn - 0,234; Mn - 0,21; Cr - 0,08; In - 0,07; Te - 0,056; Cd - 0,028; Cl - 0,028; Ni - 0,019; Se - 0,01; Sr - 0,0095; hereinafter in ppm: Nd - 94; Zr - 44; V - 33,7; Ce - 33; Ag - 30; La - 25; Co - 22; Th - 8; Sc - 6,4; U - 6,2; Rb - 3; Nb - 3; Ta - 1,2; Tb - 1,04; Mo - 1.

It should be noted that most of the elements present in the dry part of the tailings are toxic and highly toxic ones.

In the absence of moisture dispersed particles spread over long distances, polluting the soil, surface

water, vegetation. The greatest dangers to human health are fine particles (with a diameter less than 1 μm) as they reach the lower respiratory tract and settle in the alveoli of the lungs. The analysis of stale tails

taking into account granulometric composition [5] revealed high variability of element content. The maximum contents of Pb, Zn, Cu, As are noted in the clay fraction.

Table

The results of the analysis of Unal tailings by means of INAA and XRF methods

Elem.	Analysis Method	Depth up to 10 cm (median)	Depth 15-20 cm	By data of [3]	By data of [4]	By data of [5]
Concentration, %						
Na	INAA	0,92±0,09	0,36±0,04	0,12		
Al	INAA	3,4±0,2	4,6±0,3	5,24		
S	INAA	6,2±1,8	7±2	7,39		1,2-18,9
Cl	INAA	0,048±0,014	0,017±0,005			0,012-0,058
K	XRF	1,2±0,2	1,7±0,2	2,07		
Ca	XRF INAA	1,9±0,1	1,22±0,09	1,97		
Ti	XRF INAA	0,23±0,03	0,21±0,03	0,31	0,17	
Cr	XRF INAA	≤0,1	≤0,1		0,016	0,005-0,07
Mn	INAA	0,20±0,01	0,096±0,005		0,19	
Fe	XRF	5,83±0,03	2,34±0,02	8,86		
Cu	XRF INAA	1,1±0,3	0,08±0,02		0,04	0,04-2,74
Zn	XRF	4,32±0,01	0,758±0,005		0,235	9,03-0,18
As	INAA	0,82±0,06	0,022±0,002		0,028	0,014-0,175
Se	INAA	0,0103±0,0016	0,0040±0,0006			
Sr	XRF	0,0078±0,0003	0,0029±0,0002			0,0010-0,0069
Cd	XRF	0,028±0,0003	0,0032±0,0001		0,0006	
In	INAA	0,07±0,02	0,0005±0,0001			
Sn	XRF	0,2294±0,0003	0,0085±0,0001		0,0023	0,12-0,57
Sb	XRF INAA	0,7387±0,0002	0,1336±0,0001			0,09-3,83
Te	XRF	0,0443±0,0004	≤0,0002			
Ba	XRF	0,3857±0,0002	0,1416±0,0001			0,11-1,16
Pb	XRF	2,93±0,04	1,18±0,03		0,193	0,11-12,42
Concentration, ppm (10^{-4} %)						
Sc	INAA	6,8±1,7	7,8±2,0			
V	INAA	89±6	38±4		40	14-78
Co	INAA	29±4	12,0±1,8		28	4-13
Ni	INAA	256±77	23±7		20	4-49
Rb	XRF	≤3	90±3			
Zr	XRF	15±3	69±3		140	
Nb	XRF	2±1	6±1			
Mo	XRF	3±1	3±1		5	
Ag	INAA	30±2	5,7±0,4		4	
Cs	INAA	3,9±0,8	4,9±1,0			
La	INAA	21±5	22±6			
Ce	XRF INAA	33±3	43±2			
Nd	XRF	71±5	28±2			
Tb	INAA	2,5±0,2	0,5±0,4			
Ta	INAA	1,2±0,2	1,6±0,2			
Th	INAA	6,9±0,8	14,5±1,2			
U	INAA	6,7±1,3	5,9±1,2			

Analysis of the composition of tails selected at different depths of the tailing dump showed that on the surface of the dry part of the tailing dump there is a sharp increase in the content of such components as: Te (221 times) from 0.0002 to 0.0443 %, In (140

times), from 0.0005 to 0.07 %, As (37 times) from 0.022 to 0.82%, Sn (27 times) from 0.0085 to 0.2294 %. To a lesser extent, but significantly increases the content of Cu (13.7) from 0.08 to 1.1 %, Ni (10.8 times) from 23 to 250 ppm, Cd (8.7 times) from 32 to

280 ppm. From 5 to 5.5 times the content of Zn (5.7 times) increases from 0.758 to 4.32%, Sb (5.5 times) from 0.1336 to 0.7387%, Ag (5.2 times) from 5.7 to 30 ppm, Tb (5 times) from 0.5 to 2.5 ppm. From 2.1 to 2.8 times the content of Fe (2.5 times) increases from 2.34 to 5.83%, Ba (2.7 times) from 0.1416 to 0.3857%, Pb (2.5 times) from 1.18 to 2.93 %, Na (2.6) from 0.36 to 0.92%, Cl (2.8 times) from 0.017 to 0.048%, Mn (2.1 times) from 0.096 to 0.2 %, Se (2.6 times) from 0.004 to 2.7 times) from 29 to 78 ppm, Nd (2.5 times) from 28 to 71 ppm, V (2.3 times) from 38 to 89 ppm, Co (2.4 times) from 12 to 29 ppm. The Ca content increases slightly (1.5 times) from 1.22 to 1.9% and U (1.1 times) from 5.9 to 6.7 ppm.

The results of the analysis showed that the content of such highly toxic elements as Cd, Ni, As, Ag, Cu in samples from the surface of the beach area of the tailing dump is tens and hundreds of times higher than the data available in the literature [3, 4, 5, 6]. Deflationary processes, developing in the dry part of the beach area, pose a serious threat to the surrounding areas.

Despite the fact that the content of useful components in the composition of tailings is extremely uneven, the average content of Pb and Zn in the upper part of the beach area of the Unal tailings corresponds to ordinary ores (Pb + Zn from 7 to 4%). A radical way to protect the environment from the impact of the tailing dump is the leaching of tails with

the utilization of useful products of processing, and subsequent recultivation.

Involvement in the production of non-traditional technologies can become a priority direction of the mining industry not only in the RSA, but also in the entire North Caucasus region.

4. SUMMARY

1. The use of RF and INAA for the analysis of waste from the Mizur mining and processing plant made it possible to quantify the content of 39 elements.

2. The content of Zn, As, S, Cu, Sb, Se, Ag, In, Pb Cd in the composition of technogenic formations of the Unal tailing dump is abnormally high and exceeds the Clark values by more than hundreds and thousands of times.

3. The content of elements in the upper part of the beach zone is uneven, a significant variation in the content of a number of elements at different points of testing is probably due to different distances from the water mirror, and the impact of flotation processes.

4. The high content of highly toxic elements (Zn, As, Cu, Sb, Ni, Pb) in the surface layers of the beach area of the tailing dump poses a danger to the environment and public health.

5. The presence of useful ore components in the tailings indicate the need for recycling of waste Mizur concentrator.

-
- [1] V.I. Golik To the history of the mining and metallurgical industry in North Ossetia. V.I. Golik, D.A. Melkov, A.V. Logagev. Mining information and analytical bulletin]. 2009, № 1, pp. 194 - 199.
 - [2] V.I. Golik, E.N. Kozyrev, E.N. Klochko. Economic efficiency of prevention of natUnal and technogenic disasters in mining regions. Nauchnyi vestnik IuIM-Scientific journal of UIM, 2015, no. 3, pp. 7-13.
 - [3] G.V. Rukhlin. Mining waste as a raw material for high-tech products. G.V. Rukhlin, A.M. Baymatov. Bulletin of the North Caucasus State Technical University. 2010, №4 (25), pp. 34-39.
 - [4] E.V. Pryanichnikova. Ecological and geochemical assessment of the mining area: on the example of the Sadno-Unal basin, the Republic of North Ossetia-Alania: abstract of the thesis for the degree of candidate of geol.-mineral. Sciences (25.00.09). E.V. Pryanichnikova; Lomonosov Moscow State Uni., Geological Faculty, M., 2005, p. 27
 - [5] A.G. Gurbanov. Industrial waste of Mizur mining and processing plant of Sadon lead-zinc plant (geochemical features, assessment of their impact on the environmental situation of the surrounding areas (soil and water of the Ardon river) Rep. of North Ossetia- Alania. A.G. Gurbanov, J.K. Shazzo, A.B. Leksin, V.M. Gazeev, A.I. Dokuchaev, L.E. Tsukanova, I. Yakushev, I.S. Semenov, S.I. Isakov. Bulletin of Vladikavkaz scientific center. 2012, V.12, №4, pp. 27- 40.
 - [6] V.I. Golik, T.M. Teziev. Prospects for the revival of the mining industry of North Ossetia. Topical issues of modern science, 2016, no. 45, pp. 110-121.
 - [7] Yu.A. Karpov, A.P. Savostin. Sampling techniques and sample preparation. Moscow, Binom. Laboratoriia znani, 2015. URL: <http://files.pilotlz.ru/pdf/cC2584-9-ch.pdf>
 - [8] O.D. Maslov, M.V. Gustova, L.G. Molokanova. Multicomponent instrumental x-ray fluorescence analysis of soils and other environmental objects for toxic and related items. Enterprise standard STP 104-2002. Dubna, OIIaI, 2002, 16.
 - [9] M.V. Frontasyeva, S.S. Pavlov. REGATA Experimental Setup for Air Pollution Studies. In «Problems of Modern Physics». On the 90th anniversary of Saratov State University and the 40 years of the JINR-SSU collaboration. Editors: A.N. Sissakian, D.I. Trubetskoy. Dubna, JINR, 1999, pp. 152 - 158.
 - [10] A.Iu. Dmitriev, S.S. Pavlov. Automation of quantitative determination of elements in samples by neutron activation analysis at the reactor IBR 2 at FLNP JINR. Pisma v EChAia.

- Particles and nuclei, Letters, 2013, vol.1, №.10, pp. 58-64.
- [11] V.A. *Alekseenko*. Environmental Geochemistry. Moscow, Logos, 2000, 627.
- [12] I.Z. *Kamanina*. Use of nuclear physical methods for the analysis of waste of mining and processing industry on the example of Unal tailings. / I.Z. *Kamanina*, N.E. *Pukhaeva*, M.V. *Gustova*, M.V. *Frontasyeva*, D.N.*Chigoeva*, S.P. *Kaplina*. Successes of modern natural science, 2018, №7. pp.142-50; URL:<http://natural-sciences.ru/ru/article/view?id=36817>.

Received: 25.01.2019

THE PROCESS OF OSTWALD MATURATION ON TlGaTe₂ CRYSTAL SURFACE

K.G. KHALILOVA¹, N.M. ABDULLAYEV¹, K.Sh. KAGRAMANOV¹

G.M. Abdullayev Institute of Physics of Azerbaijan NAS

131, H. Javid ave., Baku, AZ 1143

It is shown that nano-island crystallization on TlGaTe₂ crystal surface is accompanied by their coalescence with process transition into Ostwald maturation. The analysis of conditions of Ostwald maturation (OM) stage beginning is carried out in the work. The growth mechanism on isotropic substrate on principle doesn't differ from the one on crystal substrate. The process of condensate formation is divided on following parts: germ-formation, growth and coalescence of germs, channel formation.

Keywords: coalescence, maturation process, fluctuation, Ostwald maturation

PACS: 62.20 Fe, 61.72.Cc, 61.72. Lk

1. INTRODUCTION

TlGaTe₂ semiconductor crystals belong to class of compounds of A³B³C₆ group crystallizing in tetragonal space group D_{4h}^{18} (structural type TlSe). The above-mentioned crystals present themselves Ga - Te chains extended along tetragonal C axis of crystal. This is crystal characteristics. It is obvious that the nano-formations of Ostwald maturation are responsible for changes of temperature dependence of its electric conduction [1].

According to [1 -2] the presence of wide homogeneity region of A³B³C₆ group crystals reached up to 6.8mol.% can be the reason of structure defect. The segregation coefficient in homogeneity is less than 1, that's why there is big probability of composition inclination on stoichiometry at single crystal growth. This will be cause to appearance of big amount of layer join defects, vacancies and dislocations.

The revealing of OM on TlGaTe₂ crystal surface is the aim of this work.

2. EXPERIMENT

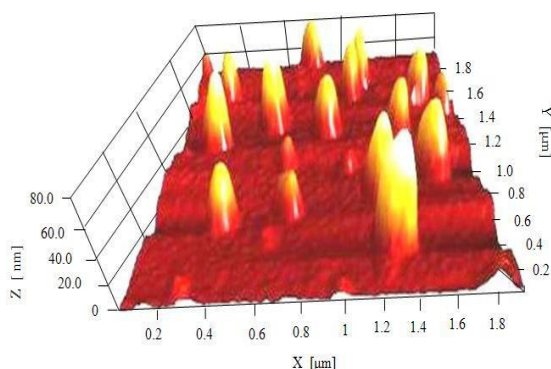


Fig.1. AFM – images in 3D-scale of nano-islands (NI) TlGaTe₂ surface being in mode of Ostwald maturation and reached the maximal height $h_{\max} = 58$ nm; $h_{\min} = 20$ nm.

The real crystals are studied in the work, the surface images obtained in atomic-force microscope (AFM) of annealed TlGaTe₂ single crystals are considered. As it is seen from the figures (fig. 1 – 6)

the obtained results evidence on the fact that the growth of new phase islands is defined by two main processes which are: substance transfer to island, i.e. the diffusion process (fig. 2) and transition of atoms through interface i.e. old phase – new phase.

The many experimental investigations show that the new phase germs comparably rapidly move on substrate surface on initial stages of atom condensation. This process is the important part in phase structure formation [1 – 3]. Such movements take place under the influence of different internal forces: collision with rapid flux particles, temperature gradient, electric and magnetic fields, drugs by movable steps and etc. According to the island migration mechanism, the only two main models describing the island movement are used until now. In first model the particle diffusion takes place only on island surface, moreover the particles fitting to interface stay immovable ones related to it.

In the second model the island is considered as sliding one on substrate surface. The concrete mechanisms of island morphological change and sliding process are suggested enough big amount, however, they are all lead to relative low values of island migration velocities and coefficients of their diffusion in comparison with real observable ones in some cases. In models of 1st type it is connected with low values of adatom self-diffusion which can't supply enough rapid island movement. In models of 2nd type this is caused by big sliding friction forces between island and substrate (i.e. high sliding activation energy) especially at epitaxial growth. Recently the quite another movement model of directly growing islands on alien substrate is suggested in work [2]. In reality, their kinetics of new phase germ-formation and filling of the condensation surface by them are the one of the important tasks of surface phase transitions by 1st order.

Designations are: the approaching NI which are able to maturation are shown by circle, the arrows show the nano-particle diffusion direction in the process of formation of Ostwald maturation.

Indeed, the growing islands absorb the adatoms and decrease the satiety on which the island formation velocity depend and velocity of their growth because of coalescence of small NI in big ones (fig. 5).

THE PROCESS OF OSTWALD MATURATION ON TlGaTe_2 CRYSTAL SURFACE

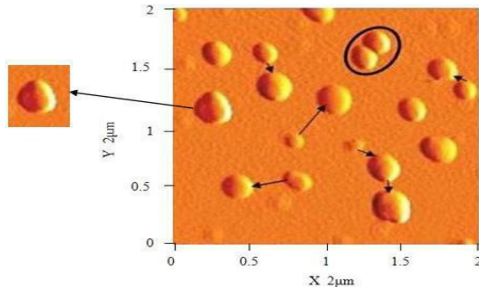


Fig.2. AFM – images in 2D scale NI in coalescence process and formation of Ostwald growth mode taking under consideration the fluctuations of particle number in germ.

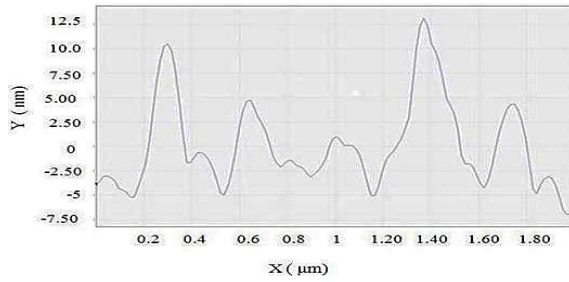


Fig.3. The profilogram of NI sizes on TlGaTe_2 surface. Designations are: height NI oscillates from 5nm up to 12.0 nm. The growth profilogram of NI evidences on their growth.

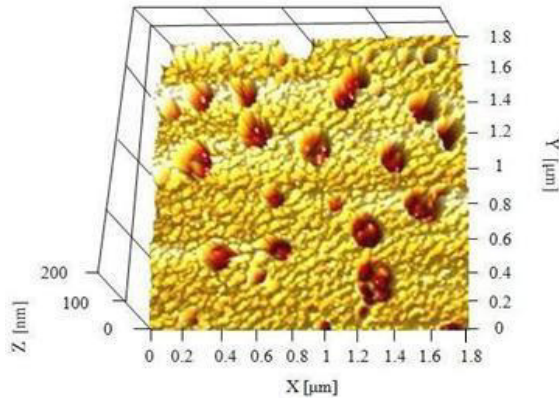


Fig.4. TlGaTe_2 coagulation nano-formations obtained in NI coalescence process.

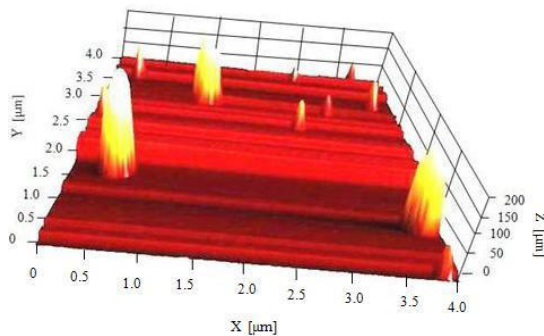


Fig.5. AFM - images NI after diffusion processes and coalescence (Ostwald NI formation process). As a result the free zone (which is seen in front part of) forms from which the small NI diffuse in Ostwald maturation bands of nano-islands.

At study of OM islands on grains of different orientation we obtain that the substance from the grains recondenses on other ones the orientation of which is the more profitable from both the thermodynamics and kinetics point of view.

The finiteness of system sizes in which the melt hardening leads to appearance of fluxes of substance and heat. If the melt overcools near boundary in some time moment and the phase transition with formation of nuclear new phase takes place in it, then the melt can be overheated far off it. In layer where the formation takes place OM stage begins. However, OM band will be in the essentially differ conditions from ones investigated above. These conditions are the result of inhomogeneous distribution of fluxes of heat and substance by the system.

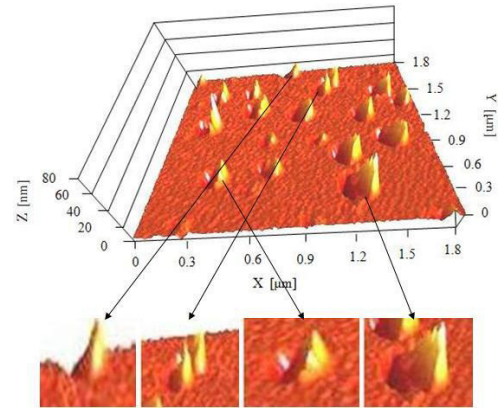


Fig.6. AFM-image of TlGaTe_2 .

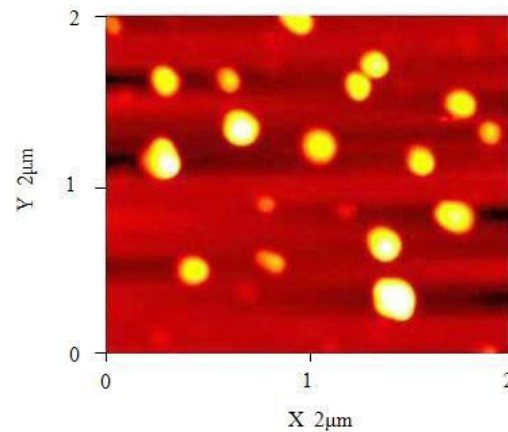


Fig.7. AFM - image in 2D scale on TlGaTe_2 basis surface. The process of big particle formation from small ones given on fig.1 is shown (process is coalescence).

From the figure it is seen the consequence of diffusion processes leading to formation of complex nano-formations (such nano-formations are beyond the limits of scanning). The all main modern theoretical conceptions and experimental results describing the both the processes of new phase formation, following evolution and NI growth processes, aren't given in description. The theory of many-component system formation requires the following development. The construction of the theory

allowing us to calculate the composition of forming films is far from the completion. The theory of steam-liquid-crystal transition taking under the inner symmetry change requires the significant investigation. The explanation of appearance reason of the different structures at the film growth from the melts from melts of eutectic composition presents the essential interest.

The condense theory in open system at power laws of growth rate on particle number and total concentration on time with arbitrary indexes [2 – 3].

3. RESULTS AND THEIR DISCUSSION

The 1st stage is the formation of small crystal germs (by diameter 0.2 – 0.5 nm) is after several seconds after condensation beginning. The germ density is very high (10^{10} - 10^{11} cm⁻²). The coalescence of the germs begins at their collision. The new germs growing up to collision with big formations after that they coalesce with them appear on substrate surface being free because of coalescence (fig. 2).

The coalescence of big islands of condensed phase carries out very hard and slowly. The filling of channels and spaces carry out by both the formation of new germs in them and the way of atom join directly from molecular beam or adsorbed layer (fig. 2).

The coalescence of small and big islands of condensed phase carries out unequally. The germs coalesce even in that case when they don't join each other. The substance transfer in this case is carried out by the way of surface diffusion by substrate. Such

germs can also move on substrate and join with each other. The islands bigger than 20nm in diameter coalesce at collision with each other by the means of surface self-diffusion and

mass transfer through contact isthmus. The volume self-diffusion carries out simultaneously. If two islands coalesce with different orientation, then the inner intergranular boundary appears. Such boundary shifts and out from merging formation by the way of volume diffusion (*AFM* - images 1 – 3). As we see the germ-formation stages, stages of separate growth of new phase germs, coalescence and last stage, i.e. Ostwald maturation on which the growth of bigger islands is carried out because of formation of small ones, are usually related to such stages. The given processes have the essentially different scales by time. The stage of formation, later the stage of separate growth and etc rapidly carry out. This time hierarchy means that rapid processes are “adapt” to slow ones.

The final stage *NI* by size 250 nm is obtained on TiGaTe_2 crystal surface.

Consequently, the coalescence on TiGaTe_2 crystal surface presents itself the merge of several islands and can be accompanied by recrystallization leading to the fact that mutually disoriented islands have the unique orientation at merging that leads to formation of biggest *NI*.

The given work is supported by Science Development Foundation under the President of the Republic of Azerbaijan - Grant № EİF/MQM/Elm-Tehsil-1-2016-1(26)-71/16/1.

-
- [1] R.M. Sardarli, O.A. Samedov, A.I. Nadjafov, A.P. Abdullayev, E.A. Zeynalova, D.G. Jabbarov. Azerbaijan National Academy of Sciences Transaction, FRTE ser, physics and astronomy, 2005, № 5, c. 45-50 (in Russian).
- [2] V.G. Dubrovskiy. Letters JTF, 2010, t.36, vip.5, p.53-61 (in Russian).
- [3] F.M. Cooney, A.K. Shekin, A.P. Grinin. UFN, 2001. T. 171, p. 345-385 (in Russian).

Received: 04.02.2019

ANALYSIS OF FLUCTUATION CONDUCTIVITY IN $Y_{0.7}Cd_{0.3}Ba_2Cu_3O_{7-\delta}$ V.M. ALIEV¹, J.A. RAGIMOV², R.I. SELIM-ZADE¹, B.A. TAIROV¹¹*G.M. Abdullayev Institute of Physics of Azerbaijan NAS**131, H. Javid ave., Baku, AZ 1143**v_aliev@bk.ru*²*Azerbaijan Medical University, 23, Bakikhanov str., Baku, AZ-1022*

The mechanism of formation of excess conductivity in cuprate HTSC $Y_{0.7}Cd_{0.3}Ba_2Cu_3O_{7-\delta}$ and $YBa_2Cu_3O_{7-\delta}$ was considered within the framework of the local pair model taking into account the Aslamazov-Larkin theory near T_c . The temperature T_0 of the transition T_0 from the 2D fluctuation region to the 3D region (the temperature of the 2D-3D crossover) is determined. The coherence lengths of the fluctuation Cooper pairs $\xi_c(0)$ along the c axis are calculated. It was shown that a partial substitution of Y by Cd in the Y–Ba–Cu–O system leads to a decrease in $\xi_c(0)$ by ~ 1.7 times (from 6.32Å to 3.8Å), as well as to the expansion as the region of existence pseudogaps and superconducting (SC) fluctuations near T_c . The temperature dependence of the pseudogap $\Delta^*(T)$ and the values of $\Delta^*(T_c)$ are determined, and temperatures T_m corresponding to the maximum temperature dependence of the pseudogap in these materials are estimated. The maximum values of the pseudogap in samples $Y_{0.7}Cd_{0.3}Ba_2Cu_3O_{7-\delta}$ and $YBa_2Cu_3O_{7-\delta}$ are, respectively, 34.56meV and 34.65meV .

Keywords: superconductivity, pseudogap, excess conductivity, coherence length, composition.**PACS:** 74.25. Fy, 74.20.Mn, 74.72. ± h, 74.25. ± q, 74.25. Jb**1. INTRODUCTION**

In recent years, the group of works [1–5] devoted to the analysis of pseudogap effects in HTSC compounds has appeared. Pseudogap (PG) is a unique phenomenon characteristic of HTSC with an active CuO_2 plane (cuprates) in the doping region less than optimal. It manifests itself in studies of the phenomena of tunneling, photoemission, heat capacity [2, 4] and other properties of HTSC. It is assumed that at a certain temperature $T^* \gg T_c$ (T_c is the critical temperature of the superconducting transition) the density of states on the Fermi surface is redistributed: on a part of this surface the density of states decreases. Below the temperature T^* , the compound is in a pseudogap state. In these works, possible conduction mechanisms in the modes of the normal, superconducting, and pseudogap states in HTSC are also discussed.

Recently, the work [6], devoted to the study of the pseudogap state in $Pb_{0.55}Bi_{1.5}Sr_{1.6}La_{0.4}CuO_{6+\delta}$ (Pb - $Bi2201$) appeared. A series of Pb - $Bi2201$ single crystals was obtained, on which a wide range of investigations were conducted to identify the pseudogap state. The results of studies on three different experimental methods indicate that the appearance of a pseudogap at $T \cong 132\text{K}$ should be perceived only as a phase transition. Thus, the authors confirmed the assumption that at the temperature decreasing, the HESC material must undergo two phase transitions: first the appearance of a pseudogap, and then a transition to the superconducting state.

However, as noted by A. Abrikosov [7], the pseudogap state cannot really be considered as some kind of new phase state of matter, since the PG is not separated from the normal state by a phase transition. So, the question of a possible phase transition at $T=T^*$ also remains open. At the same time, it can be said that a crossover occurs at $T=T^*$ [1]. Below this temperature, due to reasons not yet established to date,

the density of quasiparticle states at the Fermi level begins to decrease. Actually, for this reason, this phenomenon is called "pseudogap". For the first time, this result was obtained in experiments on the study of NMR in a weakly doped Y123 system, in which an anomalous decrease of the Knight shift [2] during cooling, which is directly related to the density of states at the Fermi level in the Landau theory, was observed.

In order to receive answers to the above questions in this work, we have analyzed the excess conductivity separated from resistive measurements on partially doped $Y_{0.7}Cd_{0.3}Ba_2Cu_3O_{7-\delta}$ with a SC transition at 85 K.

Thus, the aim of this work is to study the normal state of $YBa_2Cu_3O_{7-\delta}$ and $Y_{0.7}Cd_{0.3}Ba_2Cu_3O_{7-\delta}$ in the temperature range $T^* > T > T_c$, to determine their physical characteristics, as well as to study the possibility of the occurrence of the PG states in these compounds. The analysis was carried out on the basis of the study of excess conductivity above T_c in the framework of the local pair (LP) model [3,4] taking into account the Aslamazov – Larkin fluctuation theory [8] near T_c .

2. EXPERIMENTAL RESULTS AND THEIR PROCESSING

The method for obtaining $Y_{0.7}Cd_{0.3}Ba_2Cu_3O_{7-\delta}$ is described in [9].

The temperature dependences of the specific resistivity ρ of the samples Y1 and Y2 are showed in fig.1.

The critical temperatures of the SC transition T_c were determined from the maximum obtained by differentiation of the curve $\rho(T)$. Critical temperature of investigated samples is $T_{c1}=92.63\text{K}$ (Y1) and $T_{c2}=90.9\text{K}$ (Y2), respectively (fig.1). In this case, the

resistivity of the sample $Y_{0.7}Cd_{0.3}Ba_2Cu_3O_{7-\delta}$ in the normal phase at 300K increases almost 2 times compared to $YBa_2Cu_3O_{7-\delta}$.

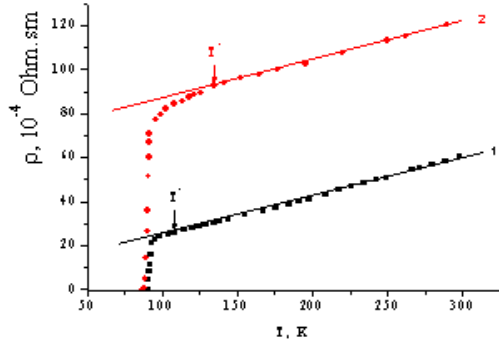


Fig.1. Temperature dependences of the resistivity of samples Y1- $YBa_2Cu_3O_{7-\delta}$ (1) and Y2- $Y_{0.7}Cd_{0.3}Ba_2Cu_3O_{7-\delta}$ (2).

3. FLUCTUATION CONDUCTIVITY

The linear course of the temperature dependence of the specific resistance of samples Y1 and Y2 in the normal phase is well extrapolated by the expressions $\rho_n(T) = (D + \kappa T + BT^2)$ and $\rho_n(T) = (\rho_0 + \kappa T + BT^2)$ (here D , B and k are some constants). This linear relationship, extrapolated to the low temperature range, was used to determine excess conductivity $\Delta\sigma(T)$ according to:

$$\Delta\sigma(T) = \rho^{-1}(T) - \rho_v^{-1}(T) \quad (1)$$

The analysis of the behavior of excess conductivities was carried out in the framework of the local pair model [4, 10].

Assuming the possibility of the formation of local pairs [3,4] in samples at temperatures below $T^* = 107.57$ K (Y1) and $T^* = 140.24$ K (Y2), the experimental results obtained near T_c were analyzed taking into account the occurrence of fluctuation Cooper pairs (FCP) above T_c in the framework of the theory of Aslamazov-Larkin (AL) [8].

The fig. 2 shows dependence of the logarithm of the excess conductivity of the samples Y1 (1) and Y2 (2) on the logarithm of the reduced temperature $\varepsilon = (T / T_c - 1)$.

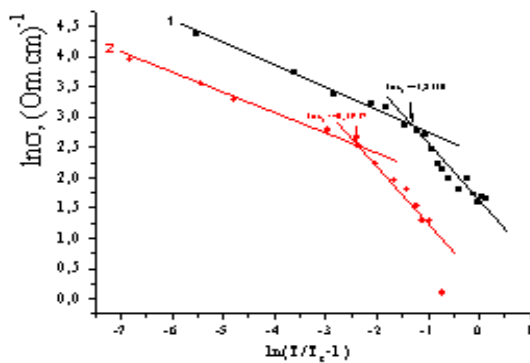


Fig. 2. The dependences of the logarithm of excess conductivity on logarithm $(T / T_c - 1)$ of samples Y1 (1) and Y2 (2).

The solid lines are the calculation in the framework of the Aslamazov-Larkin theory. According to the theory of AL, as well as Hikami – Larkin (HL) developed for HTSC [10], in the region of $T > T_c$ (but near T_c), the fluctuation coupling of charge carriers occurs, leading to the appearance of fluctuation conductivity (FC). In this region, the temperature dependence of excess conductivity on temperature is described by the expressions:

$$\Delta\sigma_{AL3D} = C_{3D} \cdot \{e^2 / [32\hbar\xi_c(0)]\} \varepsilon^{-1/2}, \quad (2)$$

$$\Delta\sigma_{AL2D} = C_{2D} \cdot \{e^2 / [16\hbar d]\} \varepsilon^{-1}, \quad (3)$$

respectively for three-dimensional (3D) and two-dimensional (2D) region. The scaling coefficients C are used to combine the theory with experiment [4].

Thus, by the angle of inclination α of dependences $\ln(\Delta\sigma)$ as a function of $\varepsilon = \ln(T/T_c - 1)$ (see fig. 2), we can distinguish 2D ($\text{tg}\alpha = -1$) and 3D ($\text{tg}\alpha = -1/2$) regions of phase transition. It can also determine the crossover temperature T_0 (the transition temperature from $\Delta\sigma_{2D}$ to σ_{3D}) and the tangents of the slopes of the dependences $\Delta\sigma(T)$ corresponding to the exponents ε in equations (2) and (3). The corresponding values of the parameters 2D and 3D regions determined from the experiment for sample Y1 are 2D ($\text{tg}\alpha = -1.04$) and 3D ($\text{tg}\alpha = -0.44$) and for Y2 2D ($\text{tg}\alpha = -1.1$) and 3D ($\text{tg}\alpha = -0.49$).

On basis of temperature of the crossover T_0 , which corresponds to $\ln\varepsilon_0$, according to fig.2, it can determine the coherence length of local pairs along the “c” axis [11,12]:

$$\xi_c(0) = d\sqrt{\varepsilon_0}, \quad (4)$$

here $d \approx 11.7\text{\AA}$ is the distance between the inner conducting planes in Y-Ba-Cu-O [13]. The values of $\xi_c(0) = 6.32\text{\AA}$ ($\ln\varepsilon_0 \approx -1.2318$) for Y1 and $\xi_c(0) = 3.535$ ($\ln\varepsilon_0 \approx -2.3937$) for Y2 was obtained, accordingly.

4. ANALYSIS OF THE MAGNITUDE AND TEMPERATURE DEPENDENCE OF THE PSEUDOGAP

As noted above, in the cuprates at $T < T^*$, the density of electron states of quasiparticles on the Fermi level decreases [14] (the cause of this phenomenon is not yet fully elucidated), which creates conditions for the formation of a pseudogap in the excitation spectrum and it leads ultimately to the formation of an excess conductivity. The magnitude and temperature dependence of the pseudogap in the investigated samples was analyzed using the local pair model, taking into account the transition from Bose-Einstein condensation (SCB) to the BCS mode predicted by the theory [10] for HTSC when the temperature decreases in the interval $T^* < T < T_c$. Note that excess conductivity exists precisely in this temperature range, where fermions supposedly form pairs -the so-called strongly coupled bosons (PRS).

The pseudogap is characterized by a certain value of the binding energy $\varepsilon_b \sim 1/\xi^2(T)$, causing the creation of such pairs [10,13], which decreases with temperature, because the coherence length of the Cooper pairs $\xi(T) = \xi(0)(T/T_c - 1)^{-1/2}$, on the contrary, increases with decreasing temperatures. Therefore, according to the LP model, the SCB are transformed into the FCP when the temperature approaches T_c (BEC-BCS transition), which becomes possible due to the extremely small coherence length $\xi(T)$ in cuprates.

From our studies, we can estimate the magnitude and temperature dependence of PG, based on the temperature dependence of excess conductivity in the entire temperature range from T^* to T_c according to [3,13]:

$$\Delta\sigma(\varepsilon) = \left\{ \frac{A(1 - T/T^*)[\exp(-\Delta^*/T)]e^2}{16\eta\xi_c(0)\sqrt{2\varepsilon_0^*} \cdot sh(2\varepsilon/\varepsilon_0^*)} \right\} \quad (5)$$

where the $(1 - T/T^*)$ determines the number of pairs formed at $T \leq T^*$; and the $\exp(-\Delta^*/T)$ determines the number of pairs destroyed by thermal fluctuations below the BEC-BCS transition temperature. The coefficient A has the same meaning as the coefficients C3D and C2D in (2) and (3).

The solution of equation (5) gives the value of Δ^* :

$$\Delta^*(T) = T \cdot \ln \left\{ \frac{A(1 - T/T^*)e^2}{\Delta\sigma(T)16\eta\xi_c(0)\sqrt{2\varepsilon_0^*} \cdot sh(2\varepsilon/\varepsilon_0^*)} \right\} \quad (6)$$

where $\Delta\sigma(T)$ is the experimentally determined excess conductivity.

Fig. 3 shows the dependence of logarithm of the excess conductivity of samples Y1 and Y2 on the inverse temperature.

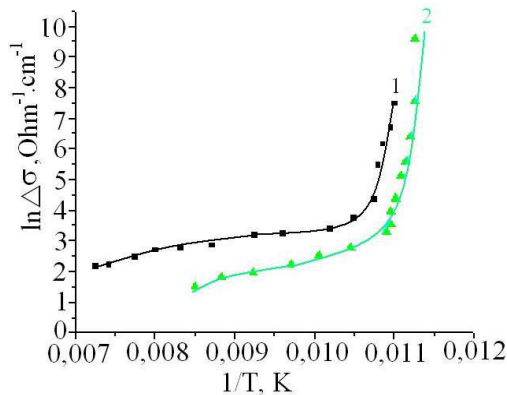


Fig.3. The dependences of logarithm of excess conductivity on inverse temperature: 1-Y1; 2-Y2; solid lines - approximation of equation 3 with the parameters given in text.

The choice of such coordinates is due to the strong sensitivity of the linear region $\ln\Delta\sigma(1/T)$ to the value of $\Delta^*(T_c)$ in equation (5), which allows us to estimate this parameter with high accuracy (this is

necessary to find the coefficient A) [3,13,15]. The dependences $\ln\Delta\sigma(1/T)$ were calculated according to the method approved in [12]. As can be seen from fig. 3 (curves 1 and 2), in this case, the values $\ln\Delta\sigma(1/T)$ calculated for both samples with parameters: $A = 82.4 \pm 0.1$, $T^* = 107.57$ K, $\xi_c(0) = 6.32$ Å (Y1) and $A = 7.6 \pm 0.1$, $T^* = 140.24$ K, $\xi_c(0) = 3.535$ Å (Y2) are in good agreement with the experimental data.

The temperature dependence and the value of the pseudogap parameter $\Delta^*(T)$ (fig. 4) were calculated on the basis of equation (6) with the parameters given above.

As noted in [3,4,13], the value of the coefficient A is selected from the condition of coincidence of the temperature dependence of $\Delta\sigma$ (equation (5), assuming $\Delta^* = \Delta^*(T)$) with experimental data in the region of 3D fluctuations near T_c . According to [13,16] the optimal approximation for the HTSC material is achieved with values of $2\Delta^*(T_c)/\kappa_B T_c \approx 5 \div 7$. For sample Y1, the values $2\Delta^*(T_c)/\kappa_B T_c = 5.4$, and for Y2 $2\Delta^*(T_c)/\kappa_B T_c = 5$ have been obtained. As a result, the values of $A = 82.4$ and $\Delta^*(T_c) = 92.62 \cdot 2.7 = 250.07$ K; for Y2 $A = 7.6$ and $\Delta^*(T_c) = 90.9 \cdot 2.5 = 227.25$ K have been obtained, and it consistent with the experimental data (fig. 4).

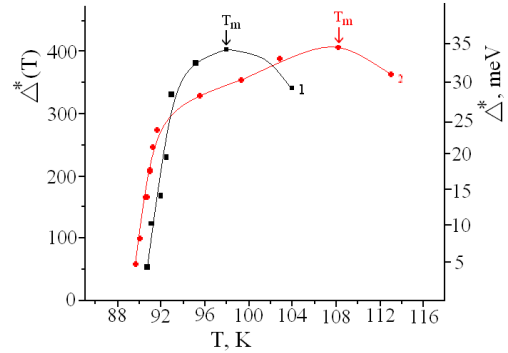


Fig.4. Temperature dependences of the calculated pseudogap of samples Y1 (1) and Y2 (2) with the parameters given in the text. The arrows show the maximum pseudogap values.

The temperature dependences of $\Delta^*(T)$ obtained on the basis of equation (6) are shown in fig. 4. The maximum values of the pseudogap for Y1 $\Delta^*_m \approx 34.56$ meV ($\Delta^*(T_m) \approx 402.66$ K, $T_m = 97.98$ K) for Y2 $\Delta^*_m \approx 34.65$ meV ($\Delta^*(T_m) \approx 406.0$ K, $T_m \approx 108.15$ K) are determined.

From the presented data in fig. 4, it is also seen that as T decreases, the pseudogap value first increases, then, after passing through a maximum, decreases. This decrease is due to the transformation of the SCB in the PCF as a result of the BEC-BCS transition, which accompanied by an increase in excess conductivity at $T \rightarrow T_c$. Such a behavior of Δ^* with decreasing temperature was first found on YBCO films [3.13] with different oxygen contents, which seems to be typical of cuprate HTSC [13]. Thus, it can be concluded that in investigated $Y_{0.7}Cd_{0.3}Ba_2Cu_3O_{7-\delta}$ and $YBa_2Cu_3O_{7-\delta}$ samples, it is possible to formed local pairs of charge carriers at

$T \gg T_c$, which creates conditions for the formation of a pseudogap [13,16] the subsequent establishment of the phase coherence of the fluctuating Cooper pairs at $T < T_c$ [17].

5. CONCLUSION

The investigation of the effect of partial substitution of Y by Cd on the mechanism of excess conductivity in Y-Ba-Cu-O polycrystals showed that partial substitution of Y by Cd leads to a decrease in the critical temperatures of the $Y_{0.7}Cd_{0.3}Ba_2Cu_3O_{7-\delta}$ (Y2) sample compared to $YBa_2Cu_3O_{7-\delta}$ (Y1) (respectively T_c (Y2) = 90.9 K and T_c (Y1) = 92.628K). In this case, the resistivity of the sample $Y_{0.7}Cd_{0.3}Ba_2Cu_3O_{7-\delta}$ in the normal phase at 300K increases (2 times) compared to $YBa_2Cu_3O_{7-\delta}$. At the same time, there is an expansion of the temperature regions of PS and FLP, as well as a decrease in the coherence length of Cooper pairs.

Studies and analysis have shown that the excess conductivity $\Delta\sigma(T)$ in $Y_{0.7}Cd_{0.3}Ba_2Cu_3O_{7-\delta}$ in the

temperature range $T_c < T < T^*$ is satisfactorily described in the framework of the model of local pairs [3,14].

The analysis result of the pseudogap state by the method of excess conductivity confirmed that the model of local pairs in this case is applicable to both samples. At $T \rightarrow T_c$, the behavior of $\Delta\sigma(T)$ of both samples obeys the Aslamazov – Larkin theory for 2D and 3D fluctuations [8, 11]. Thus, before the transition to the superconducting state, the region of superconducting fluctuations is always realized in the form of a PCF, in which $\Delta\sigma(T)$ is described by equation (2) for 3D superconductors (that is, before the SP transition, the HTSC transition is always three-dimensional).

Thus, it can be assumed that in $YBa_2Cu_3O_{7-\delta}$ and $Y_{0.7}Cd_{0.3}Ba_2Cu_3O_{7-\delta}$ PG is formed by converting the d-wave SC of the energy gap in CuO_2 planes into the corresponding gap of the fluctuation Cooper pairs above T_c .

-
- | | |
|--|---|
| <p>[1] E.B. Amitin, K.R. Jdanov, A.G. Blinov, et al. FNT, 31, 4, 323-326, 2005 (in Russian).</p> <p>[2] M.V. Sadvovskiy. UFN, 171, 539-564, 2001 (in Russian).</p> <p>[3] M.R. Trunin. UFN, 175, 10, (2005), 1017-1037, 2005 (in Russian).</p> <p>[4] A.L. Solovyov, V.M. Dmitriyev. FNT, 32, 6, 753 - 760, 2006 (in Russian).</p> <p>[5] A.L. Solovjov, M.A. Tkachenko, R.V. Vovk, A. Chreneos. Fizika C, 501, 24-31, 2014 (in Russian).</p> <p>[6] He Rui-Hua, M. Hashimoto, H. Karapetyan et al. Science, 331, 1579 - 1583, 2011.</p> <p>[7] A.A. Abrikosov. UFN, 174, 11, 1233-1239, 2004 (in Russian).</p> <p>[8] L.G. Aslamazov and A.L. Larkin. Phys. Lett., 26A, 6, 238-239, 1968.</p> <p>[9] S.A. Aliev, S.S. Ragimov, V.M. Aliev. Fizika, 2004, 10, 4, 42 - 43, 2004</p> | <p>[10] V.M. Loktev, V.M. Turkowski. Low temperature physics 30, 3, 247-260, 2004 (in Russian).</p> <p>[11] S. Hikami, A.I. Larkin. Modern Phys. Lett, v. B2, 693-697, 1988 (in Russian).</p> <p>[12] Oh B., Char K., Kent A.D. et al. Phys. Rev. B 37, 13, 7861 - 7864, 1988.</p> <p>[13] A.L. Solovyov, V.M. Dmitriyev. FNT, 35, 3, 227-264, 2009 (in Russian).</p> <p>[14] A.A. Kordyuk. FNT, 41, 5, 417 - 444, 2015 (in Russian).</p> <p>[15] D.D. Prokofyev, M.P. Volkov, Y.A. Boykov. FTT, 45, 7, 1168-1176, 2003 (in Russian).</p> <p>[16] V.V. Florentyev, A.V. Inyushkin, A.N. Taldenkov, et al., Superconductivity: physics, chemistry, technique, 3, 10, v.2, 2302-2319, 1990 (in Russian).</p> <p>[17] R. Peters and J. Bauer. Phys. Rev. B 92, 014511 – Published 22 July, 2015.</p> |
|--|---|

Received: 06.02.2019

STRUCTURE STUDY OF Se-As CHALCOGENIDE GLASSY SEMICONDUCTOR SYSTEM DOPED BY EuF_3 IMPURITYS. N. GARIBOVA^{1,2}, A.I. ISAYEV¹, S.I. MEKHTIYEVA¹, S.U. ATAYEVA¹,
S.S. BABAYEV¹, Y.R. ALIYEVA¹, N.T. HASANOV¹¹*G.M. Abdullayev Institute of Physics of Azerbaijan NAS
131, H. Javid ave., Baku, AZ 1143*²*Department of Physics and Electronics, Khazar University
41, Mehseti str., AZ1096, Baku Azerbaijan
sevdaqaribova@physics.ab.az*

The local structure and surface morphology of film samples of chalcogenide glassy semiconductor (CGS) $\text{Se}_{95}\text{As}_5$ and $\text{Se}_{95}\text{As}_5(\text{EuF}_3)_x$ ($x=0.01\div 1$ at%) have been studied by X-ray diffraction, Raman scattering and atomic-force microscopy. The “quasi-period” of the structure, the correlation length, the structural elements and chemical bonds that form the amorphous matrix, and the surface morphology of the films of the CGS materials studied have been determined. Interpretation of results obtained has been carried out within the framework of the Elliot voids-cluster model, taking into account the chemical activity of europium ions and the peculiarities of their distribution.

Keywords: amorphous, x-ray diffraction, Raman spectrum, non-crystalline semiconductor, disorder.

PACS: 72.80.Ng, 61.10.Nz, 68.35.Ct, 71.23.An, 01.30.Vv, 68.37.Ps

1. INTRODUCTION

Chalcogenide glasses are promising optical materials for creating devices for fiber and integrated optics, as well as for use in information processing systems. This is due to low losses in the transmission band, with a high refractive index ($\sim 2\text{--}4.5$), transparency in the IR spectral region ($\sim 0.5\text{--}12\ \mu\text{m}$) and photosensitivity, with high values of nonlinear optical parameters, together with the ability to change the physicochemical properties by variation of the composition, and doping [1-3]. It is known that the electronic properties of CGS material are controlled by negative effective correlation energy (so called U^- centers), the beneficial states of which are D^+ and D^- centers with two holes and electrons, respectively [4]. It is possible to change the relative concentration of D^+ and D^- centers by doping with impurities manifested in the form of ions. For this purpose, it is advisable to use rare-earth elements [5], since they mainly manifest themselves as positive ions. In non-crystalline materials, the order in the arrangement of atoms is performed only on a scale covering areas of the order of tens angstroms, there are a short and medium range order of an atoms. Therefore, structure studies of CGS materials consist in determining the short and medium order to which the presented work is devoted.

In this paper the structure of the $\text{Se}_{95}\text{As}_5$ and $\text{Se}_{95}\text{As}_5(\text{EuF}_3)_x$ ($x=0.01\div 1$ at%) chalcogenide glassy semiconductor (CGS) by the methods of X-ray diffraction, Raman scattering and atomic force microscopy have been investigated. The choice of this composition as a research object is due to the fact that replacing part of the selenium atoms with arsenic atoms whose coordination number is greater than that of selenium results in partial destruction of the Se_8 rings, stitching the ends of the chain molecules and branching of the chain structure. At the same time, the

average value of the coordination number increases and the crystallization-resistant glassy material with stable matrix is obtained. Advantage of study of such objects is due to the fact that the determined parameters of the local structure will be stable, which will make it possible to express promising areas of their application. The use of EuF_3 for doping is due to the fact the Eu, as a chemically active element, can form new structural elements with selenium atom, as well as participating, as a positive ion will contribute to a change in the relative concentration of charged centers, which will affect its electronic properties. This will help to find ways for the practical application of the specified CGS material successfully, i.e. to expand its use.

2. EXPERIMENTAL AND SAMPLE PREPARATION

The samples were obtained by fusing elementary substances of special purity in vacuumed to 10^{-3} Torr quartz cells. The synthesis was carried out at a temperature of 1200 K for 10 hours in a rotating furnace followed by cooling in the off-furnace mode with a holding time of at least 5 hours. The impurity concentration was used within $0.001\div 1$ at %. Samples for measurements were films of thickness $0.5\ \mu\text{m}\div 2\ \text{mm}$. The films were fabricated by thermal evaporation at rate of $0.2\text{--}0.5\ \mu\text{m/s}$ in a vacuum of 10^{-4} Torr onto cold glass substrates. The Raman spectra were studied on a three-dimensional confocal Raman microscope Nanofinder 30 (Tokyo Instr.) with the excitation wavelength 532nm . The radius of the laser beam incident on the film was $\sim 4\ \mu\text{m}$. The radiation receiver was a cooled CCD camera (-70°C) operating in the photon counting mode, an exposure time of 20 s with a laser power of 4 mW, and an error in the spectral

resolution of 0.5 cm^{-1} . The x-ray analysis was performed using the D2Phaser diffractometer “Bruker” and using CuK α -rays ($\lambda = 1,5406 \text{ \AA}$) at $2\theta = 5^\circ$ - 80° angular interval. Structural studies, calculations were performed on EVA and TOPAZ programs. The surface morphology of the films has been investigated by atomic-force microscope. All experiments were carried out at room temperature.

3. RESULTS AND DISCUSSION

In this paper, the structure of film samples of $\text{Se}_{95}\text{As}_5$ and $\text{Se}_{95}\text{As}_5(\text{EuF}_3)_x$ ($x=0.01 \div 1 \text{ at\%}$) chalcogenide glassy semiconductor have been studied by X-ray diffraction, Raman scattering and atomic force microscopy. Fig. 1 indicates the angular distributions of X-ray diffraction intensity for 8 \mu m thick film samples $\text{Se}_{95}\text{As}_5$, $\text{Se}_{95}\text{As}_5(\text{EuF}_3)_{0.25}$, $\text{Se}_{95}\text{As}_5(\text{EuF}_3)_1$ in the range of diffraction angles 2θ from 5 to 80° (θ is the Bragg angle). It can be seen that the general shape of these patterns is the same for pure and doped by EuF_3 impurity for glassy system Se-As. In the range of X-ray diffraction patterns (from 5° to 80°), the glasses look similar because they exhibit two halo (or broad) diffraction peaks located at different values of 2θ between 18° - 38° and 46° - 60° , where the broad highs indicate their amorphous.

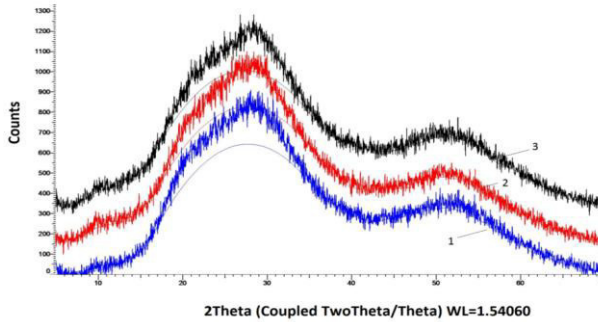


Fig.1. X-ray diffraction patterns of glassy films 1 - $\text{Se}_{95}\text{As}_5$, 2 - $\text{Se}_{95}\text{As}_5(\text{EuF}_3)_1$, 3- $\text{Se}_{95}\text{As}_5(\text{EuF}_3)_{0.25}$

X-ray diffraction patterns of CGS, as in most other glasses [6-8], has a narrow maximum, the so-called first sharp diffraction peak (FSDP), which

differs from others by an anomalous temperature dependence and pressure [9-12]. FSDP on the x-ray diffraction patterns of CGS is usually associated with the existence of ordering on the scales of medium order [6, 13–18]. For glassy materials with tetrahedral structural units, Elliott proposed the void –cluster model [13,14]. According to this model, in such materials, groups of atoms forming clusters are separated from each other by voids or regions with a reduced atomic density. According to [20], a void-cluster model is acceptable for most CGSs. Due to the mutual repulsion of electrons of solitary pairs on the chalcogen atoms, they have a low packing density, and the presence of voids is a characteristic feature of their structure. In this regard, the analysis of the results on x-ray diffraction in the region corresponding to the FSDP was carried out within the framework of the nanostructured features of chalcogenide glasses. Structure parameters, i.e. R - “quasi-period” of structure or atomic density fluctuations [13,14,20], the repeatability of which in a certain region of correlation may cause the appearance of FSDP, L is the correlation length (size of MRO regions) in which the periodicity of the fluctuations of atoms is maintained, were calculated according to the formulas [17]

$$R \approx 2\pi/Q_1, \quad (1)$$

$$L \approx 2\pi/\Delta Q_1, \quad (2)$$

where Q_1 is the value of the scattering vector, corresponding to the position of FSDP and defined by the formula $Q_1 = 4\pi \sin \theta / \lambda$, ΔQ_1 is the width corresponding to half the amplitude of the FSDP maximum. The obtained values of the parameters characterizing the FSDP and the structure of the films studied are listed in the table. Using the formula proposed in [11,15] and connecting the position of the FSDP Q_1 with the diameter of the nanovoids (D),

$$Q_1 = 2\pi/D, \quad (3)$$

we estimated the values of D . The results obtained are also presented in the table.

Table

The values of the parameters of the short range and medium orders of pure and doped by EuF_3 impurity of $\text{Se}_{95}\text{As}_5$ glassy semiconductor

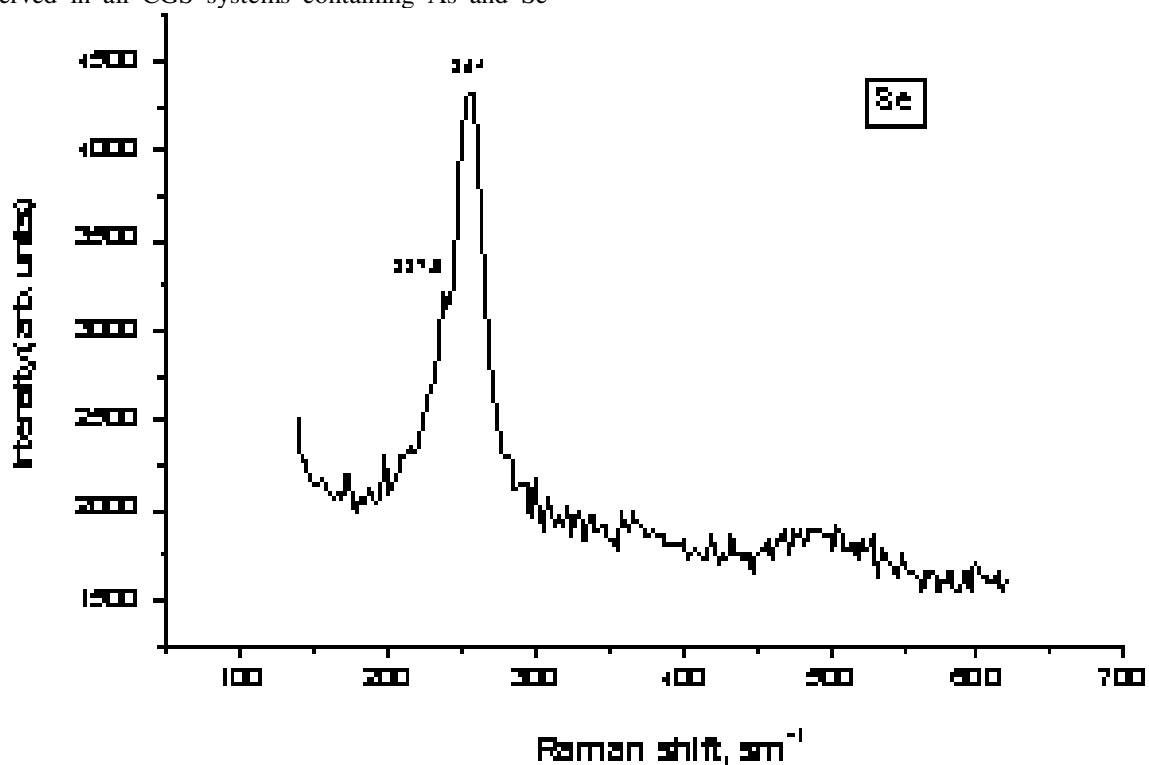
$X\text{CII}$	$2\theta, ^\circ$	$F\text{WHH}, ^\circ$	$Q_1, \text{\AA}^{-1}$	$\Delta Q_1, \text{\AA}^{-1}$	$R, \text{\AA}$	$L, \text{\AA}$	$D, \text{\AA}$
$\text{Se}_{95}\text{As}_5$	28,05	13,895	1,9763	0,9597	3,1776	6,54437	3,654
$\text{Se}_{95}\text{As}_5+0.25\text{at\%EuF}_3$	27,536	13,628	1,9408	0,9418	3,2357	6,668	3,7211
$\text{Se}_{95}\text{As}_5+1\text{at\%EuF}_3$	26,837	14,819	1,8924	1,0406	3,3184	6,0349	3,81619

The authors [10] analyzed the formulas proposed by various researchers [13,14] to determine the distances of interatomic correlations or distances between voids, and showed that, in all cases, the results obtained are close to the values of the diameter of voids obtained from formula (3).

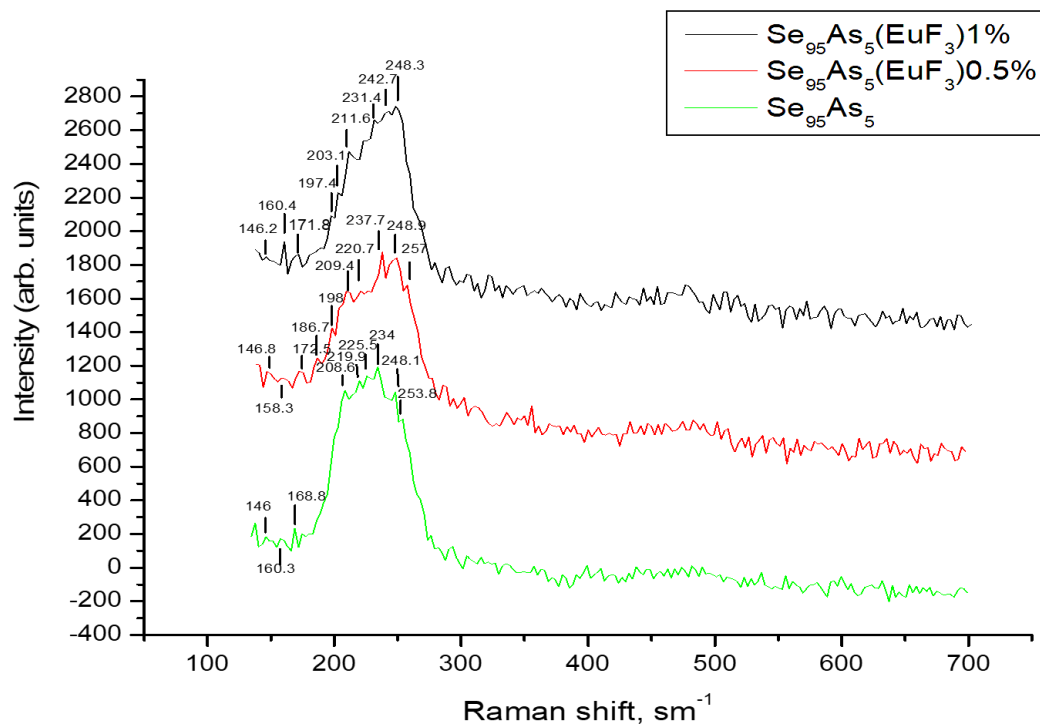
Fig. 2 shows the Raman spectrum of amorphous selenium (fig. 2a) and $\text{Se}_{95}\text{As}_5(\text{EuF}_3)_x$ ($x=0;0.5;1 \text{ at\%}$) systems films (fig. 2b). The spectrum of amorphous selenium consists of a wide at 254 cm^{-1} and narrow maximum at 236.8 cm^{-1} frequency corresponding to the vibration of Se_8 ring molecules and –Se-Se- chain

molecules [21, 22]. Doping selenium by arsenic the maximum at 254 cm^{-1} (curve 1 in fig. 2b) is weakened which is due to the rupture of part of the ring molecules. The emerging peaks in the frequency range of $209\div 220 \text{ cm}^{-1}$ are associated with the As_4Se_4 type of molecular fragment, and the peak 225 cm^{-1} also observed in all CGS systems containing As and Se

atoms and is attributed to the AsSe_3 structural elements [21,23]. The weak peak at 170 cm^{-1} is observed in all spectra shown in fig. 2b which is the associated with oscillations of homopolar coupling As – As [24].



a)



b)

Fig. 2. Raman spectra of the Se (a) and glassy systems Se- As, Se-As- EuF_3 (b)

Adding of EuF_3 impurity in the $\text{Se}_{95}\text{As}_5$ system leads to change in the spectra (curve 2 and 3 in fig. 2b). The peak at 254 cm^{-1} disappears completely, which is apparently due to the fact that europium, as chemically active, more effectively causes destruction of ring molecules and forms bridging bonds between the chains, promotes the polymerization of macromolecules, stitches the ends of polymer chains into a pyramidal structure. Europium due to its high chemical activity has a stronger effect on the structure than arsenic atoms and contributes to the establishment of grid-chain structure. New peaks appearing in the frequency range $170 \div 240\text{ cm}^{-1}$ appear to be related to the formation of the new structural elements with the participation of europium atoms, since europium as chemically active element in different structural elements can replace arsenic.

For defining of the electronic processes mechanism and the use of the film for practical purposes, an important role is played by the structure and quality of the surface. For this purpose, the effect of the EuF_3 impurity on the relief and surface

properties of $\text{Se}_{95}\text{As}_5$ has been investigated. In fig. 3 shows the AFM 3D image of the relief of the $\text{Se}_{95}\text{As}_5$ CGS composition (a) and $\text{Se}_{95}\text{As}_5(\text{EuF}_3)_x$ ($x=0.01; 0.1\text{ at.}\%$) (b,c). The AFM study of the relief shows that the relief of the samples varies greatly when the impurity of the rare-earth compound EuF_3 is introduced into the initial $\text{Se}_{95}\text{As}_5$ composition. The relief of the $\text{Se}_{95}\text{As}_5$ samples containing EuF_3 is gradually smoothed out. As can be seen, from fig. 3(c) the surface becomes even smoother with increasing EuF_3 content. This gives us reason to judge that EuF_3 at a high content (0.5-1at%) leads to the formation of a homogeneous surface of the sample. It can be seen that the surface of the composition $\text{Se}_{95}\text{As}_5$ and $\text{Se}_{95}\text{As}_5(\text{EuF}_3)_x$ ($x=0.01; 0.1\text{ at.}\%$) is different, that is, structural changes occur [17].

The histogram of the surface heterogeneity (fig. 4) shows that the introduction of EuF_3 into the $\text{Se}_{95}\text{As}_5$ composition smoothes the relief of the sample. It is also shown that the *rms* roughness of the surface of the sample $\text{Se}_{95}\text{As}_5$ is 50-250 nm, $\text{Se}_{95}\text{As}_5(\text{EuF}_3)_{0.01}$ is 100-300 nm, and for the $\text{Se}_{95}\text{As}_5(\text{EuF}_3)_{0.1}$ is 150-250 nm.

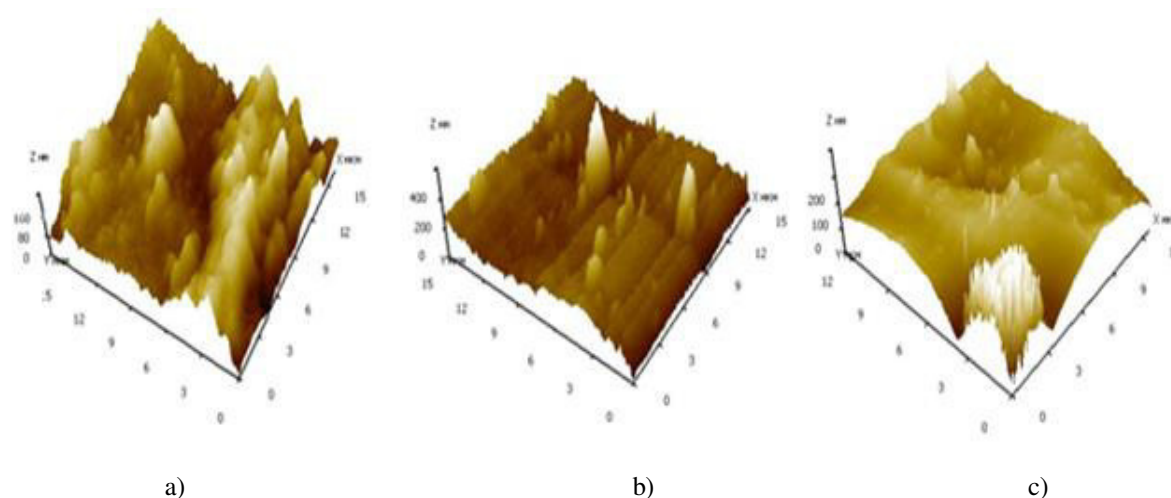


Fig.3. AFM 3D relief image of the $\text{Se}_{95}\text{As}_5$ (a), $\text{Se}_{95}\text{As}_5(\text{EuF}_3)_{0.01}$ (b), $\text{Se}_{95}\text{As}_5(\text{EuF}_3)_{0.1}$ (c)

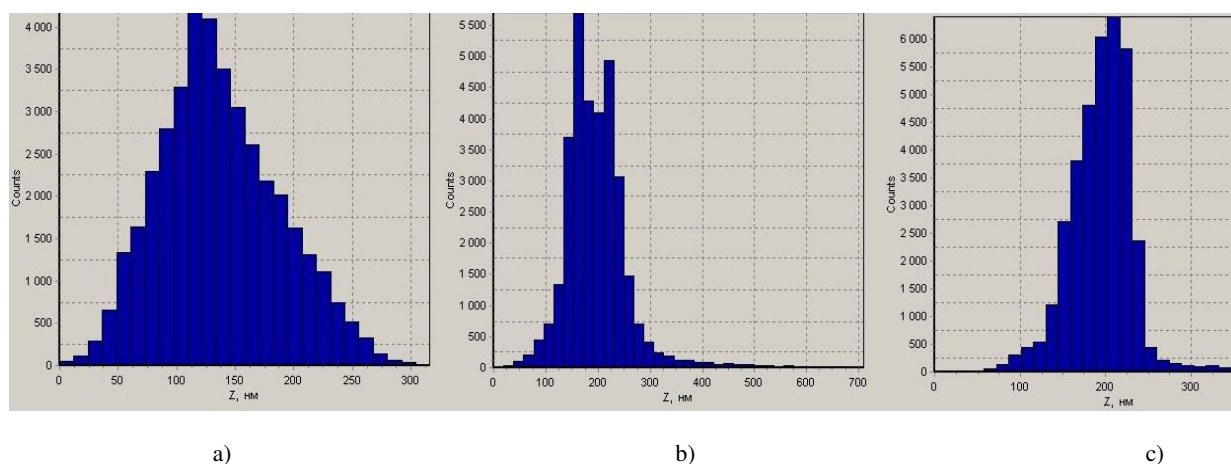


Fig.4. The histogram of the values of the image elements and the surface roughness of $\text{Se}_{95}\text{As}_5$ (a), $\text{Se}_{95}\text{As}_5(\text{EuF}_3)_{0.01}$ (b), $\text{Se}_{95}\text{As}_5(\text{EuF}_3)_{0.1}$ (c)

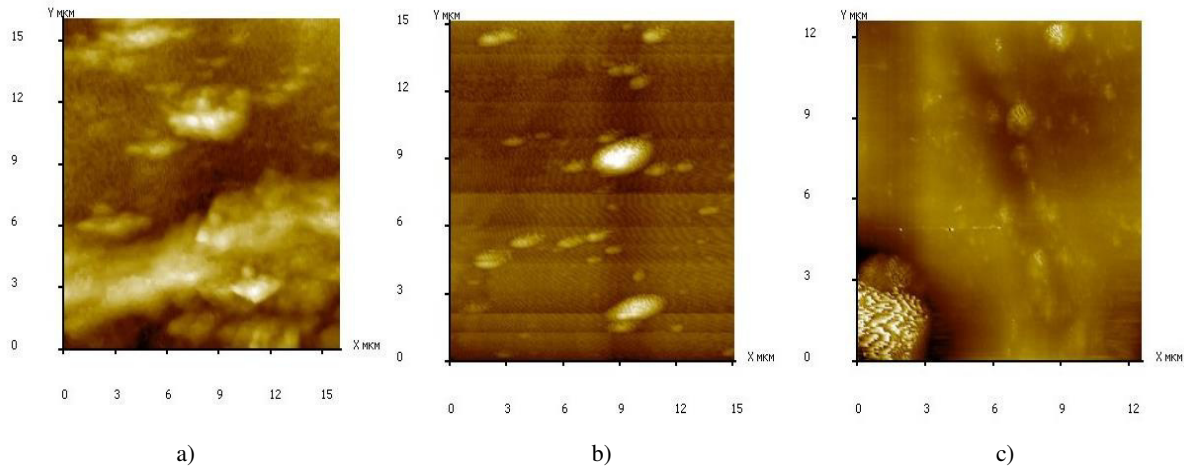


Fig.5. AFM 2D relief images of the $\text{Se}_{95}\text{As}_5$ (a), $\text{Se}_{95}\text{As}_5(\text{EuF}_3)_{0.01}$ (b), $\text{Se}_{95}\text{As}_5(\text{EuF}_3)_{0.1}$ (c)

Fig. 5 shows the AFM 2D relief images of $\text{Se}_{95}\text{As}_5$ and samples containing EuF_3 in various percentages. From fig. 5 that with an increase in the EuF_3 content, the relief of the sample changes markedly. This picture is a consequence of the fact that at low content of EuF_3 appears as ions Eu^{3+} , F^- and fills the existing voids. This eliminates the inhomogeneities associated with the density deficit, and also reduces the concentration of broken bonds, which leads to a decrease in the density of localized states in the mobility gap associated with charged defects (U^- centers). If we assume that the introduced EuF_3 appear as Eu^{3+} and F^- ions and in small quantities, mainly fill the existing voids, then they will help to eliminate the heterogeneity associated with the density deficit in these areas and at the same time due to chemical activity contribute to the formation of the EuSe_3 , SeF_6 type of structural element as a result of which the concentration of dangling bonds decreases, accompanied by a decrease in the density of localized states in the mobility gap associated with charged defects (U^- -centers) and about weakening of electrostatic potential fluctuations.

4. CONCLUSION

The structure of the $\text{Se}_{95}\text{As}_5(\text{EuF}_3)_x$ ($x = 0; 0.5; 1$ at%) CGS systems have been studied by X - ray diffraction, Raman scattering and atomic force microscopy. Interpretation of the results obtained have been carried out within the framework of the Elliott void-cluster model and the model of charged defects, the parameters of the local structure, in particular, the “quasi-period” density fluctuations, the correlation length (sizes of MRO regions), and diameters of nanovoids have been determined. A comparative analysis of the Raman spectra of the investigated films by literature data on Raman scattering of such materials the base structure elements and chemical bonds forming the amorphous matrix of $\text{Se}_{95}\text{As}_5$ CGS have been determined. Changes in the spectrum of $\text{Se}_{95}\text{As}_5$ doped by EuF_3 impurity were attributed to the destruction of some bonds and structural elements, and by the formation the new bonds with participation of europium atoms.

- [1] A. Zakery and S. Elliott. J. Non-Cryst. Solids 330, 1, 2003.
- [2] J. Sanghera and I. Aggarwal. J. Non-Cryst. Solids 256–257, 6, 1999.
- [3] I. Aggarwal and J. Sanghera. J. Optoelectron. Adv. Mater. 4, 665, 2002.
- [4] N.F. Mott, E.A. Davis. Electronic Processes in Non-crystalline Materials, Clarendon- Press, Oxford, 1971.
- [5] R.I. Alekberov, A.I. Isayev, S.I. Mekhtiyeva, G.A. Isayeva. Azerbaijan Journal of Physics 19, 3-7, 2013.
- [6] R.I. Alekberov, S.I. Mekhtiyeva, A.I. Isayev, M. Fábán. Journal of Non-Crystalline Solids Volume 470, Pages 152-159, 2017.
- [7] R.I. Alekberov, A.I. Isayev, S.I. Mekhtiyeva, G.A. Isayeva. Chalcogenide Letters, Vol. 10, p.335–339, 2013.
- [8] J.P. Neufville, S.C. Moss, S.R. Ovshinsky. J. Non-Cryst. Sol., v.13, p.191, 1973.
- [9] L.E. Busse, S.R. Nagel. Phys. Rev. Lett., 47, 1848, 1981.
- [10] L.E. Busse. Phys. Rev., B. 29, 3639, 1981.
- [11] K. Tanaka. Philos. Mag. Lett., 57, 183, 1988.
- [12] H. Tsutsu, K. Tamura, H. Eudo. Solid State Communic. V. 13, p. 191, 1984.
- [13] S.R. Elliott. Phys. Rev. Lett., 67, 711, 1991.
- [14] S.R. Elliott. J. Non-Cryst. Sol., 182, 40, 1995.
- [15] T.S. Kavetskyy, O.I. Shpotyuk, V.T. Boyko. J. Phys. Chem. Solids, 68, 712, 2007.
- [16] T.S. Kavetskyy, O.I. Shpotyuk. J. Optoelectron. Adv. Mater., 7, 2267, 2007.
- [17] O.I. Shpotyuk, A. Kozdras, T.S. Kavetskyy, J. Filipecki. J. NonCryst. Sol., 352, 700, 2006.

- [18] *A. I. Isayev, S. I. Mekhtiyeva, S. N. Garibova, and V. Z. Zeynalov. FTP v.45, 8, pp. 1026-1030, 2011 (in Russian).*
- [19] *S.R. Elliott. Phys. Rev. Lett., 67, 711, 1991.*
- [20] *S.R. Elliott. J. Non-Cryst. Sol., 182, 40, 1995.*
- [21] *P.H. Gaskell. J. Non-Cryst. Sol., 351, 1003, 2005.*
- [22] *O.P. Rachev. J. Non-Cryst. Sol., 352, 3781, 2006.*
- [23] *A. I. Isayev, S. I. Mekhtiyeva, S. N. Garibova, and V. Z. Zeynalov. FTP v.45, 8, pp. 1026-1030, 2011 (in Russian).*
- [24] *S.R. Elliott. J.Phys. Cond. Matt., v.38, p. 7661, 1992.*
- [25] *V. Kovanda, Mir Vicek, H. Jain. J. Non-Cryst. Sol., 326–327, 88, 2003.*
- [26] *V.I. Mikla. J. Phys.: Condens. Matter, 9, 9209, 1997.*
- [27] *W. Bues, M. Somer, and W. Brockner, Z. Naturforsch. C 35, 1063, 1980.*
- [28] *C. Zha, R. Wang, A. Smith et al. J Mater Sci: Mater Electron. p. 389, 2007.*

Received: 25.02.2019

INFLUENCE OF FULLERENES ON DIELECTRIC AND CONDUCTIVITY PROPERTIES OF SMECTIC A LIQUID CRYSTAL WITH NEGATIVE DIELECTRIC ANISOTROPY

T.D. IBRAGIMOV, A.R. IMAMALIYEV, G.F. GANIZADE

G.M. Abdullayev Institute of Physics of Azerbaijan NAS

131, H. Javid ave., Baku, AZ 1143

tdibragimov@mail.ru

Influence of fullerenes on dielectric and conductivity properties of smectic A liquid crystal is investigated. It is shown that the transverse component of the real part of dielectric permittivity increases at the additive of fullerenes while the longitudinal component decreases. At this case, a maximum of dielectric absorption shifts to the high-frequency region. Conductivity increases at low frequencies and decreases at the high ones. Experimental results are explained on the base of the Maier - Meier theory for anisotropic liquids and also participation of fullerenes in ionic conductivity of liquid crystal.

Keywords: Liquid crystal, smectic A, fullerenes, dielectric permittivity

PACS: 64.70.mj;64.70.pv;77.84.Nh;82.70.Dd.

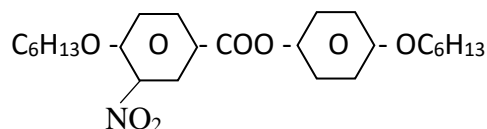
1. INTRODUCTION

Development of nanotechnology has incentivized to the idea to combine the properties of small particles with peculiarities of optic effects in liquid crystals (LC). The small particles embedded into liquid crystals can not only change properties of the matrix but also promote the origin of new optical effects. In particular, injection of conducting and non-conducting submicron particles strongly influences on electrohydrodynamic instability of liquid crystal with negative dielectric anisotropy [1]. Electro-optic parameters of the Clark-Lagerwall effect in the ferroelectric liquid crystal improve at additive of ferroelectric particles [2]. Ferroelectric particles embedded into nematic LCs form local electric fields at application of electric field to their layer which strongly change the dielectric and electro-optic parameters [3-6].

Addition of nanoparticles into LC can lead to more essential changes as they are distributed between LC molecules at low concentration. Fullerenes have the spherical form and the concrete sizes about 1 nm. Currently, there is a small number of works devoted to liquid crystalline colloids based on fullerenes. Particularly, influence of bias voltage on the liquid crystalline colloid based on pure fullerenes is investigated in work [7]. Results of influence of laser radiation on electro-optic properties of similar colloids are presented in the works [8]. Changes of dielectric parameters of nematic LC study in works [9 - 10]. The aim of present work is the study of action of fullerenes on dielectric and conductivity properties of the smectic A liquid crystal.

2. EXPERIMENTAL

We used smectic A liquid crystal 4-hexyloxyphenyl ether 4'-hexyloxy 3'-nitrobenzoic acid (C2) as a matrix which has structural formula



A presence of nitrophenyl dipole group – C- NO₂ of this LC is the reason of the large negative dielectric anisotropy. The fullerenes C₆₀ (U.S. Research Nanomaterials, Inc.) were added into the liquid crystal with 0.5 wt. % and were shaken in a vortex mixer for 1 hour at temperature 75°C, followed by sonication with dispergator Ultrasonic Cleaner NATO CD - 4800 (China) for 4 hours.

The cell had a sandwich structure and consisted of two plane-parallel glass plates whose inner surfaces were coated with thin transparent and conductive indium-tin-oxide (ITO) layer. Planar orientation of molecules was attained by coating the inner substrate surfaces with rubbed polyimide layers. The cell thickness was fixed with calibrated 20 μm polymer spacers for measurements. Homeotropic orientation of molecules has been reached by mechanical shift of one substrate concerning another at frequency of 50 Hz for several minutes in the filled cell. Both the colloid and the pure LC were injected into the empty cell by capillary action at the isotropic state. The stuffed cell was kept in the special heater with temperature regulator GL-100 (China). The copper-constantan thermocouple was used for temperature control. An accuracy of temperature determination was 0.1°C.

Dielectric and conductivity measurements were carried out by the Precision LCR Meter 1920 (IET Labs. Inc., USA) in the frequency range of 20 Hz –1 MHz and at temperatures between 30°C –60°C. In this case, applied voltage was 1 V for both LC molecular orientations.

A set-up for measurements of electro-optical parameters was assembled on the base of the Carl Zeiss polarization microscope. The electric impulses of the special form applied to the cell from the functional generator (model G6-28, Russia). A light,

passing through the cell, fell on the photo diode and was registered by digital storage oscilloscope (model 6022BE, Hantek). The threshold voltage was defined using unipolar triangular impulses in quasi -static regime. Besides, a value of the threshold voltage was supervised under the polarization microscope. Frequency dependence of the threshold voltage was registered by application of sinusoidal voltage. The measurements were carried out at temperature 32°C.

3. RESULTS AND DISCUSSION

According to [10], particles do not disturb the director field of a LC if the anchoring parameter $\zeta=WR/K$ is much smaller than 1, where W is the anchoring energy of LC molecules with particle surfaces; $2R$ is particle size; K is the LC elastic constant. The values of anchoring energy are within $10^{-4} - 10^{-6} \text{ J/m}^2$, the elastic constant of LC has an order of 10^{-12} N , and the fullerenes have sizes of 1 nm. Elementary calculations show that the anchoring parameter has an order between $10^{-1} - 10^{-3}$. It is much less than 1. Thus, the overall disturbance of the director field by fullerenes do not appears still less at similar concentration. Hence, the obtained colloids can be considered as a homogeneous media and they should behave as pure LCs but with the modified parameters. Besides, we may estimate de Broglie wavelength λ of fullerenes as follows:

$$\lambda = \frac{h}{m_0 v}$$

where h is Planck constant, m_0 is mass of fullerene ($1.2 \cdot 10^{-24} \text{ kg}$), v is the average velocity determined by the following expression:

$$v = \sqrt{\frac{3k_B T}{m_0}}$$

where k_B is Boltzmann constant, T is Kelvin temperature. Simple validation shows that λ is equal about $3 \cdot 10^{-11} \text{ m}$. The sizes of fullerenes (about 1 nm) are more than de Broglie wavelength. Thus, the condition for display of quantum-size effect is not realized and fullerenes behave as classical particles.

Observation under polarization microscope has shown that the clearing temperature decreases from 70.9°C to 69.2°C. Spherical particles of fullerenes infiltrate between LC molecules reducing interaction in between. At this case, there is disordering of LC directions and, accordingly, reduction of order parameter S . As a result, temperature of transition from isotropic to smectic phase decreases according to expression [11]:

$$T_c = (1-f_o) T_p$$

where f_o is volume concentration of particles, T_p and T_c are clearing temperatures of pure LC and the colloid, correspondingly.

The frequency dependences of real ϵ' and imaginary ϵ'' parts of dielectric permittivity of both the

pure LC and the corresponding colloid at planar configuration and temperature 32°C are presented in fig. 1. Apparently, ϵ' slightly decreases from 14,0 at 40 Hz to 13,81 at 20 kHz then it drastically decreases. The value of ϵ' for the colloid is more than for the pure LC at all frequencies. At this case, it changes from 14,4 at 40 Hz to 14,23 at 30 kHz then its value also drastically decreases. A presence of fullerenes decreases the value ϵ'' . At this case, a maximum of dielectric absorption shifts to the high-frequency region.

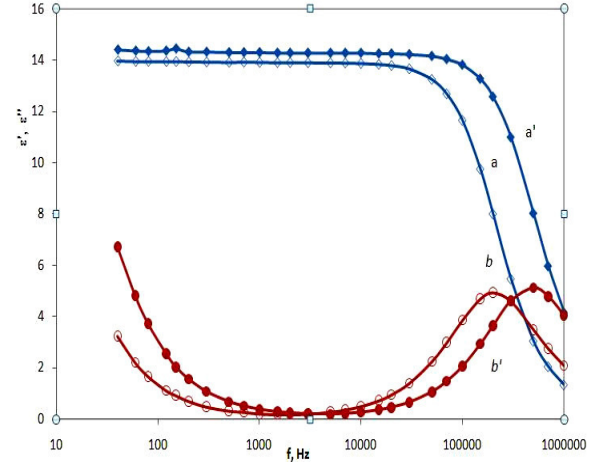


Fig.1. Frequency dependence of real ϵ' and imaginary ϵ'' components of dielectric permittivity at planar configuration (temperature 32°C): (a) ϵ' of the pure LC, (a') ϵ' of the colloid, (b) ϵ'' of the pure LC, (b') ϵ'' of the colloid.

It is known that the relaxation time of LC molecules which is characterized by flipping of molecules from one to an opposite direction and defined as follows:

$$\tau = \frac{1}{2\pi f}$$

where f is the frequency of applied electric field. The additive of fullerenes decreases the relaxation time from $8.0 \cdot 10^{-7} \text{ s}$ to $3.2 \cdot 10^{-7} \text{ s}$ at 32°C. Temperature also has an effect on the position of dielectric absorption maximum and, correspondingly, the relaxation time: an increase of temperature reduces viscosity. As a result, the molecule flipping becomes easier (fig. 2).

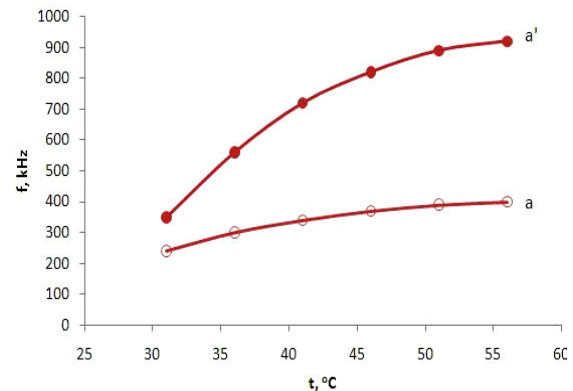


Fig.2. Temperature dependence of a maximum of dielectric absorption: (a) the pure LC, (a') the colloid.

Frequency dependences of real and imaginary components of dielectric permeability of the pure LC and the colloid at homeotropic configuration and temperature 320C are presented in fig. 3. As one can see, ε' of the pure LC equals to 4.25 at 40 Hz then there is dispersion near 500 Hz and its value remains almost invariable and equals 3.91 up to 100 kHz, finally, it sharply decreases. A presence of particles slightly reduces the value ε' to 4.17 at 40 Hz and 3.85 at 100 kHz. Here the dispersion and a maximum of dielectric absorption also observes near 500 Hz.

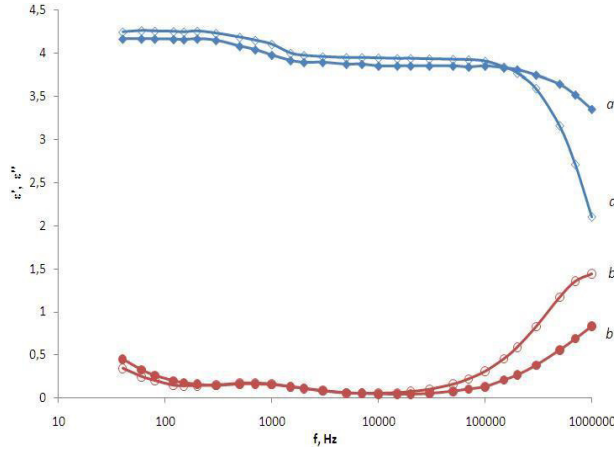


Fig.3. Frequency dependence of real ε' and imaginary ε'' components of dielectric permittivity at homeotropic configuration (temperature 320C): (a) ε' of the pure LC, (a') ε' of the colloid, (b) ε'' of the pure LC, (b') ε'' of the colloid.

Obviously, this dispersion connects with the dipole fragment – C-NO₂, which non exactly perpendicular to the long molecular axis but has the parallel component along this axis. It should be pointed out the dielectric anisotropy of the pure LC equals to 9.90 at the middle frequencies while this value makes 10.38 for the colloid. In other words, the additive of particles slightly enhances dielectric anisotropy.

The observable experimental facts can be explained by the theory Mayer-Meyer for anisotropic liquids according to which expressions for both components of dielectric permittivity are defined as follows [12]:

$$\varepsilon'_{||} = 1 + \frac{NHF}{\varepsilon_0} \left\{ \gamma_{av} + \frac{2}{3} S \Delta \gamma + F \frac{p_e^2}{3k_B T} \left[1 - \frac{1}{2} (1 - 3 \cos^2 \beta) S \right] \right\}$$

$$\varepsilon'_{\perp} = 1 + \frac{NHF}{\varepsilon_0} \left\{ \gamma_{av} - \frac{1}{3} S \Delta \gamma + F \frac{p_e^2}{3k_B T} \left[1 + (1 - 3 \cos^2 \beta) S \right] \right\}$$

here $\gamma_{av} = (\gamma_{||} + 2 \gamma_{\perp})/3$ is the average magnitude of polarizability of LC molecules; $\Delta \gamma = \gamma_{||} - \gamma_{\perp}$ is anisotropy of polarizability; N is concentration of LC molecules; S is the order parameter; β is the angle between a dot molecular dipole p_e and an axis of the

maximal polarizability; H is the dimensionless value characterizing the form of the Lorentz cavity; F is the reaction field which changes resultant field in the Lorentz cavity; ε_0 is permittivity of vacuum; k_B is the Boltzmann constant; T is absolute temperature.

Longitudinal component of dielectric permittivity increases while transverse component decreases. These expressions include the order parameter S and quantity of molecules N per volume unit. As concentration of the colloid is very small so the number of the particles per volume unit is also small, namely, with ratio of 0.0029. In other words, N decreases negligible. A different matter the order parameter which is defined as follows [12]:

$$S = \frac{1}{2} (3 \cos \theta - 1) \quad (6)$$

The embedded particles increase an instant angle θ between individual molecules and the preferred direction of molecules (director). In this connection, the order parameter considerably decreases. The last member of the expression for longitudinal and transverse components of dielectric permittivity containing the order parameter has the larger value for transverse component than for the longitudinal one. In this connection, the transverse component increases and the longitudinal component decreases at presence of fullerenes.

Frequency dependences of specific conductance of the pure LC and the colloid are resulted in fig. 4. Apparently, the dispersion connected with the dipole fragment – C-NO₂ also is observed on the curves. Here, specific conductance slightly increases before and decreases after this dispersion, correspondingly, at the additive of fullerenes. In particular, the longitudinal component increases from $1.72 \cdot 10^{-5}$ S/m to $1.73 \cdot 10^{-5}$ S/m and the transverse component from $9.92 \cdot 10^{-7}$ S/m to $1.23 \cdot 10^{-6}$ S/m. Put in other words, there is a relation $\sigma_{||} / \sigma_{\perp}$ is equal to 17.3 for the pure LC while it becomes 14.1 at the additive of fullerenes. The longitudinal component decreases from $1.90 \cdot 10^{-1}$ S/m to $8.36 \cdot 10^{-2}$ S/m and the transverse component also decreases from $1.42 \cdot 10^{-2}$ S/m to $6.40 \cdot 10^{-3}$ S/m on the frequency of 300 kHz at the additive of fullerenes. There is a relation $\sigma_{||} / \sigma_{\perp}$ equals to 13.4 for the pure LC and becomes 13.0 at the additive of fullerenes. It is obvious, that similar change of specific conductance is connected by that the fullerenes participate in movement of ions at low frequencies and they are not able to move in time behind them at high frequencies because of time lag.

Ohmic conductivity on alternating current may be presented as:

$$\sigma = 2\pi f \varepsilon_0 \varepsilon''$$

Apparently, the conductivity components ε' strongly increases within the dispersion region. Liquid crystals possess the dielectric anisotropy and, consequently, the relation $\sigma_{||} / \sigma_{\perp} = \varepsilon''_{||} f_{||} / \varepsilon''_{\perp} f_{\perp}$ strongly depends on frequency. In connection with a difference

of frequency ranges of a dispersion $\varepsilon'_{||}$ and ε'_{\perp} , maxima $\varepsilon''_{||}$ and ε''_{\perp} are observed at various frequencies and, accordingly, $\sigma_{||}$ and σ_{\perp} start to increase at the same frequencies. The additive of fullerenes shifts dispersion of the real part of dielectric permittivity to the high frequency region. Therefore, the same shift occurs with dispersion of specific conductance.

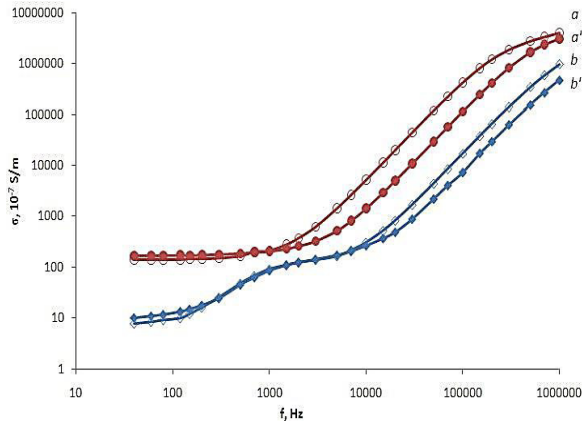


Fig.4. Frequency dependence of specific conductance components at temperature 32°C: (a) $\sigma_{||}$ of the pure LC, (a') $\sigma_{||}$ of the colloid, (b) σ_{\perp} of the pure LC, (b') σ_{\perp} of the colloid.

Additionally, the threshold voltage of homeotropic-planar transition decreases from 250V to

185 V at the additive of fullerenes. Threshold voltage of homeotropic - planar transition is defined as follows [13]:

$$U = \sqrt{\frac{Wd}{2\varepsilon_0|\Delta\varepsilon|\cdot l}}$$

ℓ is length of molecule, W is sum of elastic energy and the energy connected with formation of declinations and dispositions; $\Delta\varepsilon$ is anisotropy of dielectric permittivity, d is the layer thickness. Essential reduction of threshold voltage cannot be connected with an insignificant increase in dielectric anisotropy. Apparently, it is caused by occurrence of defects-germs with which the growth of planar areas begins. Thus, the magnitude of W decreases, that is reflected in value of the threshold voltage.

4. CONCLUSION

It is shown that the additive of fullerenes leads to an increase of the transverse component of real part of dielectric permittivity while the longitudinal component reduces. At this case, there is a shift of a maximum of dielectric absorption to the high-frequency region. Electric conductivity increases at low frequencies and decreases at the high frequencies. Threshold voltage of homeotropic-planar transition decreases from 250 V to 185 V.

- [1] T.D. Ibragimov, G.M. Bayramov. Influence of small particles on Carr-Helfrich electrohydrodynamic instability in the liquid crystal. Intern. Journal for Light and Electron Optics, 2013, v. 124, pp. 3004-3006.
- [2] T.D.Ibragimov, G.M.Bayramov, A.R.Imamaliyev Clark -Lagerwall effect in the small particles-ferroelectric liquid crystal system. International Journal for Light and Electron Optics, 2013, v. 124, pp. 343-346.
- [3] T.D.Ibragimov, A.R.Imamaliyev, G.M.Bayramov Influence of barium titanate particles on electro-optic characteristics of liquid crystalline mixture H37. Intern. Journal for Light and Electron Optics, 2016, v. 127, pp. 1217-1220.
- [4] T.D.Ibragimov, A.R.Imamaliyev, G.M.Bayramov Electro-optic properties of the BaTiO₃-Liquid crystal 5CB colloid. International Journal for Light and Electron Optics, 2016, v.127, pp.2278-2281.
- [5] T.D.Ibragimov, A.R.Imamaliyev, G.M.Bayramov Formation of local electric fields in the ferroelectric BaTiO₃ particles-liquid crystal colloids. Ferroelectrics, 2016, v. 495, No 1, pp.60-68.
- [6] T.D. Ibragimov, A.R. Imamaliyev, G.M. Bayramov. Peculiarities of electro-optic properties of the ferroelectric particles-liquid crystal colloids. AIP Conference Proceedings, 2016, v. 1727, pp.020011-1-8.
- [7] S.E.San, M.Okutan, O.K.Äoysal, Y.Yerli. Carbon Nanoparticles in Nematic Liquid Crystals. Chin. Phys. Lett., 2008, v. 25, pp. 212-215.
- [8] S.E. San, O. Köysal, M. Okutan. Laser-induced dielectric anisotropy of a hybrid liquid crystal composite made up of methyl red and fullerene C60. Journal of Non-Crystalline Solids, 2005, v.351, No 33-36, pp. 2798-2801.
- [9] M.Okutan, S.E.San, E.Basaran, F.Yakuphanoglu. Determination of phase transition from nematic to isotropic state in carbon nano-balls' doped nematic liquid crystals by electrical conductivity -dielectric measurements. Physics Lett. A, 2005, v. 339, No6, pp. 461 - 465.
- [10] Liquid Crystals beyond Displays. Chemistry, Physics, and Applications. Edited by Li Q. New Jersey, Hoboken: John Wiley and Sons, Inc. 2012, 573.
- [11] F.Haragushi, K.Inoue, N.Toshima et al. Reduction of the threshold voltages of nematic liquid crystal electrooptical devices by doping inorganic nanoparticles. Japanese Journal Applied Physics, 2007, v. 46, pp. L796-L797
- [12] L.Blinov. Structure and properties of liquid crystal. New York: Springer, 2011, 439.
- [13] L.M. Blinov, V.G. Chiginov - Electrooptic effects in liquid crystal materials. 1994, Springer Verlag, p.488.

Received: 26.02.2019

MAGNETIC MOMENT OF ELECTRONS IN DILUTED MAGNETIC SEMICONDUCTOR QUANTUM RING

A.M. BABANLI^{1,2}, B.G. IBRAGIMOV^{2,3}

¹Department of Physics, University of Süleyman Demirel, 32260 Isparta, Turkey,

²G.M. Abdullayev Institute of Physics of Azerbaijan NAS, 131, H. Javid ave., Baku, AZ 1143,

³Baku State University, Baku, Azerbaijan

arifbabanli@sdu.edu.tr, behbud.ibrahimov.93@mail.ru

In the present paper, we have investigated the magnetization of electrons in a diluted magnetic semiconductor (DMS) quantum ring. We take into account the effect of Rashba spin-orbit interaction, the exchange interaction and the Zeeman term on the magnetization. We have calculated the energy spectrum and wave function of the electrons in diluted magnetic semiconductor quantum ring. Moreover, we have calculated the magnetic moment as a function of the magnetic field for strong degenerate electron gas at finite temperature of a diluted magnetic semiconductor quantum ring.

Keywords: Rashba effect, magnetic moment, heat capacity, diluted magnetic semiconductor.

PACS: 35Q41

1. INTRODUCTION

In the last decade enormous attention has been devoted toward control and engineering of spin degree of freedom at mesoscopic scale, usually referred to as spintronics [3]. Important class of materials for spintronics forms diluted magnetic semiconductors (DMS). In a previous paper [1] we calculated the heat capacity and magnetization of a DMS quantum ring for Boltzmann statistics. The aim of this paper is to generalize the theory of free-electron Landau diamagnetism so as to include parabolic of the Fock-Darwin type confinement. In this way we move from classical statistics to the degenerate Fermi limit.

2. THEORY

We take into account the effects of the Zeeman and exchange terms on the magnetic moment of DMS

quantum ring, the electron is assumed to be moving in a parabolic potential of the Fock -Darwin type given by [1]:

$$V_c(\rho) = \frac{V_0 \rho^2}{2R^2}, \quad \rho \leq R, \quad (1)$$

where V_0 - defines the depth of this potential and ρ - is the distance of electron from the centre of the DMS quantum ring. The quantum ring is subjected to a uniform magnetic field $\vec{H} = (0, 0, H)$ normal to the quantum ring plane. We assume that the spin-orbit interaction is described by the Rashba Hamiltonians [1]. The total Hamiltonian of the system is given by:

$$H = \frac{1}{2m_n} \left(\vec{P} + e\vec{A} \right)^2 + V_c(\rho) + \frac{1}{2} g \sigma_z \mu_B H + \sigma_z \alpha_0 \frac{dV(\rho)}{d\rho} \left(-i \frac{1}{\rho} \frac{\partial}{\partial \varphi} + \frac{eH\rho}{2\hbar} \right) + H_{ex}, \quad (2)$$

where m_n - is the electron mass, σ_z - is the Pauli z matrix, α_0 is the Rashba spin-orbit coupling parameter, g represents the Lande factor. In the mean field approximation, the exchange Hamiltonian term can be written as:

$$H_{ex} = \frac{1}{2} \langle S_z \rangle N_0 x J_{sd} \sigma_z = 3A \sigma_z \quad (3)$$

where J_{sd} is a constant which describes the exchange interaction; N_0 is the density of the unit cell. For uniform magnetic field, H directed along z-axis, the vector potentials in cylindrical polar coordinates have

the components $A_\phi = \frac{H\rho}{2}$, $A_\rho = 0$ and the solution

of Schrödinger equation has been known [1]. The electron energy levels given by [1, 2]:

$$E_{nl\sigma} = \hbar \Omega_\sigma \left(n + \frac{1}{2} + \frac{|l|}{2} \right) + \frac{l \hbar \omega_c}{2} + \frac{1}{2} g \sigma_z \mu_B H + 3A \sigma + \sigma \frac{\alpha \cdot l}{R} \quad (4)$$

where $\sigma = \pm 1$ and we have used notations:

$$\Omega_\sigma = \sqrt{4\omega_0^2 + \omega_c^2 + \sigma \frac{\alpha \cdot \omega_c}{R \cdot \eta}}, \quad \omega_0 = \sqrt{\frac{V_0}{m_n R^2}}, \quad \omega_c = \frac{eH}{m_n} \quad (5)$$

The partition function for the Boltzmann statistics is given by:

$$Z = \sum_\sigma \frac{1}{2} \frac{e^{-\frac{\sigma d}{k_B T}}}{\cosh\left(\frac{\hbar \Omega_\sigma}{2k_B T}\right) - \cosh\left(\frac{b_\sigma}{2k_B T}\right)}; \quad b_\sigma = \hbar \omega_c \left(1 + \sigma \frac{2\alpha}{\hbar \omega_c R}\right), \quad d = \frac{1}{2} g \mu_B H + 3A, \quad (6)$$

where $E_{nl\sigma}$ is the energy spectrum of considered system, k_B is the Boltzmann constant. To calculate thermodynamic potential Ω we use an approach based on calculating the classical partition function z of the electron gas:

$$\Omega = -k_B T \frac{1}{2\pi i} \int_{\nu-i\infty}^{\nu+i\infty} \frac{\pi \xi}{\sin(\pi \xi)} \cdot \frac{e^{\frac{\mu}{k_B T} \xi}}{\xi^2} z\left(\frac{k_B T}{\xi}\right) d\xi \quad (7)$$

where μ is the chemical potential of the gas. If we change to the dimensionless variable of integration

$$z = \frac{b_\sigma}{2k_B T} \xi, \quad \text{Eq.(7) takes the form}$$

$$\Omega_\sigma = -\frac{b_\sigma}{4} \frac{1}{2\pi i} \int_{\nu-i\infty}^{\nu+i\infty} \frac{\pi \frac{2k_B T}{b_\sigma} z}{\sin\left(\pi \frac{2k_B T}{b_\sigma} z\right)} \cdot \frac{e^{\frac{2\mu}{b_\sigma} z}}{z^2} \frac{e^{-\frac{2\mu}{b_\sigma} z}}{\cosh(B_\sigma z) - \cosh(z)} dz, \quad (8)$$

where $B_\sigma = \frac{\eta \Omega_\sigma}{b_\sigma}$. The finite temperature effects are represented by an expansion the functions

$$\frac{\pi \frac{2k_B T}{b_\sigma} z}{\sin\left(\pi \frac{2k_B T}{b_\sigma} z\right)} \quad \text{in powers of the small quantity} \quad \pi \frac{2k_B T}{b_\sigma} z. \quad (9)$$

$$\frac{\pi \frac{2k_B T}{b_\sigma} z}{\sin\left(\pi \frac{2k_B T}{b_\sigma} z\right)} \approx 1 + \frac{2\pi^2 k_B^2 T^2}{3b_\sigma^2} + \dots$$

For the low fields $\frac{\mu}{\eta \omega_c} \gg 1$, only the small z behaviour of the non-exponential portion of the integrand in (8) contributes significantly:

$$\frac{1}{\cosh(B_\sigma z) - \cosh(z)} \approx \frac{1}{z^2} \frac{2}{B_\sigma^2 - 1} + \frac{1}{6} \frac{1 + B_\sigma^2}{1 - B_\sigma^2} + \dots \quad (10)$$

Inserting (9) and (10) into (8) and using the formula

$$\frac{1}{2\pi i} \int_{v-i\infty}^{v+i\infty} \frac{dz}{z^\delta} e^{tz} = \frac{t^{\delta-1}}{\Gamma(\delta)}, \quad (11)$$

When δ positive, we find

$$\Omega = -\frac{1}{4} \sum_{\sigma=\pm 1} b_\sigma \left(\frac{1}{2} \frac{D_\sigma^3}{B_\sigma^2 - 1} + \frac{D_\sigma^2}{6} \frac{1 + B_\sigma^2}{1 - B_\sigma^2} + \frac{4k_B^2 T^2}{3b_\sigma^2 (B_\sigma^2 - 1)} D_\sigma \right), \quad (12)$$

where $D_\sigma = \frac{2\mu - \sigma d}{b_\sigma}$. In the absence of spin degree of freedom the thermodynamic potential

$$\Omega = -\frac{1}{6} \frac{\mu^3}{\eta^2 \omega_0^2} + \frac{\mu}{6} \left(1 + \frac{\omega_c^2}{2\omega_0^2} - \frac{2k_B^2 T^2}{\eta^2 \omega_0^2} \right) \quad (13)$$

The magnetic moment of electrons in the quantum ring at the chemical potential $\mu = \text{const}$ is

$$M = -\frac{1}{A} \left(\frac{\partial \Omega}{\partial H} \right)_\mu = -\frac{2}{3} \frac{H}{A} \frac{\mu \mu_B^2}{\eta^2 \omega_0^2} \left(\frac{m_0}{m_n} \right)^2, \quad (14)$$

where A is the area of quantum ring, m_0 is the free electron mass. We shall take as the area of the cross-section of the potential well where $\mu = \frac{m_n \omega_0^2 r^2}{2}$ and can be written $A = \frac{2\pi\mu}{m_n \omega_0^2}$.

$$\frac{M}{\mu_B} = -\frac{m_n}{3\pi} \frac{\mu_B H}{\eta^2} \left(\frac{m_0}{m_n} \right)^2 \quad (15)$$

3. RESULTS AND DISCUSSION

Thus, the magnetization is independent of the confinement parameter ω_0 .

We next turn to de Haas–van Alphen oscillatory behaviour the magnetization in quantum ring with Rashba spin-orbit coupling. The integrand in (8) has simple poles and the points $\frac{2il\pi}{(B_\sigma \pm 1)}$, $l = \pm 1, \pm 2, \dots$ along the imaginary axis. Evaluating (8) by closing the integration by a large semicircle to the left, and summing the residues we have:

$$\Omega = k_B T \sum_{\sigma=\pm 1, l=1} \frac{(-1)^{l+1}}{2l} \left[\frac{\sin\left(\frac{\mu - \sigma d 4l\pi}{B_{\sigma+1} b_\sigma}\right)}{\sinh\left(\frac{4l\pi}{B_{\sigma+1}} \frac{\pi k_B T}{b_\sigma}\right) \sin\left(\frac{B_{\sigma-1}}{B_{\sigma+1}} l\pi\right)} + \frac{\sin\left(\frac{\mu - \sigma d 4l\pi}{B_{\sigma-1} b_\sigma}\right)}{\sinh\left(\frac{4l\pi}{B_{\sigma-1}} \frac{\pi k_B T}{b_\sigma}\right) \sin\left(\frac{B_{\sigma+1}}{B_{\sigma-1}} l\pi\right)} \right] \quad (16)$$

The structure of the resulting oscillations is quite complex since B_σ is strongly field dependent, and includes spikes where $\frac{B_\sigma - 1}{B_\sigma + 1}$ possesses integer values. At very high fields, so B_σ approaches 1 the amplitude the first term in (16) will grow without as expected. Differentiating only the rapidly oscillating factors in Eq. (16) we find the magnetization.

$$\frac{M}{\mu_B} = -\frac{k_B T m_0}{m_n} \sum_{\sigma=\pm 1, l=1} \frac{(-1)^{l+1}}{2l} \left[\frac{\cos\left(\frac{\mu - \sigma d 4l\pi}{B_{\sigma+1} b_\sigma}\right) \partial_{\hbar\omega_c} \left(\frac{\mu - \sigma d 4l\pi}{B_{\sigma+1} b_\sigma}\right)}{\sinh\left(\frac{4l\pi}{B_{\sigma+1} b_\sigma} \frac{\pi k_B T}{b_\sigma}\right) \sin\left(\frac{B_{\sigma+1} - 1}{B_{\sigma+1}} l\pi\right)} + \frac{\cos\left(\frac{\mu - \sigma d 4l\pi}{B_{\sigma-1} b_\sigma}\right) \partial_{\hbar\omega_c} \left(\frac{\mu - \sigma d 4l\pi}{B_{\sigma-1} b_\sigma}\right)}{\sinh\left(\frac{4l\pi}{B_{\sigma-1} b_\sigma} \frac{\pi k_B T}{b_\sigma}\right) \sin\left(\frac{B_{\sigma-1} + 1}{B_{\sigma-1}} l\pi\right)} \right] \quad (17)$$

-
- | | |
|--|--|
| <p>[1] A.M. Babanlı, B.G. Ibragimov, Specific heat in diluted magnetic semiconductor quantum ring, Superlattices and Microstructures, Vol. 111, 2017, pp. 574-578.</p> <p>[2] L.D. Landau, L.M. Lifshitz, Quantum Mechanics: Non-Relativistic Theory, Vol.3, 3rd edn., Amsterdam, Elsevier, 2001, 689 p.</p> | <p>[3] S.A. Wolf et al., Spintronics: a spin-based electronics vision for the future, <i>Science</i>, Vol. 294, 2001, 1488-1495.</p> |
|--|--|

Received: 05.03.2019

STRUCTURAL PECULIARITIES AND DIELECTRIC PROPERTIES OF HIGH-DENSITY POLYETHYLENE FILMS CONTAINING InP AND Ge PARTICLES

¹S.M. RZAYEVA, ¹Sh.Sh. RASHIDOVA, ²T.H. ISMAILOV

¹G.M. Abdullayev Institute of Physics of Azerbaijan NAS,

131, H. Javid ave., Baku, AZ 1143

²Baku State University, 23, Z. Khalilov, AZ1073, Baku, Azerbaijan;

rzayevasitare@gmail.com

High density polyethylene (HDPE) films of various thickness (100,200 μm) and content (2-10 vol.%) of InP/Ge particles were obtained by hot pressing a homogeneous mixture of fillers with a polymer matrix under a pressure of 10 MPa and at a temperature $T=413\text{K}$. HDPE films with dispersed InP and Ge particles were characterized by a combination of X-ray fluorescence microscopy (XRFM), X-ray diffractometry (XRD) and infrared Fourier transform spectroscopy (FT-IR) methods. It is shown that the obtained samples are HDPE-based composites with nanostructured InP and Ge-particles with a size of coherent scattering regions (CSR) of 44.1 and 55.7 nm, respectively. By scanning the surface of the films with a spot of a beam with a diameter of 10 μm , local concentrations of InP and Ge particles in the samples were determined. The dependence of the characteristic frequencies of FT-IR for HDPE at 719 and 730 cm^{-1} on the concentration of the filler was established. The temperature (in the range of 290–440K) and frequency (range 25– 10^6 Hz) dependences of the dielectric constant and the angle of the tangent of dielectric losses were measured. The dependence of the values of dielectric characteristics on the content of the filler in the composite is established.

Keywords: InP, Ge, HDPE, X-ray fluorescence microscopy, X-ray diffractometry, infrared Fourier spectroscopy, dielectric properties.

PACS: 77.80-e; 77.84-s

1. INTRODUCTION

Development of methods for synthesizing polymer composites containing nanostructured semiconductor particles, both simple (Si,Ge,etc.) and complex (A_3B_5 , A_2B_6 , etc.), determining their structure, optical, magnetic, dielectric, thermal properties is of fundamental and practical interest. These materials are used as LEDs, lasers, photovoltaic cells, gas sensors, etc. They have unique electrical, optical, magnetic properties, which, however, strongly depend on the composition and technology of these materials [1,2].

There is a huge amount of semiconductor compounds, and in practice we can always find semiconductors with well applicable properties. The most investigated binary semiconductors. As a rule, they are classified according to the crystal-chemical principle or according to the structure, the arrangement of the initial elements in the periodic system, the name of the anion-forming agent. For example, compounds like A_3B_5 , such as nitrides, phosphides, arsenide, antimonides, are compounds of elements of the V-group (N,P,Sb) with metals (Al,Ga,In,Tl) of group I and compounds A_2B such as chalcogenides, sulfides, selenides, tellurides-compounds of group VI elements (S,Se,Te) with metals (Zn,Cd,Hg). These compounds are isoelectronic analogs of diamond, silicon, germanium (the total number of valence electrons in these compounds is 8, the coordination number is 4) and have the same properties as these simple semiconductors [3,4].

This paper presents the results of studying the structural features and dielectric properties of thin HDPE films with different contents (2-10 vol. %) Of InP and Ge particles using X-ray fluorescence microscopy, X-ray diffractometry and IR spectroscopy,

and measuring the dielectric characteristics of these composite materials.

2. MATERIALS AND METHODS

Mechanical mixtures of InP/Ge powders and HDPE powders were hot pressed under a pressure of 10 MPa at $T = 413\text{K}$ for a period of 15 minutes and rapidly cooled to room temperature. Films with different content of InP/Ge particles and thicknesses of 100 and 200 microns were prepared by this method. XGT 7000 X-ray fluorescence microscope, Horiba and XRD D8 X-ray diffractometers, Bruker, Germany, XRD TD 3500, China were used to study the distribution of InP and Ge particles in polymer composites and the phase composition of the composites, respectively. The microscope used allows analyzing the elemental composition of solid samples by scanning the surface from 0.512x0.512 mm to 10 cm x 10 cm with a resolution of 100 μm and 10 μm . The performed x-ray microanalysis was used for the local concentration of InP and Ge particles in samples of the composite material, to investigate the influence of the preparation conditions on their distribution in the samples [5,6]. FT-IR infrared spectrometer Varian 3600 was used to monitor the effect of the filler on the structure of polymer films. FT-IR spectra were recorded at room temperature in the frequency range of 4000–400 cm^{-1} . Measurements of the dielectric constant ϵ and the tangent of the angle of dielectric loss $\text{tg}\delta$ were carried out in the temperature range of 290–520K with a linear temperature rise at a speed of 2.5 deg/min. The frequency dependence of the dielectric constant ϵ and dielectric loss tangent $\text{tg}\delta$ was carried out in the frequency range from 102 to 105 Hz, the amplitude of the measured voltage -1V. Measurements of ϵ and $\text{tg}\delta$

were carried out using an E8-7 bridge with an alternating current at a frequency of 1 kHz and an E7-20 meter. Samples for measuring the dependence of dielectric characteristics in an exemplary electric field were prepared in the form of disks with a diameter of 20 mm and a thickness of about 100 microns. Reliable electrical contact of stainless steel electrodes with a diameter of 20 mm was ensured by

using extruded electrodes of aluminum foil with a thickness of 9 μm [7, 8].

3. RESULTS AND DISCUSSION

XRFM data. Fig. 1 and Table 1 present the X-ray fluorescence spectrum and data for the InP-Ge/HDPE composite film, respectively.

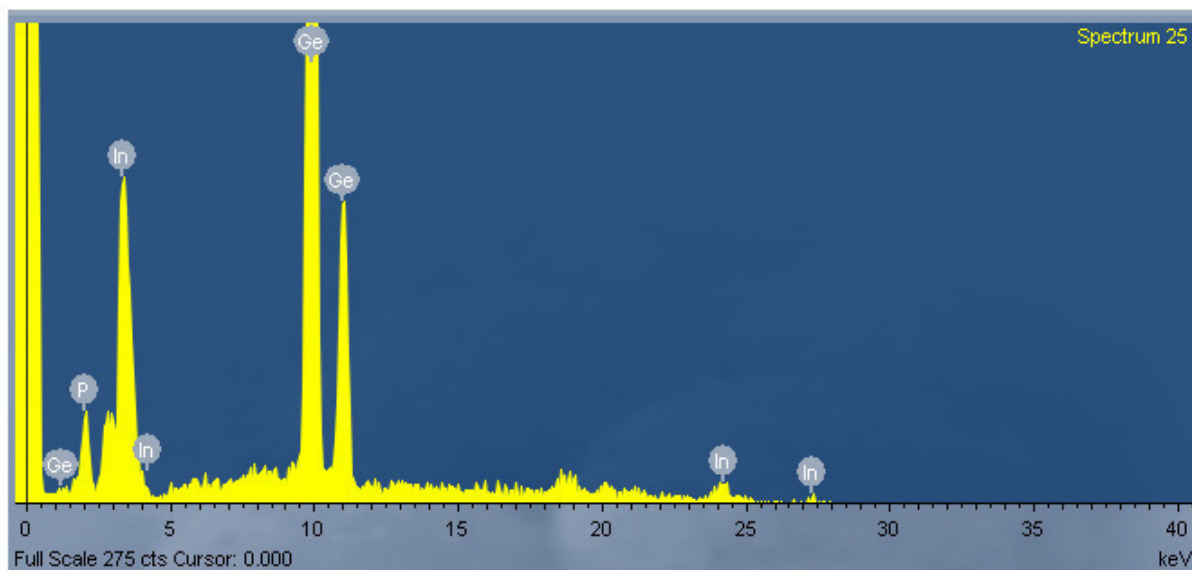


Fig. 1. X - ray fluorescence spectrum of the InP-Ge/HDPE composite film with a thickness of 100 microns.

Table 1.

The content of elements in the Ge-InP/HDPE film in five points randomly selected on the film surface according to X-ray fluorescence microscopy.

* Element	Line	Mas., [%]	3 - Sigma	* Element	Line	Mas., [%]	3 - Sigma
GeInP (1-5)				GeInP (3)			
¹⁵ P	K	4,51	0,79	¹⁵ P	K	5,13	0,81
³² Ge	K	49,45	1,87	³² Ge	K	52,52	2,47
⁴⁹ In	L	16,74	2,04	⁴⁹ In	L	19,03	2,68
GeInP (1)				GeInP (4)			
¹⁵ P	K	4,97	2,41	¹⁵ P	K	3,77	0,67
³² Ge	K	49,15	3,15	³² Ge	K	44,41	1,43
⁴⁹ In	L	18,43	3,03	⁴⁹ In	L	13,99	1,54
GeInP (2)				GeInP (5)			
¹⁵ P	K	4,67	1,62	¹⁵ P	K	4,43	3,72
³² Ge	K	51,85	2,56	³² Ge	K	54,31	4,37
⁴⁹ In	L	17,34	1,33	⁴⁹ In	L	16,44	2,98

* The results shown in the table refer to a sample whose surface is scanned with a spot of a beam with a diameter of 10 microns.

As can be seen from table 1, the values of local concentrations of InP and Ge particles in arbitrarily selected parts of a HDPE film are close and it can be stated that the particles are almost uniform in the HDPE film.

4. X - RAY PHASE ANALYSIS

In fig. 2, a, b shows radiographs of an InP/Ge mixture with a molar ratio of ~1:1 and a composite with a composition of 9% (InP+Ge)/91% HDPE, which is a

composite based on polyethylene HDPE, containing a total of 9% by volume of particles InP and Ge, respectively.

As can be seen from the diffractogram (fig. 2, b), the composite under study consists of well-crystallized HDPE with a very small amount of amorphous phase. Characteristic of HDPE according to JCPDS 00-040-1995 appear at 21.56°, 23.87°, 30.18° and 36.29°, which corresponds to the (110), (200), (210) and (020), respectively [7, 8]. Peaks of fillers embedded in HDPE

(fig. 2, b) refer to Ge and InP with a cubic structure. The average size of coherent scattering regions (44.1 and 55.74 nm) of indium and germanium phosphide particles was estimated.

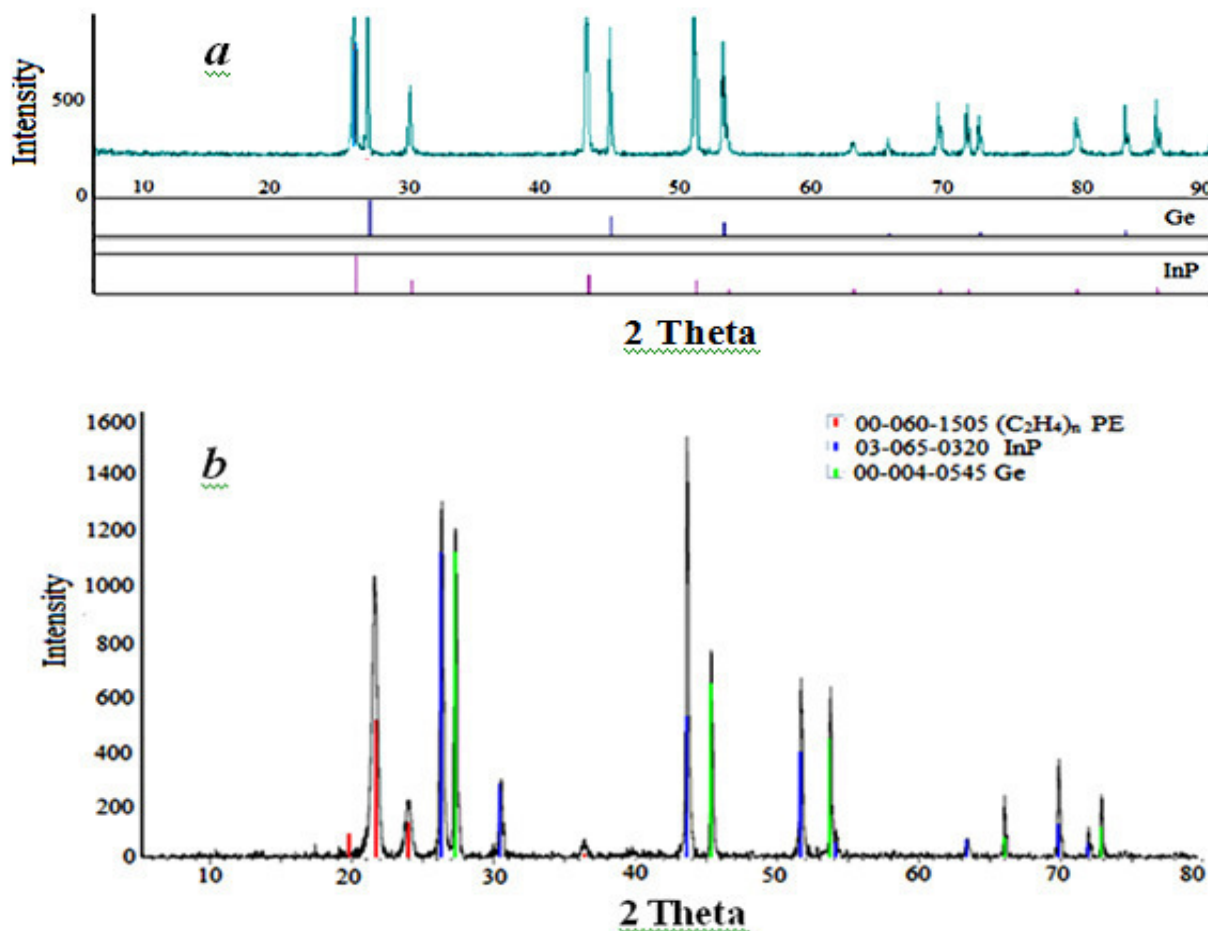


Fig. 2. XRD patterns of the: a) InP / Ge mixture with mol to mol ratio ~1:1 and b) 9% (InP+Ge)/91% HDPE mixture.

As can be seen from the diffractogram (fig. 2, b), the composite under study consists of well-crystallized HDPE with a very small amount of amorphous phase. Characteristic of HDPE according to JCPDS 00-040-1995 appear at 21.56 °, 23.87 °, 30.18 ° and 36.29 °, which corresponds to the (110), (200), (210) and (020), respectively [7, 8]. Peaks of fillers embedded in HDPE

(fig. 2, b) refer to Ge and InP with a cubic structure. The average size of coherent scattering regions (44.1 and 55.74 nm) of indium and germanium phosphide particles was estimated.

Table 2 shows the XRD parameters and crystallite size values determined on the basis of the values of these parameters.

Table 2.

XRD parameters and crystallite size values for InP, Ge and HDPE*.

	InP	Ge	HDPE
* FWHM, rad.	0,184	0,146	0,48
Lattice parameters, nm	Cubic: F-43m (216) a: 0.58687	Cubic: Fd-3m (227) a: 0.56576	Orthorhombic: Pnam (62) a: 0.74188; b: 0.49382; c: 0.25496
Crystallite Size D, nm	44.1	55.74	16.95

* Full width at half peak height.

** The calculation of the interplanar distances d was determined by the Wolf-Bragg equation: $2 \sin \theta = (\lambda / d)$; The average crystallite size, i.e. the areas of coherent scattering (OCD) was calculated using the Scherrer formula: $D = (\xi \lambda / \beta \cos \theta)$, where θ is the reflection angles in degrees; D is the average crystallite size, nm; ξ is a factor taking into account the shape of the particles and the indices of the reflecting plane, since the range of changes from 0.98 to 1.39 in practice is $\xi = 1$; β is the integral width; λ is the Cu - K α radiation wavelength ($\lambda = 0.15418$ nm).

Thus, based on the analysis of the obtained X-ray diffraction patterns, we can conclude that: a) the raw powder under investigation consists of a mechanical mixture of indium and germanium phosphide, b) the resulting composite consists of a well-crystallized polyethylene matrix containing the phases of indium

and germanium phosphide, spatially separated from each other in a polymeric matrix.

FT-IR data. Below are the FT-IR spectra of pure HDPE and HDPE, containing various concentrations of InP/Ge particles with a thickness of 100 and 200 microns.

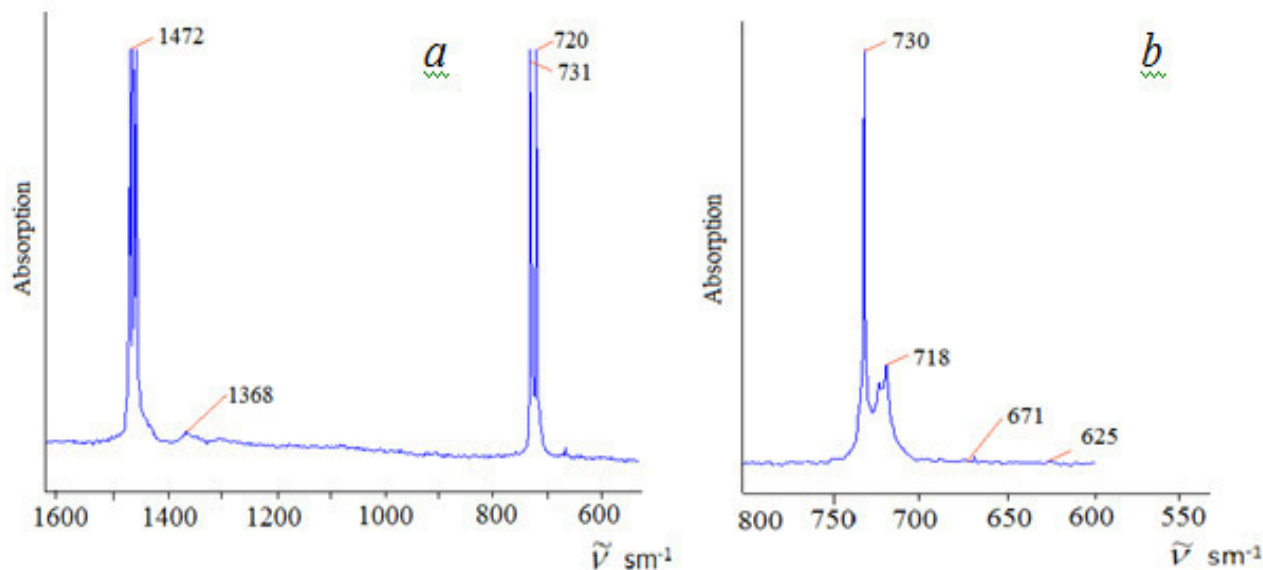


Fig. 3. FT-IR spectra of the: a) HDPE with 6 vol. % InP/Ge (100 μm) b) HDPE with 6 vol. % InP/Ge (200 μm).

From fig. 3 it can be seen that all the characteristic bands necessary for identifying the structure of the polymer, namely, doublets $720\text{--}730\text{ cm}^{-1}$ and $1462\text{--}1473\text{ cm}^{-1}$ for PE, are clearly visible on these spectra. The first (doublet $720\text{--}730\text{ cm}^{-1}$) are due to the pendulum oscillations of methylene groups in the crystalline parts of polyethylene with molecules in a flat trans-conformation and are sensitive to the intermolecular interaction and conformational state of macromolecules [14]. Changes in the characteristic frequencies of polyethylene, depending on the concentration of the filler, can be clearly traced by the spectra of FT-IR HDPE films with containing 6 % (100 μm and 200 μm) by volume of fillers, respectively in the regions: a) $1460\text{--}1480$ and b) $700\text{--}750\text{ cm}^{-1}$. The doublet observed in the IR spectrum is due to the splitting of the 1460 cm^{-1} band. The 1472 cm^{-1} band characterizes the crystalline region in HDPE samples, and the 1462 cm^{-1} band is characteristic of the amorphous component of HDPE. As can be seen, the introduction of InP/Ge microparticles into the polymer leads to a redistribution of the intensities of doublet bands.

5. DIELECTRIC PROPERTIES

The results of the study of the temperature-frequency dependence of the dielectric constant and dielectric loss of the compositions of HDPE + x vol. % InP/Ge ($0 \leq x \leq 9$) are shown in figures 4 and 5.

As follows from fig. 4a for all the above composites in the temperature range studied, the dielectric constant decreases linearly with increasing temperature. With an increase in the volume content of the InP filler, an increase in the dielectric constant occurs, in particular, for pure high-density polyethylene ϵ at room temperature is 2.07 (curve 3), for a composite with the addition of 3 vol. % InP 1.86 (curve 1), for the composite, 5 vol. % InP 1.95 (curve 2), for the composite, 7 vol. % InP 2.4 (curve 4), and 9 vol. % InP, 3.48 (curve 5).

In fig. 5 shows the frequency dependences of the dielectric constant and dielectric loss of HDPE composites with different InP/Ge filler contents in the frequency range 25–106 Hz. As follows from fig. 5a in the studied frequency range for all composites and pure HDPE ϵ practically does not change with increasing frequency.

Thus, the above experimental results allow us to state the following.

1. When modifying the polymer matrix with nanostructured InP/Ge micro-size particles, there are noticeable changes in the structural and dielectric properties for samples containing up to 4% by volume of filler, most pronounced in the FTIR spectra.

2. The mechanism of interaction of the matrix with the solid phase of the modifier is not obvious, since polyethylene, which in this case serves as a matrix and is a product of ethylene polymerization, does not contain groups that are active in the reaction with the filler.

3. The dependence of the intensity of the bands in the FTIR spectra on the content of the filler introduced into the polymer can be used to study the nature of the mechanism of influence of fillers on the structure of HDPE.

4. To control the technology of obtaining composite HDPE samples with nanostructured InP/Ge particles, X-ray fluorescence microscopy and IR spectroscopy are most suitable. The above studies have

shown that the distribution of indium and germanium phosphide particles, as well as the intensity ratio of the characteristic HDPE bands in the IR spectra, depend on the concentration of fillers. These methods allow you to control the concentration of filler particles in the manufacture of a composite material of the desired composition by measuring X-ray fluorescence and IR spectra.

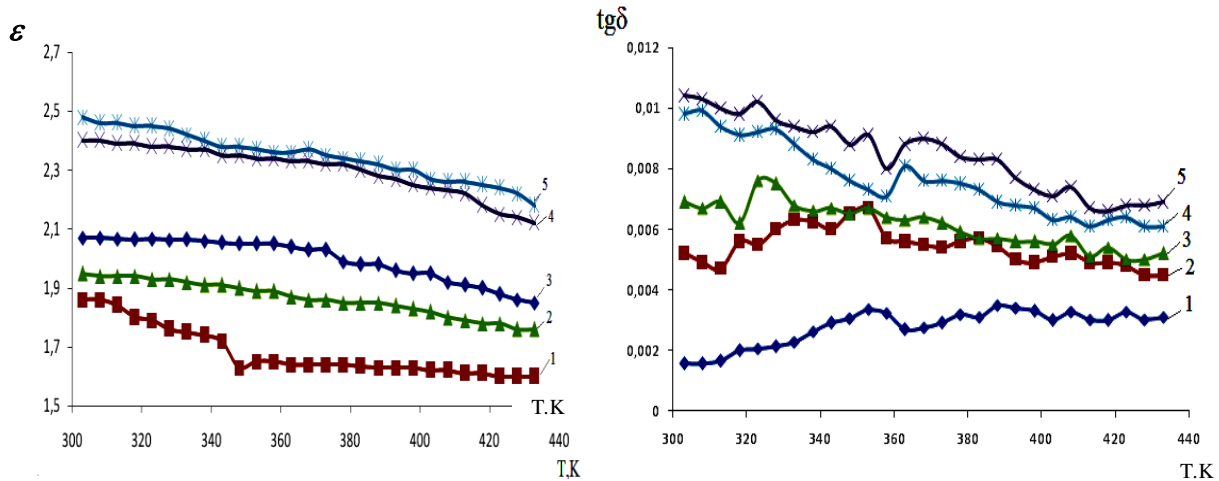


Fig. 4. Temperature dependences of the dielectric constant (a) of HDPE compositions with different filler contents of InP/Ge (in vol. %): 1-3; 2-5; thirty; 4-7; 5-9 and dielectric losses (b) of HDPE compositions with different filler contents of InP/Ge (in vol. %): 1-0; 2-3; 3-5; 4-9; 5-7 of the measurement temperature.

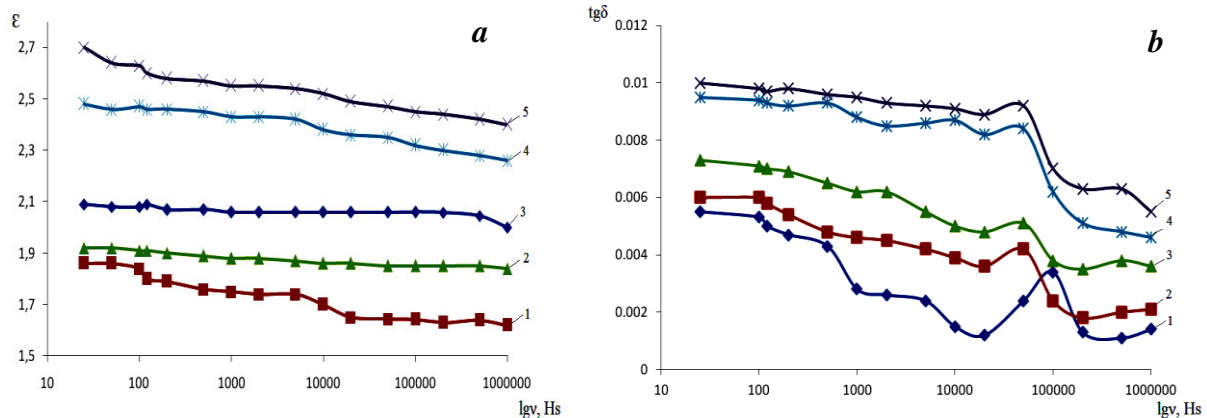


Fig. 5. Frequency dependences of the dielectric constant (a) of HDPE compositions with different content of InP/Ge filler (in vol. %): 1-3; 2-5; 3-0; 4-9; 5-7 and dielectric losses (b) of HDPE compositions with different filler contents of InP/Ge (in vol. %): 1-0; 2-3; 3-5; 4-9; 5-7 of the measurement temperature.

6. CONCLUSION

Structural features and dielectric properties of HDPE films of various thickness (100, 200 μm) modified by germanium and indium phosphide in a 1:1 ratio by weight and total content of 2-10% by volume were studied using a combination of X-ray fluorescence, X-ray diffraction and infrared spectroscopy. Changes in the structure and dielectric properties of the composite depending on the filler content are established. It is shown that the methods of X-ray fluorescence microscopy and IR spectroscopy are most suitable for optimizing the concentration of

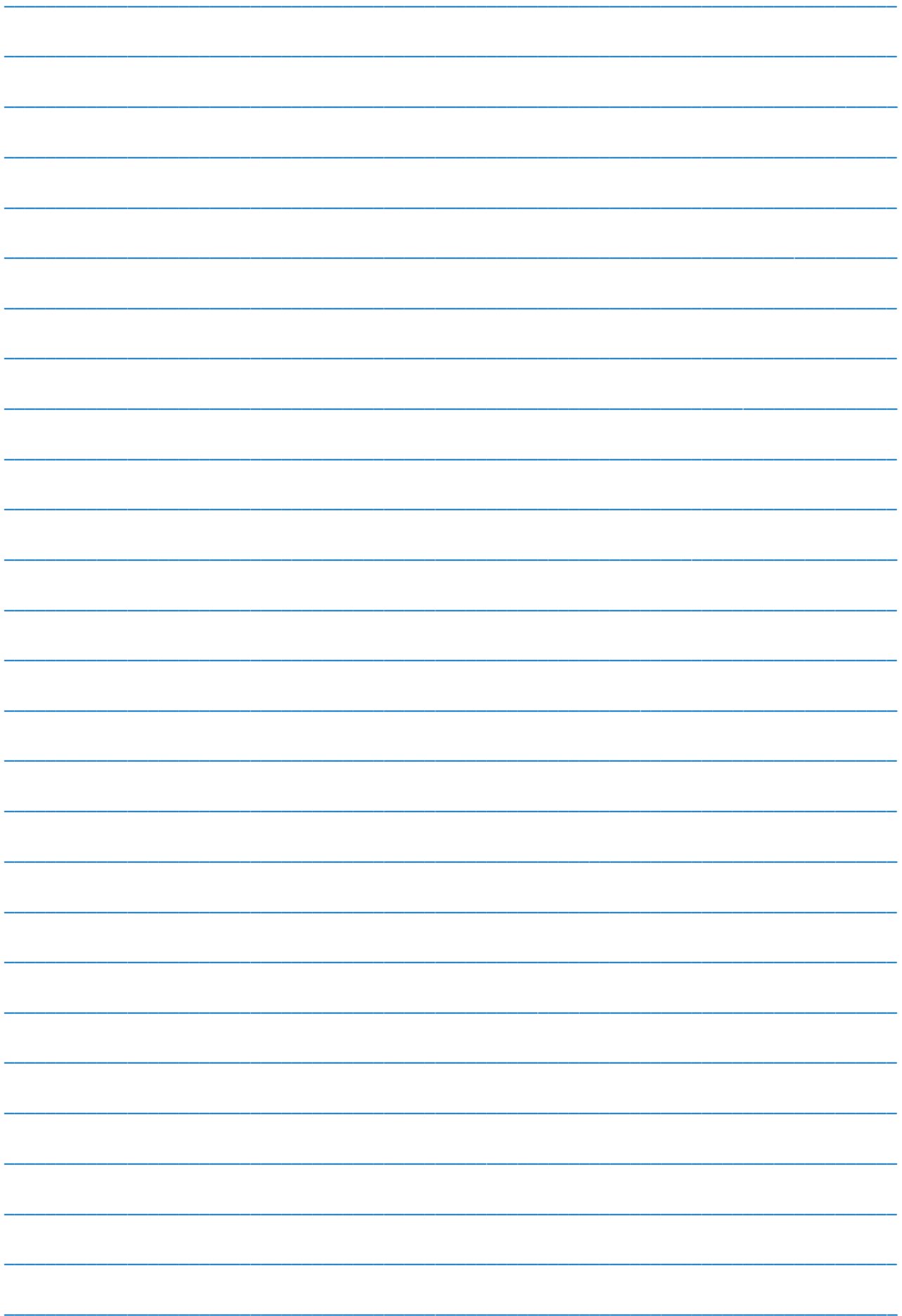
the filler and controlling the distribution of its particles in the polymer.

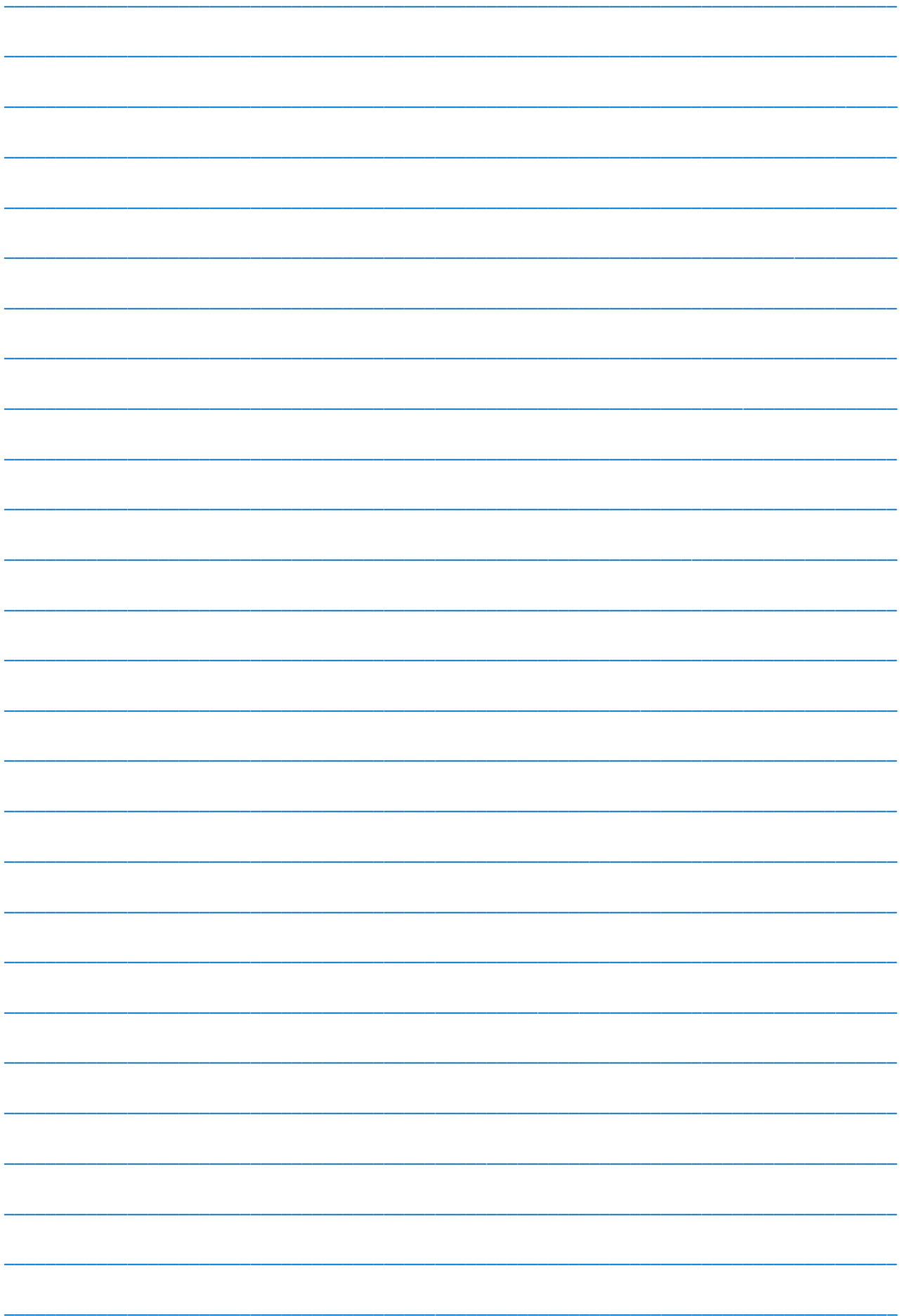
7. ACKNOWLEDGMENT

The authors express deep gratitude to the head of the laboratory of crystallography of the Institute of Physics of ANAS, Doctor of Physical and Mathematical Sciences, prof. I.R. Amiraslanov and the staff of this laboratory are Doctor of Philosophy in Physics E.R. Aliyeva for taking X-ray diffractograms and Doctor of Philosophy in Physics of the Institute of Radiation Problems of ANAS N.N. Gadzhieva for taking infrared spectra and discussing the results.

- [1] R. Wang, Y.T. Zhang, J.Q. Yao. IEEE Photonics journal, 7, 2015: 2600308
- [2] M. Patabi, A.B. Saraswathi. *Composite Interfaces*, 17, 2010: 103-111.
- [3] N.P. Gaponik, D.V. Talapin, A.L. Rogach, A. Eychmüller. *Journal of Materials Chemistry*, 10, 2000: 2163-2166.
- [4] F. Habelhams, B. Nessark, D.Bounhafs, A.Cheriet, H.Derbal. Synthesis and characterisation of polypyrrole - indium phosphide composite film. *Ionics*, 2010: 177-184.
- [5] B. Scruggs, M. Haschke, L. Herczeg, J. Nicolosi. *Advances in X-ray Analysis*, 42, 2000: 19-25.
- [6] K.Sugihara, M.Satoh, Y.Hayakawa, A.Saito, T.Sasaki *Advances in X- ray Analysis*, 42, 2000:161-170.
- [7] Sh.Sh. Rashidova, M.A. Gusinova, S.M. Rzaeva. *Journal of Engineering Physics and Thermophysics*, Vol 88, 2015:781-784.
- [8] Chung, T.C.M. «Functional polyolefins for energy applications», *Macromolecules*, 2013, vol. 46, p. 6671 - 6698.
- [9] Scheidl, K. *Global PE Report*, Proc. of PE, 99 Polyethylene World Congr., Zurich, September, 1999. P. I-2.
- [10] Polyethylene of high pressure. Scientific - technical basis of industrial synthesis. A.V. Polyakov, F.I. Duntov, A.E. Sofiyev et al. L.: Chemistry, 1988, p.200 (in Russian)
- [11] T.Hirtsu and P.Nugroho. Polymeric structure. *Journal of Applied Polymer Science*, 1997, 66, 6, 1049.
- [12] A.R Blythe., D. Bloor. *Electrical properties of polymers*. M.: fizmatlit, 2008. 376 p. (in Russian).
- [13] R. Kotek Recent advances in polymer fiber. *Polymer Reviews* Vol. 48, issue 2, April-June, 2008, p. 221-229
- [14] R. Zbinden. *IR of spectroscopy of high polymers*. M.: Mir, 1966, p.356 (in Russian).
- [15] M.I. Aliev, E.M. Gojaev, S.M. Rzaeva and Sh.Sh. Rashidova. *Physical Science International Journal* 8 (3): XX -XX, 2015, Article no. PSIJ. 18839. p.1-5.

Received: 05.03.2019.





CONTENTS

1.	Optical parameter spectra of Bi_2Te_3 (Ni, Cu, Zn) single crystals N.Z. Jalilov	3
2.	Ion-optical calculation of time-of-flight mass-spectrometer T.K. Nurubeyli, K.Z. Nuriyev	9
3.	The use of nuclear-physical methods for the analysis of wastes from mining and processing industry I.Z. Kamanina, S.P. Kaplina, M.V. Gustova, M.V. Frontasyeva, N.E. Pukhaeva	13
4.	The process of ostwald maturation on TlGaTe_2 crystal surface K.G. Khalilova, N.M. Abdullayev, K.Sh. Kagramanov	18
5.	Analysis of fluctuation conductivity in $\text{Y}_{0.7}\text{Cd}_{0.3}\text{Ba}_2\text{Cu}_3\text{O}_{7-\delta}$ V.M. Aliev, J.A. Ragimov, R.I. Selim-zade, B.A. Tairov	21
6.	Structure study of Se-As chalcogenide glassy semiconductor system doped by EuF_3 impurity S. N. Garibova, A.I. Isayev, S.I. Mekhtiyeva, S.U. Atayeva, S.S. Babayev, Y.R. Aliyeva, N.T. Hasanov	25
7.	Influence of fullerenes on dielectric and conductivity properties of smectic a liquid crystal with negative dielectric anisotropy T.D. Ibragimov, A.R. Imamaliyev, G.F. Ganizade	31
8.	Magnetic moment of electrons in diluted magnetic semiconductor quantum ring A.M. Babanli, B.G. Ibragimov	35
9.	Structural peculiarities and dielectric properties of high-density polyethylene films containing InP and Ge particles S.M. Rzayeva, Sh.Sh. Rashidova, T.H. Ismailov	39



www.physics.gov.az